# IMDEA Materials Institute

## Competing deformation mechanisms in ARB Cu/Nb metallic multilayers as a function of layer thickness and temperature

**Master of Science Thesis**

**Jeromy Snel**

**March 2016**

institute IMdea materials

# Competing deformation mechanisms in ARB Cu/Nb metallic multilayers as a function of layer thickness and temperature

Master of Science Thesis

For obtaining the degree of Master of Science in Aerospace Engineering at Delft University of Technology

Jeromy Snel

March 2016

Delft University of Technology - Faculty of Aerospace Engineering

Department of Aerospace Structures and Materials

Novel Aerospace Materials Group

**Graduation Committee**

Dated: 13 of April 2016

Chairman of the committee:

Prof.dr.ir. S. van der Zwaag

Committee members:

Dr. J. Molina-Aldareguia

Dr.ir. W.G. Sloof

# Abstract

This thesis investigated the mechanical properties and deformation behaviour of accumulative roll-bonded (ARB) Cu/Nb metallic multilayers at nanoscale layer thicknesses and temperatures up to $400\,^{o}C$.

Samples with individual layer thicknesses between 7 and 63 nm were nanomechanically tested at room-temperature by micropillar compression and nanoindentation at quasi-static strain-rates. Yield strength, strain-rate sensitivities and activation volumes were obtained from the experiments. First a small scale study was performed to reveal the effects of microstructural variations and pillar taper on the obtained material parameters. The deformed micropillars were then studied under the SEM to link the experimental results to observated deformation behaviour at different thicknesses. Additionally the results obtained from nanoindentation and micropillar compression were compared. Finally, based on the experimental results and observations a deformation mechanism map was proposed for the material as a function of layer thickness.

Next, the high-temperature properties of the material were investigated. Micropillar compression experiments were performed in-situ inside an SEM at temperatures of $20\,^{o}C$, $200\,^{o}C$ and $400\,^{o}C$. The influence of temperature on the mechanical properties and deformation behaviour at different layer thicknesses was studied by means of the obtained material parameters and SEM observations in pillar deformation. TEM cross-sections were fabricated and analyzed to further investigate and/or confirm some of the deformation-related suspicions. The results and observations were used to draw qualitative conclusions on the high-temperature performance of the material.

# Table of contents

# List of Figures

# List of Tables

# Chapter 1

# Introduction

The introductory chapter is divided into two parts. The aim of the first part is to provide the reader with the state-of-the-art knowledge on the mechanical behaviour and underlying deformation mechanisms of metallic multilayered systems. Section 1.1 gives a brief introduction into nanoscale multilayers in general. In Section 1.2 the emphasis is on the structure and properties of Cu/Nb multilayers. Multilayer strength and deformation behaviour are discussed, and a small section is devoted to the (limited) knowledge on the high-temperature behaviour of the material. The second part of the introduction briefly introduces the basic concepts and challenges of nanomechanical testing. Emphasis will be on nanoindentation and micropillar compression with the final section devoted to high-temperature experiments.

## 1.1 Nanoscale multilayers

Over the last decades multilayered materials consisting out of metal-metal, metal-ceramic, ceramic-ceramic and metal-intermetallic alternating layers have been getting worldwide attention due to their outstanding performance. Metal-ceramic multilayers for example show an attractive combination of electrical, magnetic, optical and mechanical properties, with applications in electronic devices and as optically absorbing coatings in solar collectors [24]. Within the ceramics and hard-coatings industry, multilayering has been applied several decades now for strengthening and toughening of coatings [25]. Metal-metal multilayers such as Cu/Nb show an outstanding radiation resistance, greatly maintaining its strength during irradiation by the creation of He bubbles.

Multilayering is therefore a powerful tool for introducing and/or optimizing mechanical and functional properties. Within this work emphasis is on the mechanical and deformation behaviour of multilayers. Studies on metal-metal multilayers with layer thicknesses in the nanoscale range have shown ultimate strengths of several GPa's [26–33]. The oustanding mechanical performance is due to a combination of the properties of the individual constituents and the presence of dislocation blocking interfaces. It is generally known that as the individual layer thickness decreases to nanoscale sizes, the volume fraction of interfaces is so high that these start to dominate the dislocation-related processes. Similar to grain boundaries in conventional metals, these interfaces can act as dislocation sources, sinks, storage sites and promote or demote dislocation transmission to adjacent layers [34]. Interface structure plays a key role here, and distinction is made between the following three interface types:

- **Coherent interfaces:** A coherent interface is formed when two materials with the same crystal structure and small lattice mismatch meet. Elastic straining of the lattices occurs along the interface plane resulting in alternating tensile and compressive stresses, increasing the resistance against dislocation movement. A second (less-dominant) strengthening mechanisms can occur due to large shear modulus mismatch between the layers[1].

[1] A large shear modulus mismatch between layers may result in high repulsive stresses (Koehler stresses) when dislocations transmit from the lower modulus phase into the higher modulus phase.

- **Semi-coherent interfaces:** As opposed to coherent interfaces, semi-coherent interfaces have a larger lattice mismatch. Large straining of the lattices is energetically not favoured, instead misfit dislocations are formed at the interface. Strengthening is dominated by the misfit dislocations acting as barriers against glide dislocations. Koehler stresses[1] can also play a role, but to a lesser extent.

- **Incoherent interfaces:** Incoherent interfaces are formed between materials with different crystal structures and large lattice mismatch. A periodic array of misfit dislocations is formed along the interface. Interfaces act as dislocation sinks trapping the dislocations and require large stresses for dislocation transmission.

The effectiveness of the different dislocation-blocking mechanisms is not the same. In coherent and semi-coherent interfaces, slip systems and directions are nearly continuous across the interface and provide efficient pathways for tranmsission [35]. In multilayered systems with incoherent interfaces slip sytems and directions are discontinuous across the interface. These interfaces provide stronger transmission barriers and also higher strengthening capability. Important to note is that only chemically sharp interfaces, i.e. interfaces with an abrupt transition between the constituents provide effective barriers to dislocation transmission. Chemical intermixing drastically reduces the interface effectiveness and the strength of the multilayered material as observed in Cu/W multilayers [26, 36]. With interfaces being the dominant physical property in mechanical and deformation behaviour of nanoscale multilayers, in-depth knowledge on the structure-property-functionality relation is key in understanding the behaviour of existing multilayers and developing new multilayered materials with tailored properties.

## 1.2 Cu/Nb metallic multilayers

Amongst the metal-metal multilayers Cu/Nb has been the most widely studied. Its high radiation tolerance in combination with its mechanical properties and thermal stability makes them a material-of-interest to the nuclear industry, with potential applications as radiative coatings in nuclear powerplants. Part of the outstanding irradiation tolerance is attributed to the interfaces which increase the capacity to absorb radiation and act as sinks for radiation-induced defects. At elevated temperatures these interface also limit the growth of $He^{+}$-bubbles to a size on the order of the layer thickness [37]. The interfaces therefore prove valuable for both mechanical and irradiation properties of the multilayered system.

### 1.2.1 Interface texture

Cu/Nb nanoscale metallic multilayers (NMMs) consist of alternating layers of Cu (FCC) and Nb (BCC). The interfaces formed are incoherent and characterized by a high dislocation barrier strength. More interestingly the interface texture, i.e. the cube-on-cube crystal orientations at the interface, has shown to be dependent on the manufacturing technique. The most used manufacturing techniques for multilayered systems are physical vapor deposition (PVD) processes and accumulative roll bonding (ARB).

In physical vapor deposition (PVD) processes[2] thermally preferred interfaces are formed predominantly adopting the Kurdjumov-Sachs (KS) and Nishiyama-Wasserman (NW) misorientation relationship [1,38]. Figure 1.1a and b shows HRTEM micrographs of respectively the KS and NW interfaces. Both interfaces adopt the $\{111\}Cu||\{110\}Nb$ texture, the NW interface deviates by a $5^{o}$ twist about the interface normal [1]. The compact planes of Cu (111) and Nb (110) are aligned parallel to the interface plane and a flat interface structure is formed. The misfit dislocations formed along the interface plane contain an in-plane[3] Burgers vector.

[2] Bottom-up manufacturing technique in which the multilayer is built-up layer by layer, e.g. d.c. magnetron sputtering

[3] In-plane refers to the interface plane. Since in PVD produced interfaces the compact planes are parallel to the interface plane, Burgers vector is contained both within the interface plane and the compact plane.

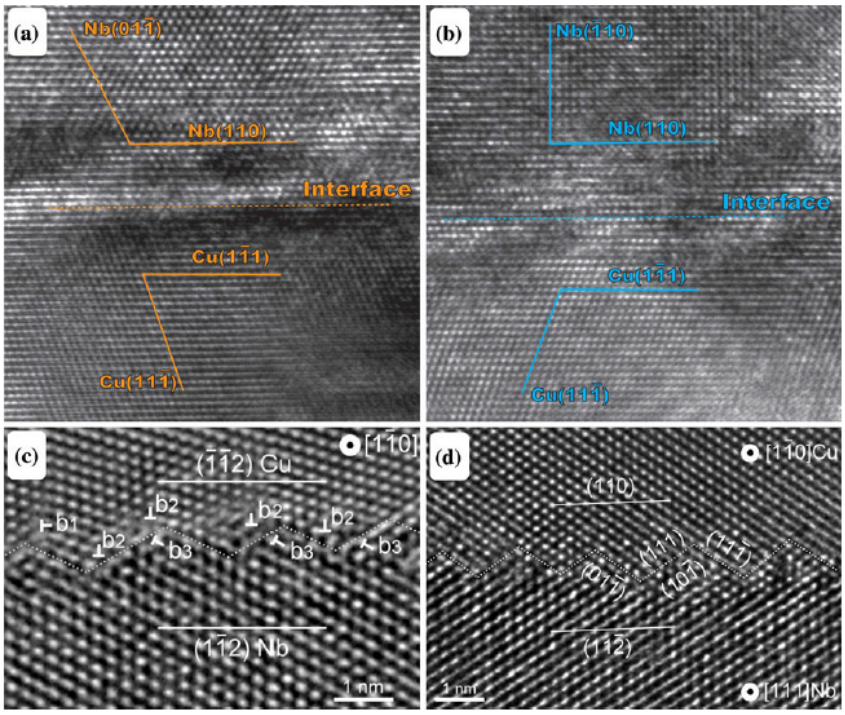


Figure 1.1: HRTEM micrographs of PVD and ARB produced interfaces: a) $\{111\}Cu||\{110\}Nb$ KS interface in Cu-Nb PVD nanolayered composite. b) $\{111\}Cu||\{110\}Nb$ NW interface in Cu-Nb PVD nanolayered composite. c) $\{112\}Cu||\{112\}Nb$ KS interface in Cu-Nb ARB nanolayered composite. d) $\{110\}Cu||\{112\}Nb$ interface in Cu-Nb ARB nanolayered composite. [1]

In accumulative roll bonding on the other hand thick sheets of Cu and Nb are stacked, rolled, cut and re-stacked, reducing the layer thickness in each rolling step until the desired layer reduction is obtained. During the process the multilayer is being severely deformed and mechanically driven interfaces are formed. The interfaces predominantly adopt the $\{112\}Cu||\{112\}Nb$ KS and $\{110\}Cu||\{112\}Nb$ misorientation relationship [1,38–40], as depicted in Figures 1.1c and d. What is remarkable of these preferred interface structures is that they only start to form as the individual layer thickness is reduced below the micron-scale [41]. Furthermore as opposed to PVD produced interfaces, ARB produced interfaces are faceted and contain misfit dislocations with both in-plane and out-of-plane Burgers vectors [42].

The ability of the interface to block dislocation transmission is the most dominant interface property contributing to multilayer strength. Due to the textural differences of PVD and ARB produced interfaces, their dislocation blocking capability differ and hence their mechanical properties. Two important interfacial characteristics for transmission are:

- **Alignment of slip systems:** Efficiently aligned slip systems (continous slip systems) of the individual constituents across the interface provide easy pathways for dislocation transmission. Discontinuous slip systems are difficult pathways.
- **Interfacial shear strength:** Dislocations approaching interfaces with low shear strength tend to shear the interface and get absorbed. Interfaces with high shear strength are less likely to shear and thereby promote dislocation transmission.

The higher degree of discontinuous slip systems across PVD produced interfaces and the low interfacial shear strength makes these interfaces stronger barriers to dislocation transmission. PVD Cu/Nb is therefore generally stronger than ARB Cu/Nb since the stresses needed to promote a dislocation into

the adjacent layer are higher. Besides dislocation transmission the interfaces also act as sources for dislocation nucleation/emission and dislocation sinks. Both interfaces are capable of nucleating dislocations, however the mechanisms of nucleation are different. In PVD produced interfaces which contain misfit dislocations with in-plane Burgers, stress concentrations cause the nucleation and emittance of Shockley dislocations. In ARB Cu/Nb dislocations are nucleated by dissociation of interfacial misfit dislocation. ARB Cu/Nb is generally considered to supply lattice dislocations more easily due to the presence of misfit dislocations with out-of-plane Burgers vector.

### 1.2.2 Multilayer strength

The interface-dislocation interactions are important contributors to the deformation mechanisms and strength of multilayered systems. Multilayers generally show a trend of increasing strength with decreasing layer thickness, related to the increasing volume fraction of interfaces at finer thicknesses. Especially the work by Misra and colleagues at Los Alamos National Laboratory on multilayer strengthening and deformation mechanisms have been ground breaking in understanding multilayer behaviour as a function of layer thickness. In general three deformation regimes can be distinguished for multilayer strength with individual layer thickness of microns and smaller. Figure 1.2 gives a schematic overview of the different deformation regimes governing multilayer strength, as proposed by Misra et al. [2]

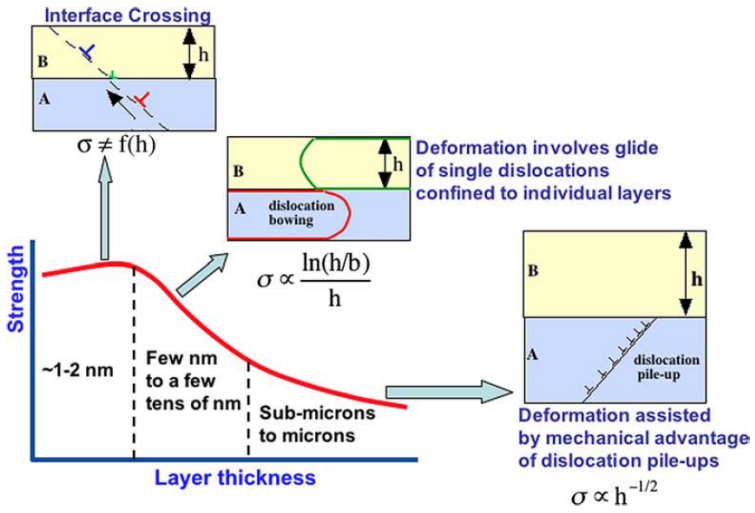


Figure 1.2: Schematic overview of the different dislocation regimes and their mechanisms observed in multilayers at different length scales. [2]

At layer thicknesses of microns to several tens of nanometers the characteristic length scale is large enough for dislocation pile-ups to occur. The interfaces operate in a similar fashion as grain boundaries in conventional metals, and restrict movement of the dislocations. Multilayer strength for this layer thickness regime has shown strengthening similar to the Hall-Petch behaviour in conventional metals [2, 43]. The Hall-Petch behaviour for multilayer strength is defined as [2]:

$$\sigma_y = \sigma_0 + kh^{-1/2} \tag{1.1}$$

where $\sigma_y$ is the yield strength, $\sigma_0$ is a measure of the lattice friction stress to slip, $k$ is the Hall-Petch slope and $h$ is the layer thickness. Studies have shown that Hall-Petch behaviour is valid down to layer thicknesses of 50-75 nm for PVD Cu/Nb [2, 43]. For ARB Cu/Nb it is unknown.

As the layer thickness further reduces below several tens of nanometers, dislocation pile-ups become difficult and deformation occurs by glide of single dislocations. A schematic illustration of this mechanisms is given in Figure 1.3. Due to the relatively small distance between the interfaces at these fine layer thicknesses, dislocations are being bowed out in between the interfaces. Interfaces that are strong barriers to dislocation transmission result in higher repelling forces and more bowing. In addition to glide, during a dislocation loop dislocations are being deposited at the interface. These can interact with subsequent dislocation loops and cause some strain-hardening. Based on this characteristic behaviour Misra et al. developed a model for confined layer slip [2]:

$$\sigma_{cls} = M\frac{\mu b}{8\pi h'}\left(\frac{4-\nu}{1-\nu}\right)\left[ln\frac{\alpha h'}{b}\right] - \frac{f}{h} + \frac{C}{\lambda} \tag{1.2}$$

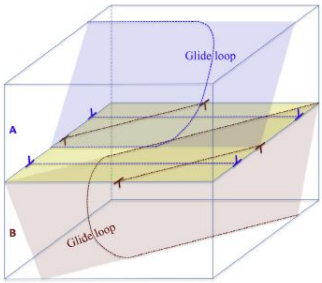


Figure 1.3: Schematic of the confined layer slip mechanism in multilayered materials. The interfaces bow-out the dislocations resulting in dislocation glide loops confined within layers. During the process dislocations are deposited at the interfaces that can interact with subsequent glide loops. [3]

A more detailed description of the parameters and their values is given in Chapter 4. However, the three terms on the right hand side are based on respectively the glide stresses, interface stresses and the stresses due to interaction with the deposited interface dislocation array. At layer thicknesses of a few nanometers the stresses needed to bow-out dislocations become so large that dislocation transmission is favourable. A peak strength is observed and the layer thickness at which this occurs is referred to as the critical layer thickness $h_c$. Below the critical layer thickness a strength plateau or even a drop in strength is observed ($\sigma \neq h$). For PVD Cu/Nb the peak strength is observed at a few nanometers [2,27]. For ARB Cu/Nb it is believed to occur at $\pm$10 nm [26].

### 1.2.3 Deformation behaviour

When deforming Cu/Nb multilayers some material behaviour is consistently observed. Numerous studies have shown the occurrence of shear bands in Cu/Nb multilayers [4, 9, 44–46]. It is a crystallographic rotation of the layers to an orientation where slip is more likely to occur. This re-orientation can activate slip systems and/or cause the material to shear along the interfaces. Shear banding and shear failure are considered plastic instabilities, and are closely related to the strain-hardening capability of the material. Similar to strain-hardening observed in nanocrystalline metals, multilayered systems show almost zero strain-hardening at the very fine thicknesses [13] and are prone to strain localization. TEM and HRTEM analysis by Zheng et al. on PVD and ARB Cu/Nb revealed trat the transmissibility of interfaces plays a profound role in strain localization [4]. They postulated that interfaces that block transmission can tilt the interface and the crystallographic orientations of the layers such that layer-parallel deformation is possible.

In addition to shear banding multilayers containing FCC layers are also prone to form deformation twins as observed in multiple FCC-based multilayers [4, 33, 47]. Beyerlein et al. showed a transition from deformation by slip only at layer thicknesses of 100 nm to deformation by slip and twinning at layer

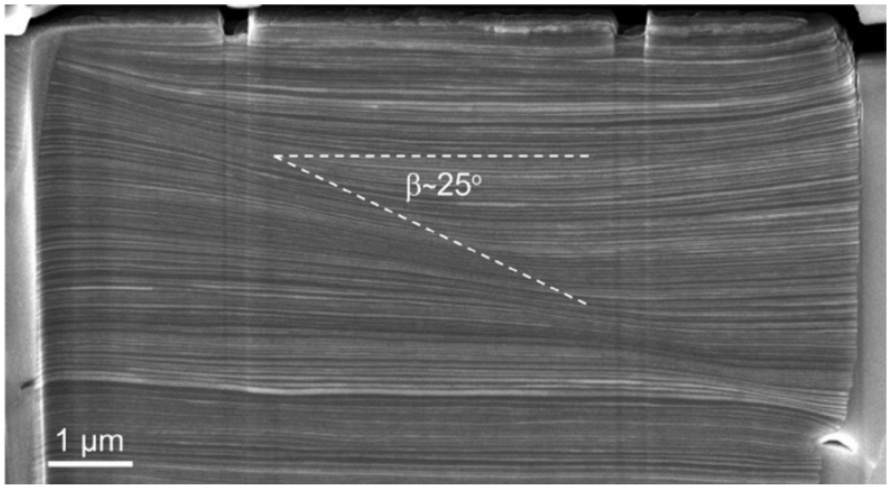


Figure 1.4: SEM image of a shear band in a deformed micropillar [4].

thicknesses of 60 nm [9]. At a layer thickness of 10 nm the twin fraction had reached 30%. A study by Zheng et al. on the twinning mechanisms in ARB Cu/Nb revealed an important role of the interfaces and interfacial misfit dislocations in the formation of deformation twins [47]. The twin-formation plane suggested twin nucleation to occur due to dissociation of interfacial misfit dislocations, and twin growth to occur via alternating emissions from opposite interfaces. In ARB Cu/Nb twinning occurs sooner than in PVD Cu/Nb [1, 9, 48], which based on the suggestions by Zheng et al. on twin nucleation is not surprising regarding the presence of misfit dislocations with out-of-plane Burgers vector in ARB produced interfaces.

### 1.2.4 Elevated temperature behaviour

The focus so far has been on the room-temperature behaviour of the material. However, since the material is to be applied as a coating in a nuclear enviroment, its performance over the full spectrum of conditions needs to be studied which includes the performance at elevated temperatures. Studies at elevated temperatures are however limited, with most studies addressing thermal stability and/or tensile performance [49–54]. Few studies are available on the compressive behaviour of the material at elevated temperatures.

Studies on the thermal stability of PVD Cu/Nb multilayers showed good morphological stability up to temperatures of $500^oC$ [52–54]. At higher temperatures grain growth and alignment of grain boundaries within different layers was observed as depicted in Figure 1.5. These so-called quadruple points were found to be unstable and formed ”triple points” by diffusion-assisted offsetting of layers. In-turn the triple points were found to anchor the microstructure, preventing further grain growth or layer splitting.

At layer thicknesses of 35 nm and smaller the microstructure was found te be more unstable. The layered structure was not maintained and frequent pinch-off was observed followed by spheroidization of the pinched-off segments. In ARB Cu/Nb no pinch-off and spheroidization was observed for a layer thickness of 18 nm exposed for 1 hour to $700\,^oC$. However, as opposed to PVD Cu/Nb, significant layer coarsening was observed with layer thickness increasing from 18 nm to 75 nm.

Mara et al. studied the high temperature tensile properties of PVD Cu/Nb with layer thicknesses of 40, 60 and 75 nm at $500\,^oC$, $600\,^oC$ and $700\,^oC$ [49–51]. They showed a significant decrease in strength at elevated temperatures and strain-rate sensitivities approaching 0.5 at $700\,^oC$, indicative of grain boundary sliding. However it is likely that the tensile experiments were performed in the layer direction, thereby

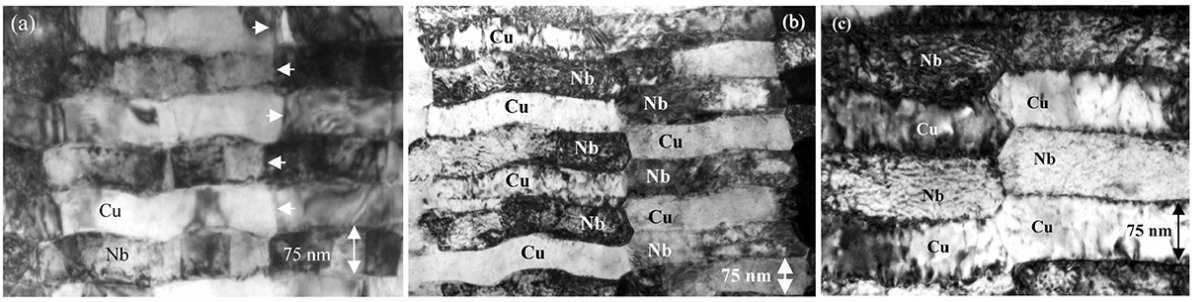


Figure 1.5: SEM images showing the microstructural evolution of PVD Cu/Nb at temperatures of (a) $600\,^oC$, (b) $700\,^oC$ and (c) $800\,^oC$. Alignment of grain boundaries along a vertical line occurs (a), followed by layer offsets (b) and the formation of triple points (c).

promoting grain boundary and/or interface sliding. This mechanism is expected to be difficult when tested perpendicular to the layers, and different mechanisms of deformation are expected.

Monclús et al. studied the high temperature flow behaviour of ARB Cu/Nb by nanoindentation up to $400\,^oC$. They reported a transition of peak strength from layer thickness of 10 nm at room-temperature to 18 nm for temperaturess of $300 - 400\,^oC$. However no strain-rate sensitivities were reported and deformation behaviour at elevated temperatures was not extensively studied. High-temperature micropillar compression studies on other Cu-based metal-metal and metal-ceramic multilayered systems showed diffusive flow of Cu at temperatures of $200\,^oC$ and higher [25, 31]. This was more pronounced in Cu/TiN containing hard ceramic layers, with Cu microcrystals forming on the pillar walls.

## 1.3 Nanoscale testing

This section gives a short introduction into nanomechanical testing. First an overview is given of the different testing techniques and their inherent differences. A small portion is devoted to the strength-related size-effects. Finally the challenges of performing nanomechanical tests at elevated temperatures are addressed.

### 1.3.1 Techniques

Nanoindentation and to a lesser extent micropillar compression are the most widely used techniques for small-scale testing of materials. In nanoindentation a tip with well-defined geometry is used to indent the sample surface while recording the force and indenter displacement. Different indenter geometries can be used as depicted in Figure 1.6. The power of nanoindentation lies in the ease of performing these experiments. Unlike micropillar compression and tensile testing, no pre-fabrication of individual test samples is needed and the only requirement is a good sample surface quality. This technique relies on accurate knowledge of the indenter geometry to determine the contact area with the material while indenting [11]. A more detailed overview of the governing equations for nanoindentation experiments is given in Section 2.4.3.

Although nanoindentation is relatively easy to perform, interpretation of the results is often complex. The plastic volume in nanoindentation is represented by a sphere around the indenter, and as a result of the geometry of the indenter a complex stress-strain state develops. Furthermore due to the geometry-based estimation of contact area this technique is also sensitive to pile-up or sink-in of material around the indenter, which directly affects the contact area and thus the accuracy of the measurements.

Micropillar compression is a relatively new technique introduced at the beginning of the century by

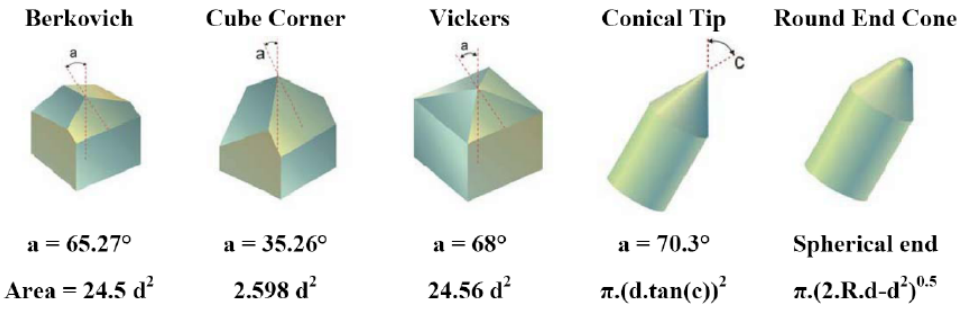


Figure 1.6: Various common indenter shapes and their projected cross-sectional area as a function of indentation depth [5, 6]

Uchic et al. in order to study plasticity on samples with sub-micron length scales [7, 55]. It requires pre-fabrication of pillars with micro- or nanoscale dimensions by focused ion beam (FIB) milling. Compression of the micropillar is performed with a flat-punch indenter containing a flat head, as depicted in Figure 1.7.

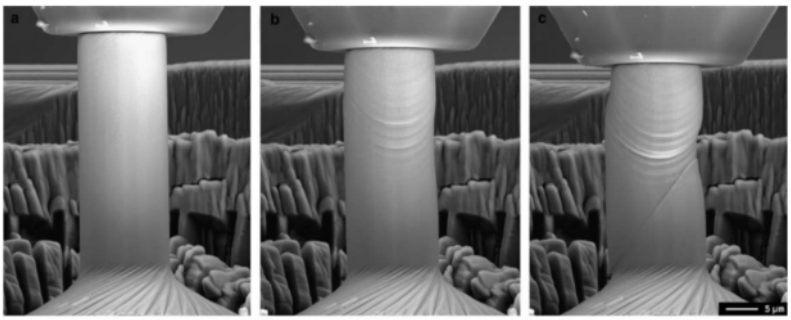


Figure 1.7: SEM images showing the compression of a micropillar at different strains [7].

Performing micropillar compression experiments on a material requires significantly more preparation than nanoindentation. The big advantage however is the presence of a more homogeneous stress-strain state in the pillar. Interpretation of the results are more straightforward and an additional advantage is that deformation behaviour is more easily observed in the pillars. Still care has to be taken when performing compression experiments. The obtained compression curves are known to be sensitive to pillar-indenter alignments, pillar taper and need to be corrected for substrate deflection. Furthermore materials can also exhibit a so-called ”pillar-size effect”, with smaller pillars appearing stronger [56–59]. Zhang et al. observed a dependency of the pillar-size effect on layer thickness in Cu/Zr pillars, with the strengthening effect being increasingly pronounced at finer thicknesses [29]. In some cases size-effects were also observed to develop with temperature [59]. However for Cu/Nb pillars room-temperature studies have shown that the pillar-size effect is negligible [27, 44].

### 1.3.2 High-temperature testing

Compared to room-temperature nanomechanical experiments, high-temperature experiments pose a number of additional experimental challenges. A number of articles and reviews have been written on the topic [8, 60, 61], to which the reader is referred to for a more detailed overview. The most important factors influencing the accuracy of high-temperature experiments are related to thermal drift, thermal matching, indenter material and indenter-sample reactions. The development of in-situ devices capable of testing inside vaccuum chambers of SEMs and TEMs have already drastically reduced oxidation issues and increased the thermal stability of the systems compared to ambient conditions. The capability

of monitoring the deformation during testing is another great advantage. Figure 1.8 gives a schematic overview of a typical nanomechanical device used for in-situ high-temperature experiments inside an SEM.

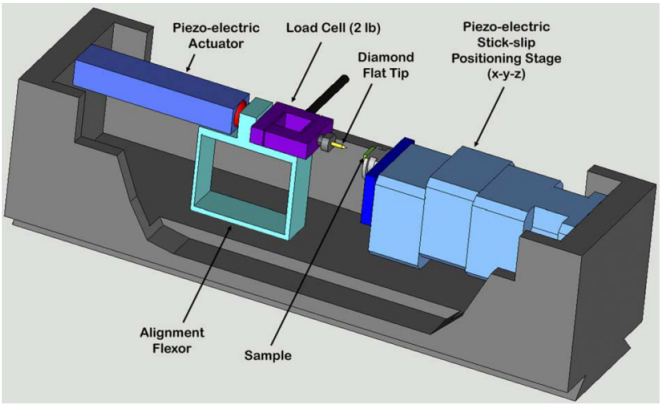


Figure 1.8: Schematic overview of the lay-out of a typical nanomechanical device used for in-situ testing inside a SEM [7].

The displacement drift induced by heat flow and thermal fluctuations inside the testing chamber is undisputedly the most dominant factor to be controlled when measuring displacements on the nanoscale. These thermally induced expansions and/or contractions can lead to inaccuries of the measured displacement. Two types of drift are often distinguished: frame drift and contact drift [8,60]. To mitigate drift a high thermal stability of the frame away from the tested region is required as well as thermal matching of the indenter and sample at the point of contact. Frame drift is often resolved by introducing a stabilization period before starting the experiments. For accurate thermal matching individual heating of sample and indenter is the first important requirement of the system. Multiple procedures have been addressed to further minimize temperature differences as a result of thermal gradients between the point of contact and the thermocouples. For more detailed information on these calibration procedures the reader is referred to the previously cited papers. Figure 1.9 gives an overview of other factors affecting the contact drift and drift direction, which include the contact area and thermal conductivity of the material.

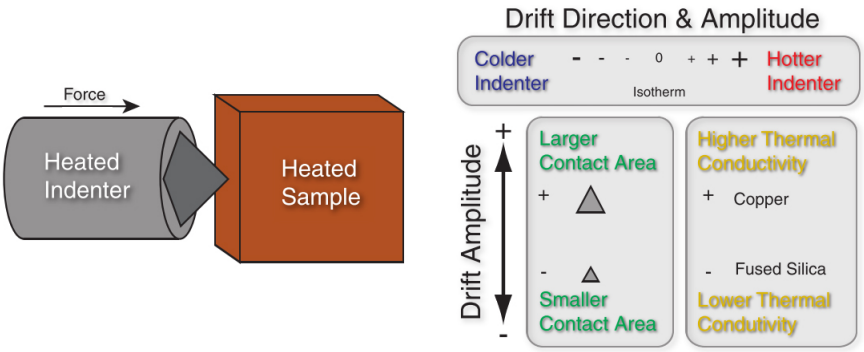


Figure 1.9: Direction and magnitude of drift as a function of indenter temperature, contact area and thermal conductivity. [8]

The choice of indenter material is mainly based on the hardest and stiffest material available, ensuring the lowest amount of damage and wear to the indenter [62]. At room-temperature diamond is

often the material of choice. However at elevated temperatures hot-hardness and chemical reactivity become increasing important. For example diamond, which is the most-used indenter material at room-temperature, can show oxidative damage at temperatures of $400\,^oC$ and higher and loses its hardness quicker than other materials at elevated temperatures. Furthermore it has to be ensured that for the given indenter-sample material combination no chemical reactions occur at the test temperatures.

## 1.4 Scope and outline of the thesis

The presented literature has shown that the mechanical properties and deformation behaviour of ARB Cu/Nb are relatively unexplored compared to PVD Cu/Nb. The majority of studies either focus on the interface texture evolution during manufacturing or atomistic modeling revealing the role of the interface texture in the dislocation-related deformation processes. Empirical results are very limited, especially studies by micropillar compression. Furthermore, in relation to their potential applications in nuclear reactors, not much is known about the thermo-mechanical behaviour of the material.

The above arguments have motivated this thesis project. First in Chapter 2 an overview of the experimental techniques used within this project is given. The core of the thesis is divided into three chapters. In Chapter 3 the results of a small study on the effect of pillar taper and microstructure on yield strength and strain-rate sensitivity is presented. The purpose of this study was to understand to which extent the experimentally determined material parameters were sensitive to experimental artefacts such as taper and/or microstructural variations in the pillars. In Chapter 4 the room-temperature behaviour of the material is studied. The emphasis is on the role of layer thickness on multilayer strength and deformation behaviour, with a small section devoted to the different results obtained from micropillar compression and nanoindentation. In Chapter 5 the high-temperature behaviour of the material is studied. The emphasis is on the role of layer thickness and temperature on the rate-controlling mechanisms of deformation in the multilayer. The main conclusions and recommendations for further research are given in Chapter 6. In the Appendix an overview is given of the Matlab script developed to process the experimental data.

# Chapter 2

# Experimental techniques

This chapter given an overview of the experimental techniques, equipment and set-ups used within this project.

## 2.1 Fabrication of Cu/Nb multilayers

Cu/Nb ARB samples were manufactured by Los Alamos National Laboratory (New Mexico, United States) according to the ”copper-clad” method. In this method alternating layers of Cu and Nb with equal layer thickness are bounded by two half-thick Cu layers [1] such that no new Cu/Nb interfaces are formed during the restacking step. By rolling, cutting, stacking and rerolling, samples with average layer thickness in the range of micrometers to nanometers can be obtained. Figure 2.1 gives a schematic overview of the ARB process and an image showing the reduction in individual layer thickness after each rolling pass. ARB Cu/Nb samples with average layer thickness of 7, 16, 34 and 63 nm were supplied. The same rolling direction was maintained during all reduction steps and no intermediate annealing steps were carried out.

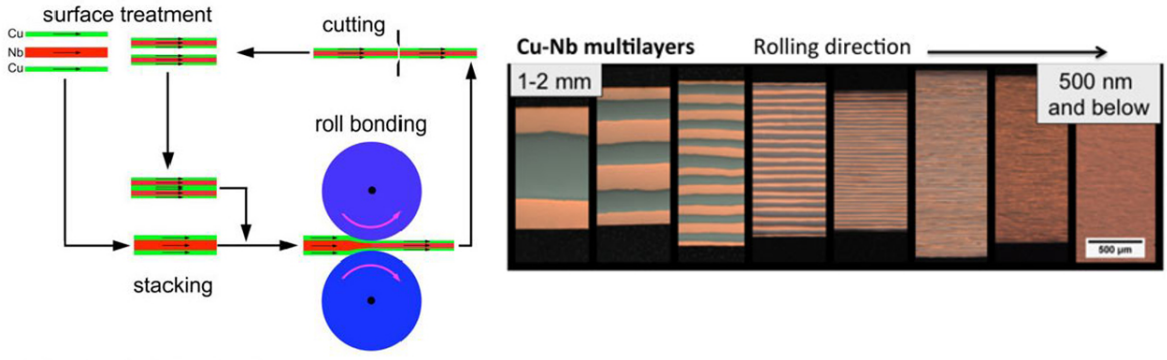


Figure 2.1: Schematic of the ARB production process (left) and Cu/Nb ARB samples manufactured with different individual layer thicknesses (right). [1, 9]

Multiple studies have shown the formation of a preferred $\{112\}Cu||\{112\}Nb$ interface texture in ARB Cu/Nb during rolling reductions [38–41], with the transition occurring at individual layer thickness of approximately 700 nm [41]. All samples were assumed to contain the dominant $\{112\}Cu||\{112\}Nb$ interface texture. No further interfacial analysis has been performed to confirm this. Furthemore top-down ARB manufacturing of multilayers is known to result in samples with significantly higher microstructural

variation compared to multilayers manufactured by PVD. Variations in thickness within layers and between different layers are characteristic for samples processed by this technique, and are a result of the lack of control on a microstructural level during the fabrication process. Although no statistics were available on the layer thickness variations of the current ARB batch, a different batch studied by Los Alamos showed typical variance of 1-8% of the average layer thickness for the current layer thickness range[1] [9]. When performing micropillar compression these microstructural variations are an important consideration when choosing the pillar size, as further discussed in Section 2.3.2.

## 2.2 Sample preparation

In order to prepare the sample surface for nanoindentation and the FIB fabrication process, sample surfaces were grinded and polished. Figure 2.2 gives an overview of the utilities used for sample preparation. One of the challenges of preparing surfaces of multilayered materials is polishing parallel to the layers. To ensure even polishing, three smaller samples with sub-centimeter dimensions were cut from each sample using a wire-cutting tool and glued to an aluminium holder with thermal-setting wax (crystalbond). Cutting was performed perpendicular to the thickness direction to minimize bending of the sample while cutting. The surfaces were grinded in three stages using P1200, P2000 and SiC1200/4000 sandpaper. Polishing was performed in two stages using respectively $3\,\mu m$ diamond paste and $1\,\mu m$ diamond paste. Surface quality was monitored under an optical microscope during the process. After polishing the samples were removed from the aluminium holder using acetone and ultrasonically cleaned in ethanol for 2 minutes. Samples were then mounted to an SEM holder using silverpaint.

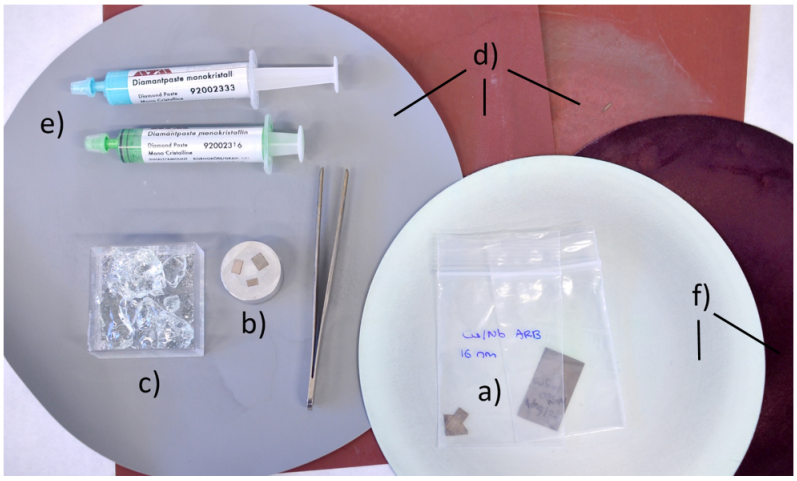


Figure 2.2: (a) Samples as received from Los Alamos National Laboratory. (b) Cut samples placed on an aluminium holder. (c) Crystal bond. (d) Sandpaper for grinding. (e) Diamond paste with different grain sizes. (f) Polishing pads

## 2.3 Fabrication of micropillars

This section outlines the micropillar fabrication process.

### 2.3.1 Equipment & fabrication method

The micropillars were manufactured using a FEI Helios Nanolab 600i DualBeam FIB-FEGSEM. This system contains both an electron beam and an ion beam, and can therefore be simultaneously used for

[1] Average thicknes was characterized by a lognormal distribution, showing more thicker layers than thinner layers.

imaging (SEM) and nanofabrication (FIB). Figure 2.3 shows a schematic diagram of the configuration of the FIB and SEM. The ion-beam has a $52^o$ offset from the electron beam. It uses $Ga^+$ ions for milling and by controlling the acceleration voltage (0.5 - 30 keV) and probe current (1 pA - 65 nA) the speed of the ions impacting the surface and the beam diameter ($\pm$5 - 500 nm) can be controlled.

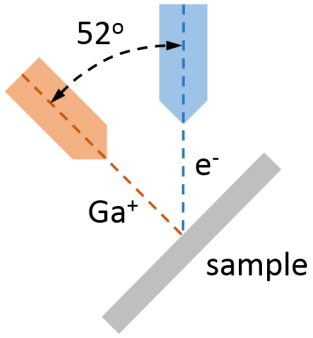


Figure 2.3: Schematic diagram of the configuration of the FEI dualbeam FIB-FEGSEM. The sample is tilted to $52^o$ such that the sample surface is oriented at $90^o$ to the ion beam (annular milling). Electron imaging takes place at $52^o$.

The micropillars were fabricated by annular milling in which milling occurs with the ion-beam normal to the surface ($90^o$). Compared to lathe milling[2], annular milling is a much faster process and results in less ion-implantation. Disadvantage of annular milling is the presence of taper in the fabricated pillars which complicate the stress-strain analysis [63]. Post-milling taper reduction is therefore a necessity.

### 2.3.2 Pillar geometry and size

Pillars with rectangular geometry and square cross-section were chosen for testing. Although within the engineering community cylindrical pillars are the most used, motivation for this choice of geometry is often not present. One can imagine that the absence of sharp corners compared to rectangular pillars mitigates stress concentrations. However, a study by Kiener et al. on single crystal Cu(100) and MgO showed negligible differences between cylindrical and rectangular pillars [64]. In other aspects rectangular pillars show several advantages:

- **Taper reduction:** reduction of taper on rectangular micropillars is much easier and faster. Whereas in cylindrical pillars the taper is reduced by rotating the pillar in small increments of a few degrees around its axis, in rectangular pillars only several rotations are needed to reduce taper on all four pillar walls.
- **Determination of shear bands and/or shear failure:** determining the angle of shear bands or shear failure is easier on a flat surface (square pillar) than on a curved surface (circular pillar), where the curvature causes visual distortion of the slip/shear line.

Due to the microstructural variations in ARB Cu/Nb multilayers relatively large pillars were manufactured. By capturing a larger pillar volume the microstructural differences between individual pillars diminishes and experimental scatter is reduced. Pillars with top cross-sectional area of $\pm$5 x 5 $\mu m^2$ and aspect ratio of 2-3[3] were chosen.

[2] In lathe milling the ion beam is at an angle to the sample surface ($< 90^o$). This method requires the rotation of the micropillar in steps of a few degrees in between each milling pass. Due to the many rotations and realignments of pillar and ion-beam, scripts for lathe milling are often complex and the process is time-consuming. Advantage of lathe milling is the fabrication of near taper-free pillars.

[3] Based on finite-element studies on the buckling behaviour of micropillars [65] an aspect ratio of 2-3 was found to be ideal

### 2.3.3 Milling of micropillar

Micropillars were fabricated by annular milling according to an in-house milling script in a three-stage process with decreasing current probe density:

- **Stage 1. (47 nA):** a large crater of $\pm 40\ \mu m$ x 40 $\mu m$ is milled at high current probe density around the location of the micropillar (Figure 2.4a). The crater facilitates imaging of the pillar by removing the surrounding material.
- **Stage 2. (9.3 nA):** a second crater of $\pm 20\ \mu m$ x 20 $\mu m$ is milled within the first crater and around the existing top-section of the micropillar (Figure 2.4b). The crater is required to be larger than the diameter of the flat-punch indenter to prevent contact with the surrounding material during compression.
- **Stage 3. (2.5 nA):** a fine beam diameter is used to finalize the shape and size of the micropillar and reduce the surface roughness of the pillar walls (Figure2.4c)

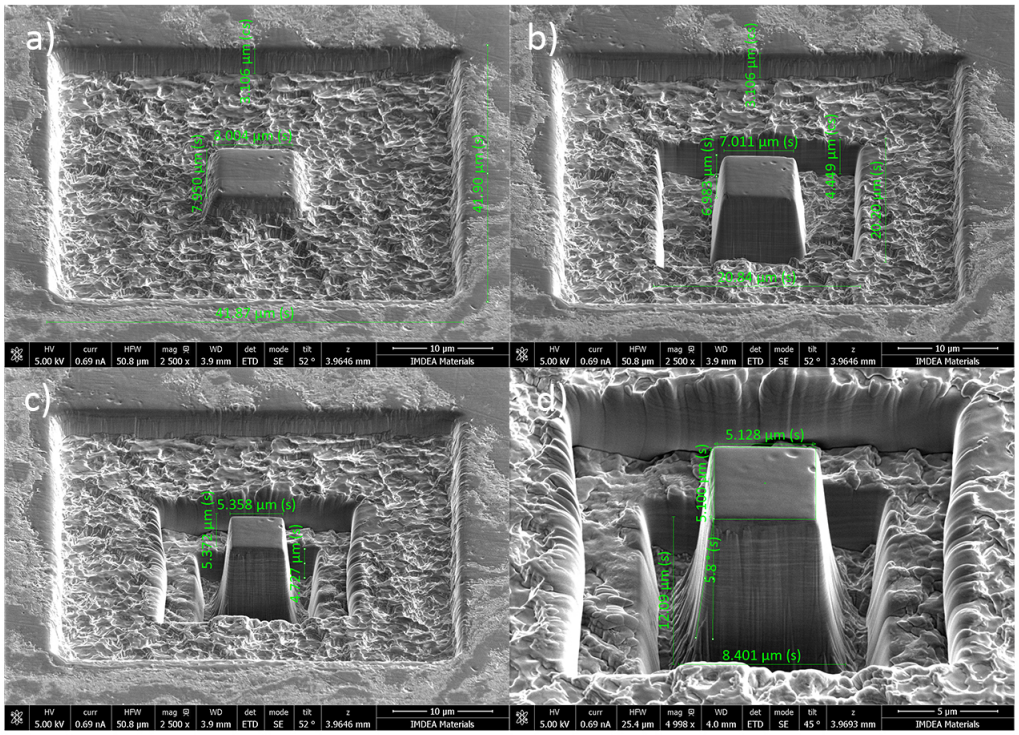


Figure 2.4: SEM images of the FIB fabrication process after: (a) stage 1, (b) stage 2 and (c) stage 3 and (d) the approximate dimensions of the tapered micropillar. Dimensions are indicative, the method for obtaining pillar dimensions is further explained in Section 2.3.4.

Figure 2.4 shows SEM images obtained after each milling stage and images of the final micropillar. Pillars have a top diameter of $\pm 5\ \mu m$, an aspect ratio of $\pm 2.5$ and a taper of $\pm 4 - 6^o$. Taper reduction was performed by tilting the specimen an additional $1 - 2^o$ with respect to the $52^o$ milling position as depicted in Figure 2.5. The area of cleaning was selected manually and taper reduction was performed at low beam current density of $0.79\ nA$ for high milling accuracy and to limit the amount of ion implantation. Depending on the tilt angle, micropillars with taper in the range of $\pm 0.5 - 4^o$ were obtained.

### 2.3.4 SEM Imaging & pillar measurements

After fabrication of micropillars electron images were taken for two purposes:

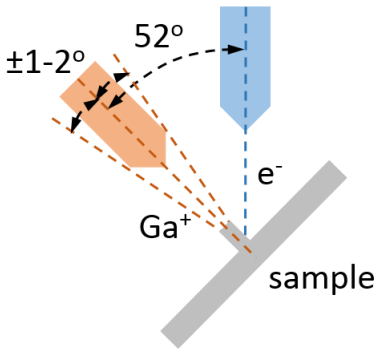


Figure 2.5: Schematic overview of the configuration for reducing taper with the ion-beam tilted an additional $\pm 1 - 2^o$ with respect to the normal milling direction.

- **Capture the microstructure:** Images of the pillar microstructure provide valuable support to explaining differences in mechanical behaviour of pillars during micropillar compression experiments.

- **Obtain pillar dimensions:** Pillar dimensions are needed for converting the experimental data (force-displacement) to stress-strain.

The top- and bottom diameters of the pillars were measured from the top-view as depicted in Figure 2.6a with which the average diameter and cross-sectional area was determined. The length of the pillar was determined according to Figure 2.6b. Pillar taper was calculated by:

$$\theta_p = tan^{-1}\left(\frac{(d_{bottom} - d_{top}}{2L_0}\right) \tag{2.1}$$

where $d_{bottom}$ and $d_{top}$ are respectively the average diameter at the bottom and top of the pillar and $L_0$ is the undeformed pillar length.

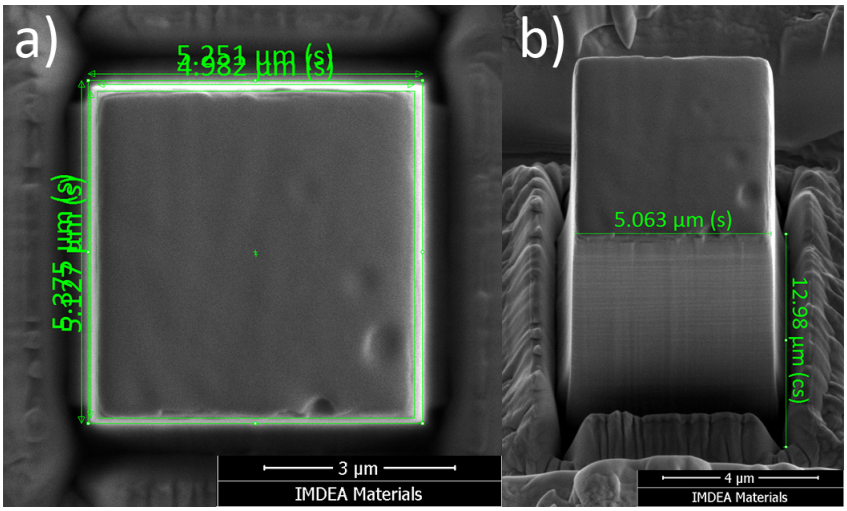


Figure 2.6: Top and bottom cross-sectional areas of the pillar are measured from the top-down view (a). Height of the pillar is measured from the side-view (b).

## 2.4 Nanomechanical testing

This section gives an overview of the equipment and set-ups used for nanomechanical testing and outlines the principles of micropillar compression and nanoindentation.

### 2.4.1 Equipment

During this research project two commercial systems for nanomechanical testing were used:

- Hysitron TI950 TriboIndenter
- Hysitron PI87 SEM picoindenter

The Hysitron TI950 TriboIndenter uses a vertical axial-loading system based on on a piezoelectric force transducer and capacitance depth-sensing indenter head[4] [5]. Figure 2.7 shows the set-up inside the testing chamber. Mounted to the granite bridge are a low-load transducer, high-load transducer and optical microscope. The low-load transducer can reach a maximum force of $12\,mN$ with force resolution $< 1\,nN$ and displacement resolution $< 0.02\,nm$. The high-load transducer is capable of reaching a maximum load of $1\,N$ with force resolution $< 1\,\mu N$ and displacement resolution $< 0.1\,nm$. The top-down view from the optical microscope ensures easy and accurate positioning of the indenter. All the hardware is embedded on an active vibration isolation system and located in a thermal and acoustic enclosure designed to minimize vibrations, thermal drift and acoustic noise during testing. Additionally a special stage can be installed for high-temperature experiments.

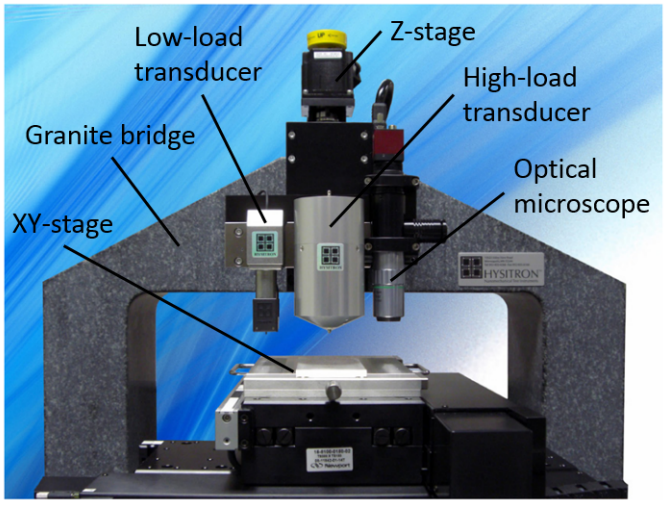


Figure 2.7: Configuration of Hysitron TI950 TriboIndenter[5]

The PI87 SEM picoindenter is a system that can be operated in-situ inside a SEM. Transducer and indenter depth-sensing technology is identical to that of the TI950 TriboIndenter. Figure 2.8 shows the configuration of the PI87 and the orientation of the system with respect to the electron beam and ion-beam in a commercial dualbeam FIB-SEM setup. The stage is responsible for movement in the XYZ-direction. Additionally the sample is located on a tilt & rotary stage for indenter alignment, giving

[4] For a more detailed description of Hysitrons' technology for nanomechanical systems the reader is referred to the Hysitron website: `http://www.hysitron.com`.

[5] Adoptation of image taken from TI 950 TriboIndenter Information Sheet, website: `https://www.hysitron.com/products-services/standalone-instruments/ti-950-triboindenter`, downloaded on: 25-12-2015.

the system 5 degrees of freedom. The system can be equipped with a low load transducer or a high load transducer. The low-load transducer has a maximum force of $30\,mN$ with force resolution $< 1\,nN$ and displacement resolution $< 0.02\,nm$. The high-load transducer can reach a maximum force of $150\,mN$, with force resolution $< 1\,\mu N$ and displacement resolution $< 0.1\,nm$. For high-temperature experiments the system is equipped with a custom hot-stage and high-temperature diamond indenter. Sample and indenter are individually heated and a water-cooling system isolates the hot-zone.

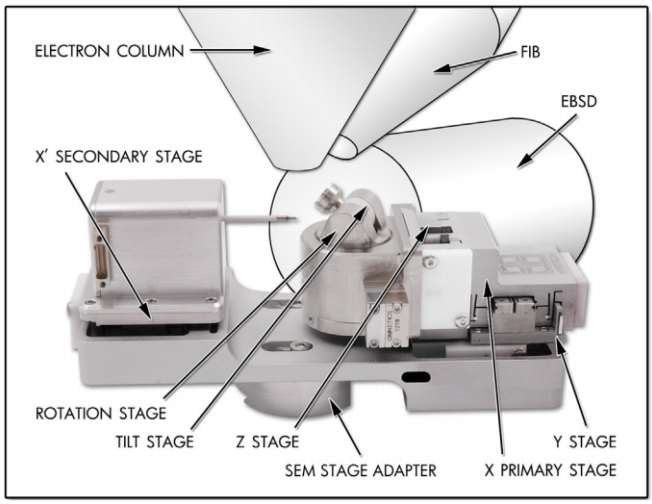


Figure 2.8: Schematic of configuration of Hysitron PI87 SEM picoindenter[6]

### 2.4.2 Micropillar compression

Micropillar compression was introduced by Uchic et al. at the beginning of this century in order to study plasticity on samples with sub-micron length scales [7, 56]. Figure 2.9 gives a schematic overview of the test set-up for micropillar compression. The micropillar is located inside a crater. For self-supportive samples the micropillar and the base material supporting the micropillar are comprised of the same material. Samples not capable of self-support often contain a substrate such as Si. Compression is performed with a diamond flat-punch indenter. Some of the challenges related to micropillar compression experiments include:

- **Elastic deflection of the substrate:** In addition to the displacements resulting from shortening of the micropillar during compression, measured displacements also include sink-in effects of the pillar into the substrate.
- **Misalignment between the flat-punch surface and the top surface of the pillar:** Non-parellel alignment between the surfaces leads to localized stress concentrations at the top of the pillar, manifested as decreased stifness at the initial loading section.
- **Tapering effect:** The increasing cross-sectional area down the axis of a tapered pillar causes gradual plasticity to occur complicating the stress-strain analysis. This topic is further addressed in Chapter 3.

#### Sneddon correction

In micropillar compression the measured displacements contain elastic compliances of multiple components of the pillar system. Figure 2.10 shows the contributions of the different components to the

[6]Image taken from PI 87 SEM PicoIndenter information sheet, website: `https://www.hysitron.com/products-services/instruments-for-microscopes/pi-8x-sem-picoindenter`, downloaded on: 25-12-2015.

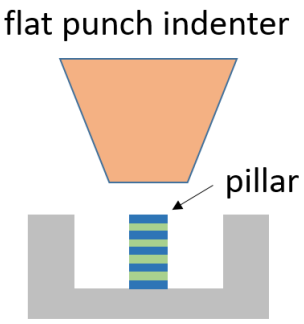


Figure 2.9: Schematic overview of the test set-up for micropillar compression experiments. Micropillar is located inside a crater and compressed with a flat-punch indenter. Crater should be large enough to facilitate the indenter head. Pillar is supported either by the same material or by a substrate.

measured displacements for an Al/SiC micropillar [10]. After the elastic and plastic deformation of the micropillar, the most dominant contribution is from the sink-in effect of the pillar into the substrate. Other effects such as elastic deformation of the indenter and pillar base radius only play a minor role.

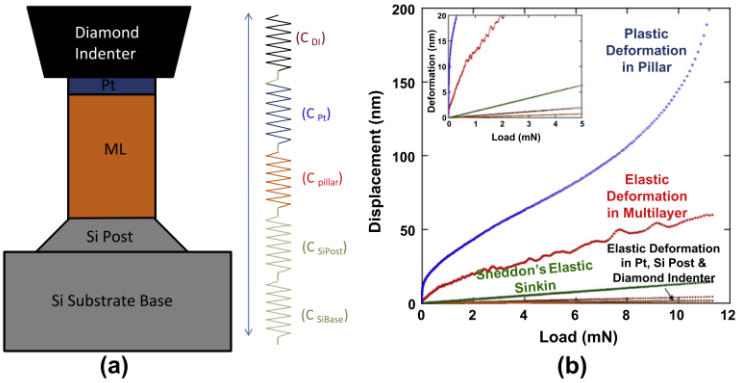


Figure 2.10: (a) Pillar system used by Singh et al. for Al/SiC multilayer with Si substrate and Pt coating. (b) Contributions of the individual components of the pillar system to the total measured displacement [10].

Based on this contributions from the indenter head and the pillar base radius are assumed negligible. The pillar displacement is then related to the measured displacement by:

$$C_p = C_m - C_s \tag{2.2}$$

where $C_p$ is the pillar compliance, $C_m$ the measured compliance and $C_s$ the substrate compliance. The substrate compliance ($C_s$) is given by the Sneddon correction [66]:

$$C_s = \frac{\sqrt{\pi}(1-\nu_s^2)}{2E_s\sqrt{A_s}} \tag{2.3}$$

where $\nu_s$ is the Poisson's ratio of the substrate, $E_s$ is the E-modulus of the substrate and $A_s$ is the cross-sectional area at the pillar-substrate interface. The Sneddon corrected pillar displacement is then given by

$$u_p = u_m - PC_s \tag{2.4}$$

where $P$ is the force.

### Initial-plasticity correction

Misalignments between the pillar surface and the head of the flat-punch indenter can lead to high stresses and local plasticity as depicted in Figure 2.11. In the compression curve this is reflected as a section with reduced initial loading stifness [67]. Initial plasticity is corrected by extrapolation of the curve when full contact between pillar and indenter head is established. A more detailed description of the procedures for extrapolation is found in the Appendix.

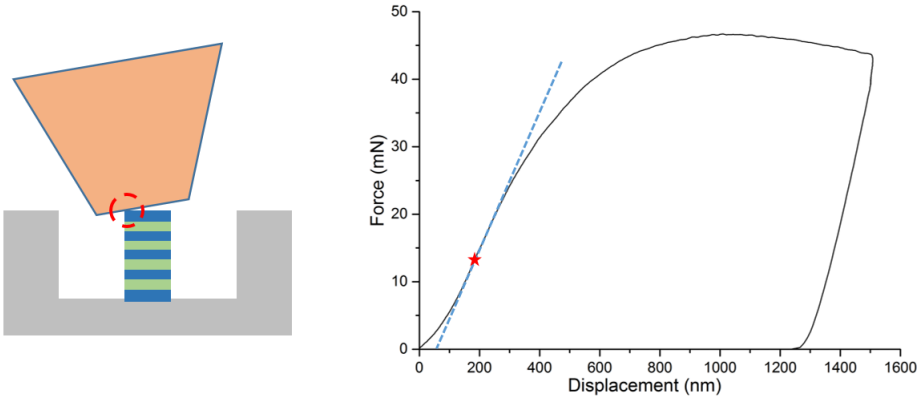


Figure 2.11: Schematic overview of pillar misalignment (left) and the reduced stifness at initial loading observed in the compression curve (right).

### Stress-strain conversion

For conversion of the measured force and displacement to stress and strain the pillars were assumed to be perfect prisms of length $L_0$ and square cross-sectional area $A_0$ corresponding to the top cross-sectional area of the pillar. The engineering stress $\sigma_eng$ and engineering strain $\epsilon_{eng}$ were calculated respectively by

$$\sigma_{eng} = \frac{P}{A_0} \tag{2.5}$$

$$\epsilon_{eng} = \frac{u_p}{L_0} \tag{2.6}$$

where $P$ is the force and $u_p$ is the pillar displacement (after Sneddon correction). True stress-strain was calculated by assuming constant volume during deformation as depicted in Figure 2.12.

The cross-sectional area $A_p$ is then related to the pillar displacement $u_p$ by

$$A_p = A_0 \frac{L_0}{L_0 - u_p} \tag{2.7}$$

Rearranging terms and substituting the equation into Equation 2.5 gives the following expression for the true stress $\sigma_{true}$

$$\sigma_{true} = \frac{P}{A_0}\left(1 - \frac{u_p}{L_0}\right) \tag{2.8}$$

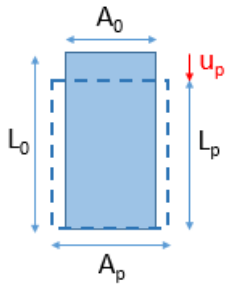


Figure 2.12: Schematic overview of the constant volume assumption and its effect on instantaneous pillar length and cross-sectional areas.

The true strain is given by:

$$\epsilon_{true} = ln\Big(1 - \frac{u_p}{L_0}\Big) \tag{2.9}$$

### 2.4.3 Nanoindentation

In general nanoindentation experiments are easier and faster to perform than micropillar compression. No micropillars have to be fabricated, samples can easily be tested at multiple locations on the surface and it is less sensitive to indenter-sample misalignments. The principles of operation of nanoindentation are very similar to micropillar compression, however the interpretation of data is more complex. In nanoindentation a tip with well-defined geometry is pushed into the sample surface. This technique relies on accurate knowledge of the indenter geometry to determine the contact area with the material while indenting, the well-known Oliver-Pharr method [11]. Figure 2.13 shows a schematic overview of the cross-section of an indent. When the material is loaded an indent with depth $h$ is formed. When unloaded a residual indent of depth $h_f$ is left behind.

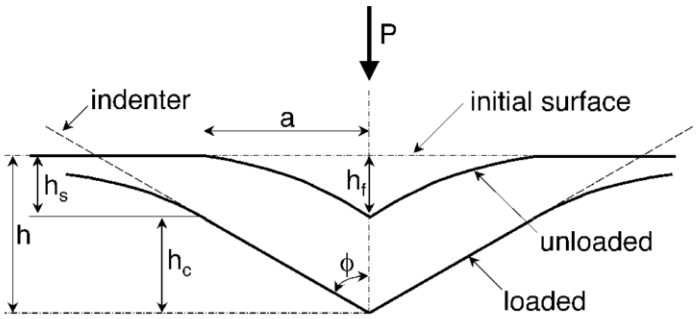


Figure 2.13: Schematic overview of the deformation and residual imprint during indentation. While loading an indent with depth $h$ is formed. Upon removal of load a residual imprint is left with depth $h_f$. Hardness and E-modulus are measured during elastic unloading. [11]

#### Governing equations

The governing equations for analysis of nanoindentation data are significantly different from that of micropillar compression. The procedures used to calculate hardness and E-modulus are based on the unloading processes. The amount of sink-in $h_s$ is given by

$$h_s = \epsilon \frac{P_{max}}{S} \tag{2.10}$$

where $\varepsilon$ is a constant that depends on the geometry of the indenter (Berkovich=0.72). The depth along which contact is made between the indenter and the material, referred to as the depth of elastic unloading $h_c$, is given by

$$h_c = h_{max} - \epsilon \frac{P_{max}}{S} \tag{2.11}$$

where $h_{max}$ is the indentation depth with respect to the undeformed surface. The contact area $A_c$ is a function of the contact depth $h_c$ and is generally calculated by indenting a material with well-known elastic modulus (e.g. fused silica) at different depths. The following curve is then fitted to determine the relation between contact depth and contact area

$$A_c = C_0 h_c^2 + C_1 h_c + C_2 h_c^{1/2} + C_3 h_c^{1/4} + C_4 h_c^{1/8} + C_5 h_c^{1/16} \tag{2.12}$$

where $C_0$ is related to the shape of the indenter (for Berkovich $C_0$ = 24.5). $C_1$-$C_5$ are constants used for data fitting. The hardness is determined by

$$H = P_{max}/A_c \tag{2.13}$$

where $A_c$ is the contact area at maximum load. Alternatively the instantaneous hardness can be determined, which is given by the instantaneous force $P$ divided by the instantaneous area $A_i$

$$H_i = P/A_i \tag{2.14}$$

The stifness $S$ is defined as

$$S = \left.\frac{dP}{dh}\right|_{h_{max}} \tag{2.15}$$

The reduced modulus $E_r$ which includes elastic contributions of the sample and the indenter, is given by

$$E_r = \frac{\sqrt{\pi}}{2} \frac{S}{\sqrt{A_c}} \tag{2.16}$$

The effective E-modulus $E$ of the material is given by

$$E = \left(1 - \nu^2\right)\left(E_r - \frac{E_i}{\left(1 - {v_i}^2\right)}\right) \tag{2.17}$$

where $\nu$ is the Poisson's ratio of the material, $E_i$ and $\nu_i$ are respectively the E-modulus and Poisson's ratio of the indenter.

### 2.4.4 CSR & SRJ tests

Two types of load functions were used during the compression and indentation experiments. In constant strain-rate (CSR) tests the strain-rate is held constant during the full compression/indentation test. Material parameters such as yield strength and E-modulus can be directly determined from these tests. By performing multiple tests at different strain-rates, the strain-rate sensitivity can also be determined. However, this method for determining the SRS is limited to materials showing medium-to-high strain-rate

sensitivity and small experimental scatter. In ARB Cu/Nb relatively high experimental scatter is present due to the microstructural variations. CSR experiments are therefore not suitable for determining strain-rate sensitivities.

An alternative to CSR tests are strain-rate jump (SRJ) tests. In these tests the material is deformed at discrete strain-rates within the same compression. Since the same ”sample” is tested at different strain-rates, it is supposed that the measured strain-rate sensitivities are free of microstructural influences. Examples of compression curves obtained by CSR and SRJ tests are given in Figure 2.14. The method for determining the SRS from SRJ tests is explained in Section 2.4.5.

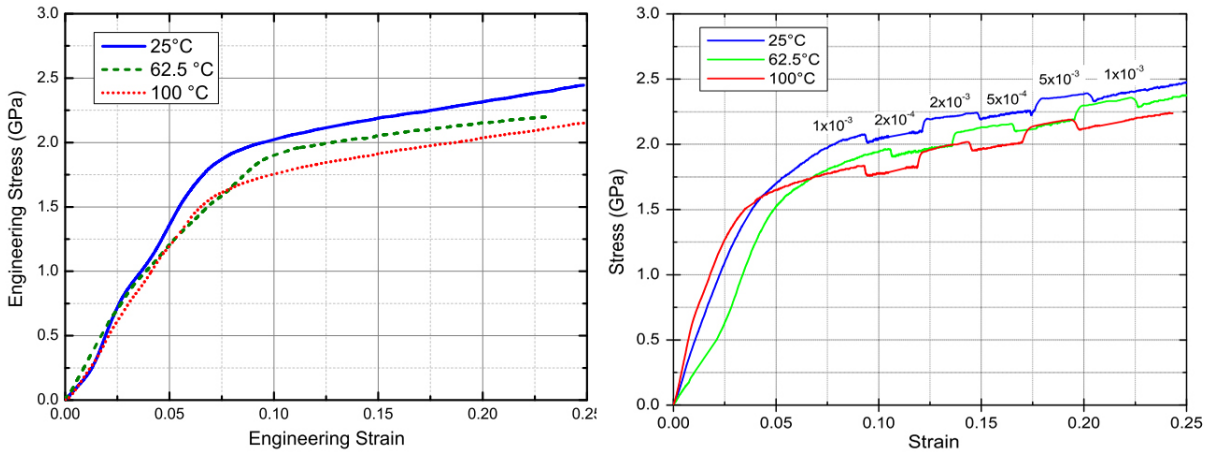


Figure 2.14: Examples of micropillar compression stress-strain curves obtained from CSR tests (left) and SRJ tests (right) at different temperatures. The SRJ tests clearly show the jumps in flow stress due to change in strain-rate. [12]

Provided that the plastic strain is low, a constant strain rate in micropillar compression experiments is defined as

$$\dot{\epsilon} = \frac{\dot{u}}{L_0} = const. \tag{2.18}$$

where $\dot{u}$ is the displacement-rate and $L_0$ is the undeformed pillar length. In nanoindentation experiments, a constant strain-rate is defined as

$$\dot{\epsilon} = \frac{\dot{h}}{h} = const. \tag{2.19}$$

where $h$ is the indentation depth. In nanoindentation the strain-rate is a function of the indentation depth, the displacement-rate therefore needs to increase in order to maintain a constant strain-rate.

### 2.4.5 Material parameters

This section gives an overview of the material parameters determined from the experiments.

#### Yield strength & strain-hardening

The yield strength is an important parameter since it defines the transition from elastic to plastic behaviour of the material. In micropillar compression experiments the yield strength is defined as the

stress at 0.2% plastic strain ($\sigma_{0.2\%}$). In nanoindentation experiments hardness is generally related to the strength by the Tabor factor. However this factor generally corresponds to flow stresses at 7-8% plastic strain, and therefore corresponds more to flow stresses in uniaxial compression tests. The relation between flow stresses $\sigma_f$ and hardness $H$ is given by

$$\sigma_f = H/cf \tag{2.20}$$

where $cf$ is the Tabor or constraint factor which is generally in the range of 2.7-3.

The dislocation induced strengthening during plastic deformation known as strain-hardening is an important parameter for describing the dislocation activity inside the crystal. The work-hardening relation between stress and plastic strain follows a power law relation given by the Hollomon's equation

$$\sigma = K\epsilon_p^n \tag{2.21}$$

where $\sigma$ is the stress, $K$ is the strength coefficient, $\epsilon_p$ is the plastic strain and $n$ is the strain-hardening exponent.

**Strain-rate sensitivity**

The strain-rate sensitivity of plastic flow of a material is based on the response of the underlying deformation mechanisms to a change in stress or strain-rate. It is derived from the Mukherjee, Bird and Dorm (MBD) equation for creep which reflects influences of temperature, microstructure and rate-controlling deformation mechanisms on the steady-state strain-rate of the material. The MBD equation is given by [22]

$$\dot{\epsilon} = A\frac{DGb}{kT}\left(\frac{b}{d}\right)^p\left(\frac{\sigma}{G}\right)^n \tag{2.22}$$

where $\dot{\epsilon}$ is the steady-state strain rate, $D$ is the appropriate diffusivity (lattice or grain boundary), $G$ is the shear modulus, $b$ is the Burgers vector, $k_b$ is the Boltzmann constant, $T$ is the temperature in Kelvin, $d$ is the grain size, $p$ is the grain size exponent, $\sigma$ is the applied stress and $n$ is the creep exponent of the flow stress. The diffusivity, strain rate sensitivity and factor $A(b/d)^p$ are creep mechanism dependent. Under constant temperature and microstructure, the relation between strain-rate and stress level reduces to $\dot{\epsilon} = \sigma^n$ and the strain-rate sensitivity $m$ is defined as

$$m = \frac{ln(\sigma_2/\sigma_1)}{ln(\dot{\epsilon}_2/\dot{\epsilon}_1)} \tag{2.23}$$

where $m = 1/n$ and ($\sigma_1$,$\sigma_2$) and ($\dot{\epsilon_1}$,$\dot{\epsilon_2}$) reflect the changes in flow stress due to changes in applied strain-rate or visa versa. Typical strain-rate sensitivity values for different creep mechanisms are given in Table 2.1.

Within this research project strain-rate sensitivities are determined by strain-rate jump tests. The method for determining flow stresses is depicted in Figure 2.15. The flow stress before the jump is given by $\sigma_1$. The flow stress $\sigma_2$ after the jump is determined by fitting a linear line to the steady strain-rate regime $\dot{\epsilon}_2$ and extrapoling to the strain-rate jump point.

Table 2.1: Creep mechanisms [22]

| **Mechanism** | **Diffusivity (D)** | $A(b/d)^p$ | **n** |
|---|---|---|---|
| Nabarro-Herring creep | Volume by vacancy exchange | $7(b/d)^2$ | 1 |
| Coble creep | Grain boundary by vacancy exchange | $50(b/d)^3$ | 1 |
| Weertman climb (FCC) | Volume by vacancy exchange | $\sim 2.5x10^-6$ | 4.2-5.5 |
| Weertman climb (BCC) | Volume by vacancy exchange | $\sim 2.5x10^-6$ | ~4.5 |
| Superplastic creep | Volume by vacancy exchange | $\sim 100(b/d)^3$ | 2 |

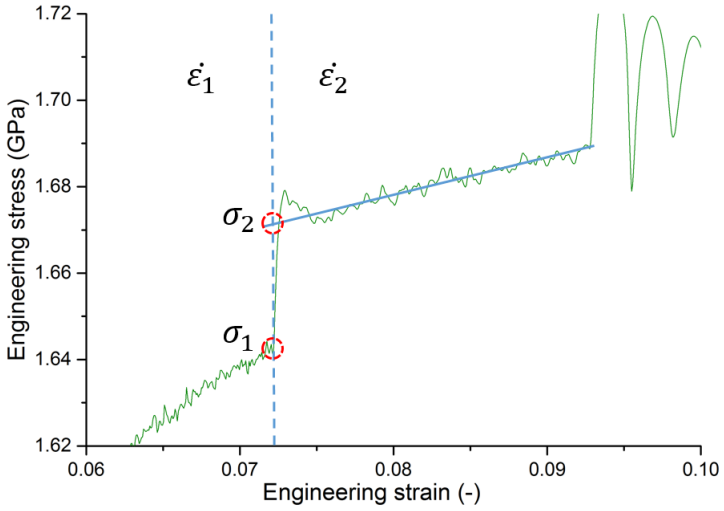


Figure 2.15: Method for determining strain-rate sensitivity from strain-rate jump tests. A linear curve is fitted to the constant strain-rate segment after the jump and extrapolated to the jump strain. Stress levels $\sigma_1$ and $\sigma_2$ are determined and strain-rate sensitivity is calculated from Equation 2.23

### Activation volume

The activation volume $V$ is a physical quantity that gives an indication of the physical volume involved in the rate-controlling deformation processes. It is given by

$$V = \frac{\sqrt{3}kT}{m\sigma_y} \tag{2.24}$$

where $k$ is the Boltzmann constant, $T$ is the absolute temperature (degrees K), $m$ is the strain-rate sensitivity and $\sigma_y$ is the yield stress. Alternatively the activation volume can also be written as [68]:

$$V = \sqrt{3}kT\frac{\partial ln(\dot{\epsilon})}{\partial \sigma_f} \tag{2.25}$$

The specific activation volume is given by

$$V^* = \frac{V}{b^3} \tag{2.26}$$

where $b$ is the magnitude of the Burgers vector. Typical activation volumes and their corresponding deformation mechanisms are given in Table 2.2.

Table 2.2: Activation volumes of common deformation mechanisms [13, 23]

| **Deformation mechanism** | **Activation volume ($V^*$)** |
|---|---|
| Grain boundary diffusion | $1 - 10b^3$ |
| Dislocation nucleation | $1 - 10b^3$ |
| Confined layer slip | $10 - 100b^3$ |
| Dislocation glide | $100 - 1000b^3$ |
| Dislocation forest cutting | $> 1000b^3$ |

#### Activation energy

For each type of deformation, whether dislocation glide, grain boundary sliding or diffusion, obstacles are present which act as energy barriers to deformation. Mechanisms with high activation energy generally have higher strain-rate sensitivities since the probability of an atom overcoming an obstacle is larger at low strain-rates than at high strain-rates[7]. The energy at which all atoms overcome the barrier independent of strain-rate is the activation energy. The activation energy follows from the relation between strain-rate $\dot{\epsilon}$ and applied stress $\sigma$ through an Arrhenius formulation [12]

$$\dot{\epsilon} = A\sigma^n e^{\frac{Q}{RT}} \tag{2.27}$$

where $A$ is a pre-exponential constant, $n$ is the creep exponent, $R$ is the gas constant and $T$ is the temperature in Kelvin. Taking the logarithmic on both sides, the equation reduces to

$$log(\dot{\epsilon}) = log(A) + nlog(\sigma) - \frac{Q}{RT} \tag{2.28}$$

### 2.4.6 Data processing

As outlined in the previous sections several corrections and conversions had to be applied to the raw data before material parameters could be extracted. In order to consistently process the data and obtain the parameter values a Matlab script was developed. Its use has proven very valuable, and a description of the script and the processing steps are given in the Appendix.

[7] The high number of total atomic vibrations in experiments at low strain-rate increases the probability of one of the vibrations to overcome the energy barrier.

# Chapter 3

# Effect of pillar taper and microstructure on yield strength and strain-rate sensitivity

## 3.1 Motivation

Pillar taper is an experimental artefact known to influence the stress-strain fields of a micropillar during compression. Whereas taper-free pillars show a relative homogeneous stress-strain state along the pillar length, in tapered pillars the non-homogeneous cross-sectional area leads to a more complex stress-strain state, complicating the actual stress-strain measurements and related mechanical properties such as yield strength and E-modulus [69]. In order to obtain "correct" values for yield strength and E-modulus, taper-free pillars are the unique choice. However, a slight taper is generally desired for geometrical stability. Especially in multilayered materials where mechanical properties are highly layer orientation dependent, rotation of layers due to instability or strain localization can strongly affect the outcome of compression experiments. A taper-related conflict of interest therefore exists between determination of material parameters and geometrical stability of the pillar. Additionally, the microstructure of ARB manufactured multilayers are known to have significant variation in layer thickness. The extent to which these influence the yield strength and strain-rate sensitivity is currently unknown. The objective of this small study is to get an understanding of the mutual effects of taper and microstructure on the yield strength and strain-rate sensitivity obtained from micropillar compression experiments.

## 3.2 Experimental overview

Room-temperature compression experiments were performed on ARB Cu/Nb micropillars with average individual layer thickness of 63 nm and taper of $\pm 1^o$, $2^o$ and $3^o$. Table 3.1 gives an overview of the average dimensions of the pillars. Using the average layer thickness and the dimensions of the smallest pillar, a minimum of 200 layers were present in each pillar. Cu/Nb with layer thickness of 63nm was chosen since previous compression experiments showed homogeneous deformation without strain localization, as opposed to the multilayers with thinner layers. Strain localization (e.g. shear) significantly affects the flow stresses, complicating the determination of strain-rate sensitivities. A total of 12 compression tests were performed of which all were strain-rate jump tests. Strain-rates of $10^{-2}\,s^{-1}$, $10^{-3}\,s^{-1}$ and $10^{-4}\,s^{-1}$ were chosen and each compression test contained 5 strain-rate segments and 4 strain-rate jumps. Yield strength was determined at a strain-rate of $10^{-3}\,s^{-1}$. All compressions were performed with a diamond flat-punch indenter with diameter of $10\,\mu m$.

Table 3.1: Overview of average dimensions of the compressed pillars.

| Taper | Number of compressions | Average taper ($^o$) | Average diameter ($\mu m$) | Average height ($\mu m$) |
|---|---|---|---|---|
| $1^o$ | 6 | $0.8 \pm 0.2$ | $5.0 \pm 0.0$ | $13.9 \pm 0.4$ |
| $2^o$ | 4 | $2.0 \pm 0.3$ | $5.5 \pm 0.1$ | $13.5 \pm 0.5$ |
| $3^o$ | 2 | $2.8 \pm 0.1$ | $5.4 \pm 0.0$ | $13.6 \pm 0.5$ |

## 3.3 Results

SEM images of the pillars before and after deformation are presented in Figures 3.2 and 3.3. As expected all pillars showed homogeneous deformation without strain localization. Furthermore the ”mushroom-effect” is visible with deformation increasingly localizing on the top part of the pillar as taper increases. Furthermore in some of the pillars one or several thick layers were present as shown in Figure 3.2. Since thicker layers were expected to influence pillar strength, distinction was made between pillars with homogeneous microstructure and variational microstructure. This was done to separate microstructural effects fom taper effects, such that a better understanding of the individual contributions to strength and strain-rate sensitivity is obtained.

Representative compression curves of pillars with various degrees of taper and homogeneous microstructure are shown in Figure 3.1. All curves have been converted from force-displacement to engineering stress-strain by assuming a constant pillar length equal to the undeformed pillar length and constant cross-sectional area[1] throughout the compression experiment. Although these assumptions are reasonable for deformation of pillars with small taper ($\pm 1^o$), as taper increases these assumptions are not representative anymore and the calculated stress-strain curves can give misleading results.

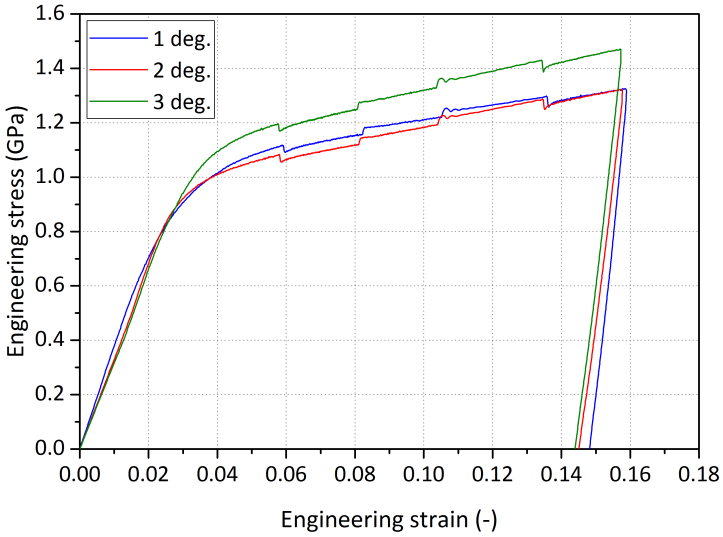


Figure 3.1: Representative compression curves of 63nm ARB Cu/Nb with different degrees of taper.

[1] The top cross-sectional area of the undeformed pillar was chosen for the stress calculations

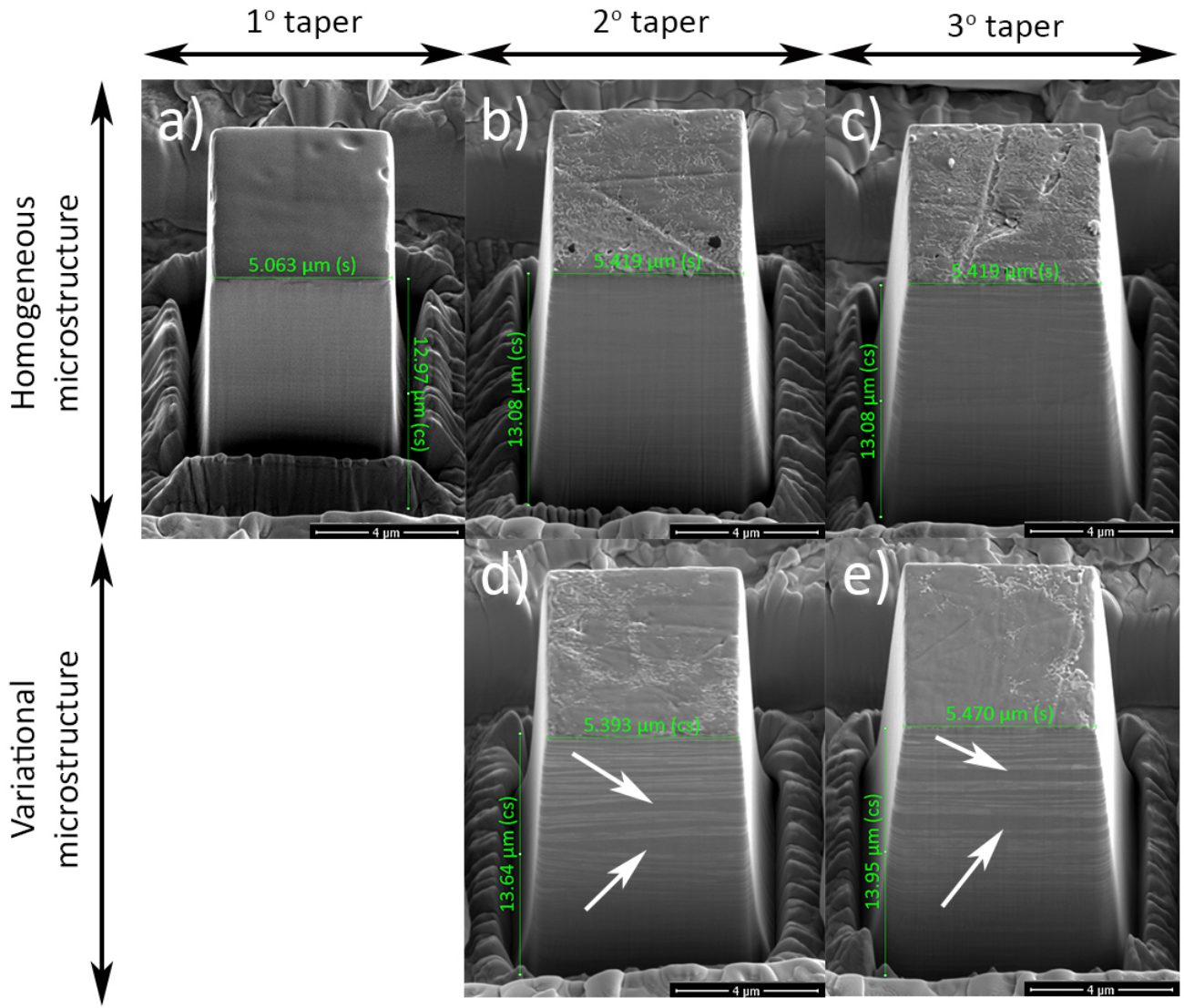


Figure 3.2: SEM images of a selection of micropillars before compression with various degree of taper. Bright layers correspond to Cu, dark layer correspond to Nb. In some of the pillars thicker Nb layers were present, as indicated by the arrows.

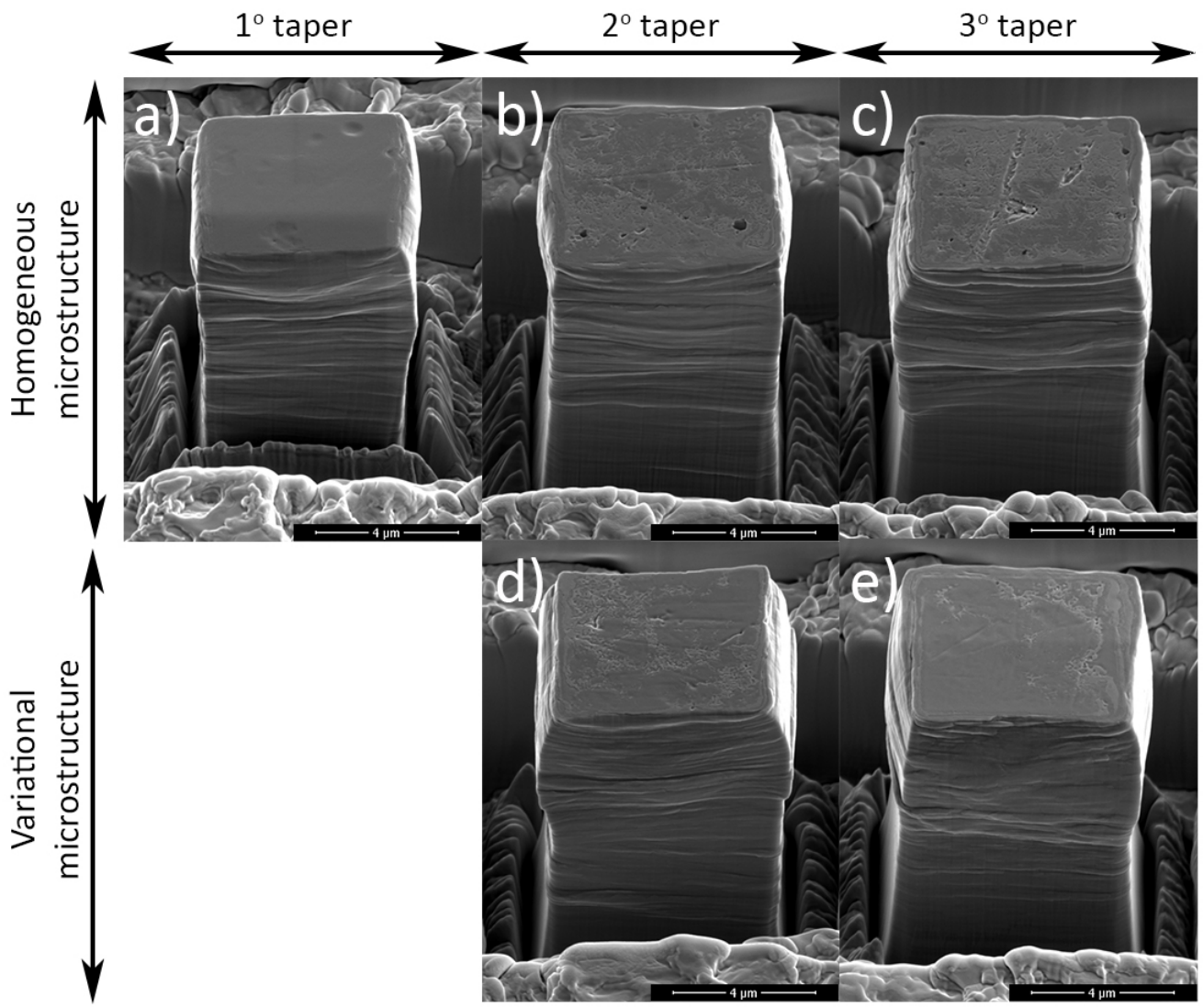


Figure 3.3: SEM images of the deformed micropillars showing increased localization of deformation on the top part of the pillar with taper. Increased extrusion of thicker layers is difficult to assess.

Comparing the curves representative for pillars with $1^o$ and $3^o$ taper, one can see that under the current assumptions taper resulted in curves with higher flow stresses and more strain-hardening. Furthermore tapered pillars should also have a higher modulus, however this was not directly visible from the curves. Due to misalignments of pillar and indenter the loading section of the curve is rarely fully elastic, which is the main reason why the elastic modulus in micropillar compression is determined from the unloading section. This however brings other uncertainties related to the cross-sectional area at unloading, which can deviate significantly from the area based on the assumptions especially in pillars compressed to high strains and/or pillars that tend to show strain localization.

The ”apparent” differences in shape and stress levels of the curves are due to taper-induced changes in stress-strain distribution. Due to the variation in cross-sectional area along the length of the pillar, a strain-gradient develops and deformation localizes on the top part of the pillar. In SEM images of deformed pillars this is often characterized by mushroom-type deformation where the top part of the pillar is wider than the bottom after deformation. Another side-effect of the inhomogenous geometry is presented by gradual yielding, in which yielding occurs gradually down the pillar axis with the top area with smallest cross-sectional area yielding first. This behaviour characteristic of tapered pillars is not reflected in the assumptions, and therefore lead to higher flow stresses and apparent strain-hardening. It is therefore important to realize that in micropillar compression the obtained stress-strain curves are not necessarily representative of material behaviour, and care has to be taken when extracting material parameters from the curves.

### 3.3.1 Yield strength

The yield strength was computed in four different ways. The most common method is based on the maximum stresses occurring at the top of the pillar. As mentioned before this method is accurate for taper-free pillars, but overestimates the yield strength when applied to tapered pillars. Different approaches are reported in literature to compensate for taper, which include stress-calculations based on average cross-sectional area, average stresses and average radius [69]. The yield strengths obtained by these methods are plotted in Figure 3.4. The eye-guide is based only on the pillars with homogeneous microstructure.

Table 3.2: Overview of yield strengths obtained by different methods, with the stress based on: $\sigma_y^{[1]}$ the top cross-sectional area of the pillar, $\sigma_y^{[2]}$ the average pillar cross-sectional area, $\sigma_y^{[3]}$ the average pillar stress and $\sigma_y^{[4]}$ the average pillar radius.

| **Taper** | $\sigma_y^{[1]}$ **[GPa]** | $\sigma_y^{[2]}$ **[GPa]** | $\sigma_y^{[3]}$ **[GPa]** | $\sigma_y^{[4]}$ **[GPa]** |
|---|---|---|---|---|
| $1^o$ | 0.80 | 0.73 | 0.74 | 0.73 |
| $2^o$ | 0.90 | 0.76 | 0.78 | 0.76 |
| $3^o$ | 1.00 | 0.78 | 0.82 | 0.79 |
| $\Delta\sigma_y/^o taper$ | 0.10 | 0.03 | 0.04 | 0.03 |

SEM images clearly revealed the presence of thicker Nb layers in two pillars, as depicted by the arrows in Figure 3.2. These pillars are marked in red and showed a significant decrease in yield strength. Pillars ’d’ and ’e’, both contained two thicker Nb layers and showed a drop in yield strength of respectively $\pm$0.1 GPa and $\pm$0.2 GPa based on Figure 3.4a. Furthermore the drop in strength of pillar ’e’, where the thicker Nb layers were located more towards the top of the pillar, is higher than that of pillar ’d’. A different pillar with $\pm 1^o$ taper and yield strength of $\pm$0.7 GPa showed a similar reduction in strength as pillar ’d’, however

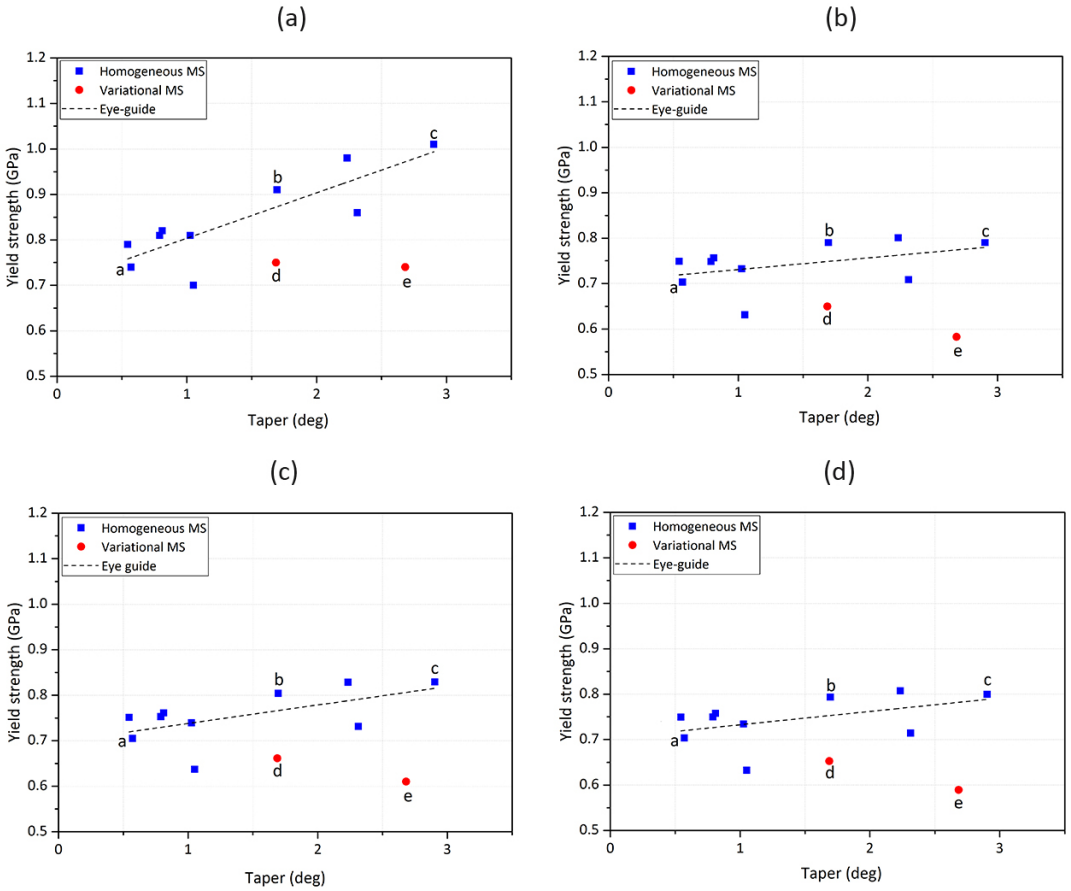


Figure 3.4: Yield stress as a function of taper obtained by: a) top cross-sectional area, b) average cross-sectional area, c) average stress and d) average radius. The eye-guide is based only on the pillars with homogeneous microstructure (MS). Data points a-e correspond to the pillars shown in Figures 3.2 and 3.3.

no clear microstructural variations were observed that could explain the lower strength. Comparing the yield strength values to that of pillars with $1^o$ taper and homogeneous microstructure, one can see that the effect of microstructure on pillar strength is of the same order as the effect of taper on pillar strength.

Now the microstructural effects have been separated, the pillars with relatively homogeneous microstructure are selected to study the effect of taper. Table 3.2 gives an overview of the yield strengths obtained per degree of taper according to the different methods presented in Figure 3.4. When using the conventional method ($\sigma_y^{[1]}$), the "apparrent" yield strength increased by 25% from $\pm$0.8 GPa at $1^o$ taper to $\pm$1.0 GPa at $3^o$ taper, corresponding to an increase of 0.1 GPa per degree of taper. When computing the yield strength based on the average cross-sectional area ($\sigma_y^{[2]}$) as shown in Figure 3.4b, these differences decreased to 0.03 GPa per degree of taper. Similar values for $\sigma_y$ and $\Delta\sigma_y$ were obtained when computing average stresses and stress at the average pillar radius. All methods predicted a yield strength of 0.7 GPa when no taper is present.

### 3.3.2 Strain-rate sensitivity

Figure 3.5 shows the strain-rate sensitivities obtained from the strain-rate jump compression tests. The pillars with varying microstructural features are marked in red. No consistent trend was observed between the presence of thicker Cu or Nb layers and deviating strain-rate sensitivities, suggesting the SRS

to be independent of microstructural variations. Furthermore the strain-rate sensitivity also seemed to be independent of taper, with the average SRS well within the scatter of the individual compressions.

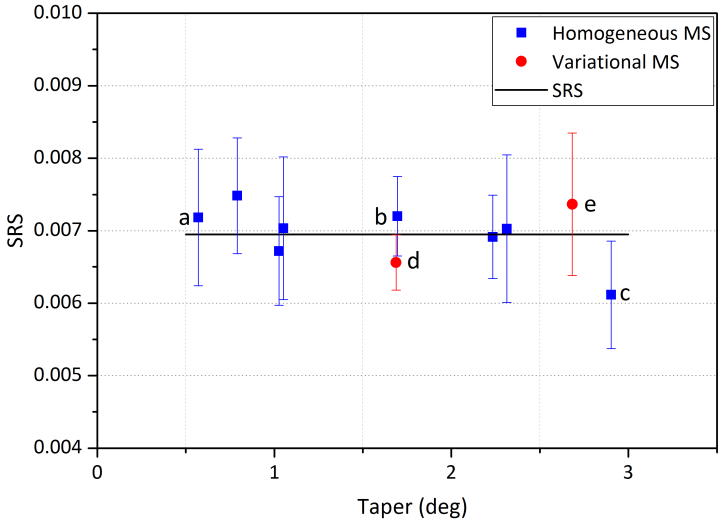


Figure 3.5: Strain-rate sensitivities obtained for 63 nm ARB Cu/Nb at different degrees of pillar taper. Each data point corresponds to one compression test containing four strain-rate jumps, with the error bars giving the standard deviation. Data points a-e correspond to the pillars shown in Figure 3.2.

## 3.4 Discussion

Based on the before mentioned observations, several microstructure-related factors appear to influence the strength. The results indicate a common trend of decreasing strength with the presence of thicker layers. Zhou et al. [70] observed similar reductions in strength for Ag/W multilayers where hardness decreased as the modulation ratio[2] of the harder W phase increased. This is not surprising regarding the well-known dependency of multilayer strength on layer thickness. Secondly, softening also seems to be related to the position of the layers along the pillar axis. Layers located more towards the top of the pillar seem to cause more softening.[3]. In the presented study only thicker layers of the harder phase (Nb) were present. Since plastic deformation in multilayers is predominantly accommodated by the softer layers, it would not be surprising that multilayer strength reacts even stronger to variations in the softer (Cu) layers than the harder (Nb) layers.

The microstructural factors influencing the strength have been studied at a given layer thickness. Important to realize is that this effect may magnify or diminish at different layer thicknesses. Regarding the known strength relations for the confined layer slip (CLS) and Hall-Petch regime, softening due to the presence of thicker layers is expected to have its maximum within the CLS regime ($\sigma \propto ln(h/b)/h$) where the coupling between strength and layer thickness is strongest. As the layer thickness approaches the Hall-Petch regime ($\sigma \propto h^{-1/2}$) the softening effect is expected to decrease. Close to the peak strength ($\sigma \neq f(h)$) [2] layer thickness variations on the order of a few percent[4] are not expected to influence the

[2] Relative layer thickness fraction of one phase in a bi-layer, given by the layer thickness of that phase over the modulation period.
[3] Taper-induced localization of deformation causes a stress and strain gradient down the pillar axis. Thicker layers located in the highly stressed top section are expected to cause more softening than layers located in the lower stressed bottom section of the pillar.
[4] Studies by Los Alamos showed layer thickness variance of 1-8% of the average layer thickness for ARB Cu/Nb within a layer thickness regime of 10-86 nm, with variance increasing with layer thickness. [9]

strength.

Taper has shown to significantly overestimate yield strength when calculated by the conventional method using the top cross-sectional area for stress-conversion. This is not surprising considering the larger nominal cross-sectional area. The three ”alternative” methods discussed calculate stresses based on average cross-sectional area, average stress and average radius. All methods resulted in similar yield strengths, with the ”average cross-sectional area” method providing the highest correction. This shows that the higher yield strength obtained from tapered pillars can be corrected for to within a reasonable margin ($\Delta\sigma_y < 0.04\,GPa/^o taper$). Important to realize is that, although these methods are suitable for taper-correcting the average stresses and therefore the yield strength, it does not correct for the different shape of the curve. E-modulus will inevitably be higher and will need to be corrected for separately. Furthermore apparent strain-hardening will still be present, which can only be corrected for when taking into account the increasing cross-sectional area as a function of strain.

Strain-rate sensitivity was found to be independent of microstructure and taper. Independent of the phase controlling plastic deformation of the multilayer, small variations on the order of a few percent of the layer thickness have shown not to affect the rate-controlling deformation mechanisms. Furthermore the insensitivity of the SRS to taper is explained by the relation between stress and strain-rate at a given geometry (taper). Given that the geometry does not change at the moment of strain-rate change, the flow stresses is only dependent on the change in applied strain-rate.

## 3.5 Conclusion

This study has shown that microstructural variations significantly influence pillar strength. For the studied pillars, it was found that the reduction in strength due to the presence of thicker layers was of the same order as the increase in strength due to taper. This showed that microstructure and taper play an equally important role in pillar strength, and emphasizes the need to study the microstructure (e.g. SEM images) of each individual pillar before compression.

The yield strength was found to increase significantly with taper when determined according to the conventional method (top cross-sectional area). The results have shown that several methods are suitable to geometrically reduce stresses and yield strength, however none of these methods are capable of completely correcting for taper. Considering the additional effects of taper on E-modulus and strain-hardening, pillars with maximum taper of $\pm 1^o$ are recommended for determining mechanical properties.

The strain-rate sensitivity was found to be independent of the taper angle and was found to have a value of 0.007 for strain rates ranging from $10^{-4}\,s^{-1}$ to $10^{-2}\,s^{-1}$. While the presence of a few isolated thick layers was found to have a strong effect on the apparent yield stress, its effect on the SRS was found to be small. Tapered pillars can therefore be used to determine strain-rate sensitivities under conditions where higher geometrical stability is desired.

# Chapter 4

# Nanomechanical testing at room-temperature

This chapter presents the results of the nanoindentation and micropillar compression experiments performed on ARB Cu/Nb metallic multilayers at room-temperature. Four samples with distinct individual layer thickness in the range of 7-63 nm were tested. Constant strain-rate and strain-rate jump experiments were performed to obtain yield strength, strain-rate sensitivity and activation volumes as a function of layer thickness. The deformed micropillars were studied under the SEM/TEM to characterize the type of deformation at each layer thickness. Based on the mechanical test results and SEM observations different deformation regimes are distinguished and potential mechanisms of deformation are presented. Finally a deformation mechanism map is proposed for ARB Cu/Nb multilayers as a function of layer thickness.

## 4.1 Experimental

The room-temperature nanoindentation and micropillar compression experiments were performed with the Hysitron TI950 TriboIndenter. Each sample was located on an aluminium SEM holder, which was placed in a custom aluminium adapter and held in-place by three clamps. The samples were placed inside the testing chamber 30 minutes before testing for the temperature in the chamber to stabilize. Thermal drift measurements were performed before each compression/indentation by a 45-second contact hold between indenter and sample surface, and drift corrections were automatically applied by the Hysitron software. All experiments were performed with the high-load transducer operated in displacement-control. Measured drift was below 0.1 nm/s. The nanoindentation and compression experiments were performed on the same samples.

Nanoindentation was performed with a Berkovich diamond indenter and tip calibration was performed in Fused Silica in order to estimate the contact area as a function of indentation depth. Load-unload experiments were carried out to evaluate the hardness and E-modulus with indentation depth. Machine compliance was adjusted such that a near-constant E-modulus with indentation depth was obtained. A total of 10 indentations were performed per layer thickness sample. All indentations were strain-rate jump tests within the $10^{-2} - 10^{-3}\, s^{-1}$ strain-rate regime. Indentation depth was $3\,\mu m$.

Micropillar compression was performed with a diamond flat-punch indenter with diameter of $10\,\mu m$. Constant strain-rate and strain-rate jump tests were performed on both taper-free and tapered pillars. Yield strength was only determined from taper-free pillars ($\pm\, 1^o$ taper), strain-rate sensitivities were determined from both taper-free and tapered pillars[1]. All compressions were performed perpendicular to the

[1] The study presented in Chapter 3 on the effect of taper on material parameters determined from micropillar compression showed that whereas yield strength and strain-hardening are dependent on pillar taper, SRS is independent of taper.

layers at pillar strains of $0.1 - 0.2$. The initial loading strain-rate is $10^{-3}\,s^{-1}$. Table 4.1 gives an overview of the number of compressions performed for each sample and the average pillar dimensions of the taper-free pillars.

Table 4.1: Overview of the number of compressions performed on taper-free and tapered pillars per layer thickness sample and the average pillar dimensions of the taper-free pillars.

| Layer thickness | Compressions (taper-free/tapered) | Diameter ($\mu m$) | Height ($\mu m$) | Taper ($deg$) |
|---|---|---|---|---|
| 7 nm | 10/3 | 4.7±0.1 | 13.4±0.4 | 1.0±0.2 |
| 16 nm | 12/2 | 4.8±0.1 | 13.4±0.3 | 1.2±0.3 |
| 34 nm | 6/3 | 4.9±0.1 | 14.0±0.4 | 0.4±0.0 |
| 63 nm | 6/8 | 5.0±0.0 | 13.9±0.4 | 0.8±0.2 |

## 4.2 Results

### 4.2.1 Nanoindentation

Due to the relative ease of performing nanoindentation, all samples were additionally tested by nanoindentation in order to compare results with micropillar compression. Representative force-displacement curves of the nanoindentation strain-rate jump experiments are presented in Figure 4.1a, instantaneous hardness curves are presented in Figure 4.1b. The curves of the 7 and 16 nm samples were nearly identical, indicating similar hardness. The 34 nm curves were slightly lower, indicating a small decrease in hardness compared to the samples with the finest layer thicknesses. The curves of the 63 nm sample appeared to show a more significant decrease in hardness. The change in instantaneous hardness due to the stepped strain-rate seemed to be similar for all layer thicknesses, which could indicate similar strain-rate sensitivities.

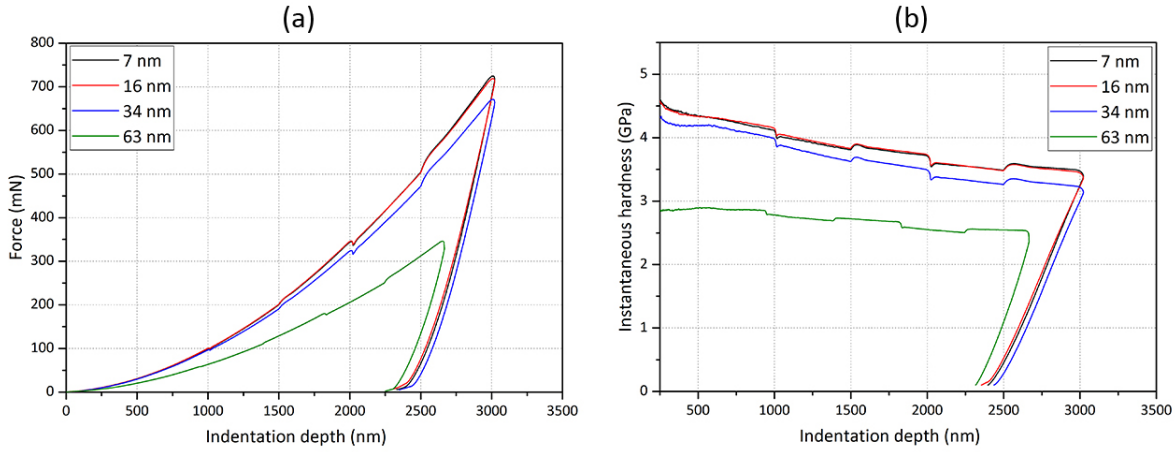


Figure 4.1: Representative nanoindentation compression curves (a) and instantaneous hardness curves (b) after conversion.

### 4.2.2 Micropillar compression

All pillars were analyzed under the SEM after compression to characterize deformation. SEM images of representative pillar deformation at each studied layer thickness are presented in Figure 4.3. Significantly different deformation behaviour was observed at different layer thicknesses. At 63 nm relatively homogeneous deformation was observed. Layers appeared to co-deform and no shear failure was observed. At the finest thicknesses the pillars were observed to fail by shear at relatively small plastic strains. Shear failure was observed to occur along one or several shear planes. The shear planes were oriented at $32 - 38^o$ and shearing appeared to occur towards the rolling direction of the multilayer. In the 34 nm pillars homogeneous deformation was observed up to strains of 0.1. However at larger strains of 0.15 a change in behaviour was observed. At these strains a shear band appeared to be present as indicated by the arrow.

Representative compression curves obtained for ARB Cu/Nb at different layer thickness are presented in Figure 4.2. The scatter is attributed to microstructural variations between pillars which is characteristic of multilayers fabricated by accumulative roll-bonding. The curves indicate a clear decrease in strength with layer thickness. The 7 and 16 nm samples show the highest strengths with flow stresses surpassing 2 GPa. At 34 and 63 nm the flow stresses drop to approximately 1.7 GPa and 1.3 GPa. Comparing the curves with the SEM images, one can see that shear failure appears to be linked to very high flow stresses. Low flow stresses appear to be linked to more homogeneous deformation, as observed in the 63 nm pillars.

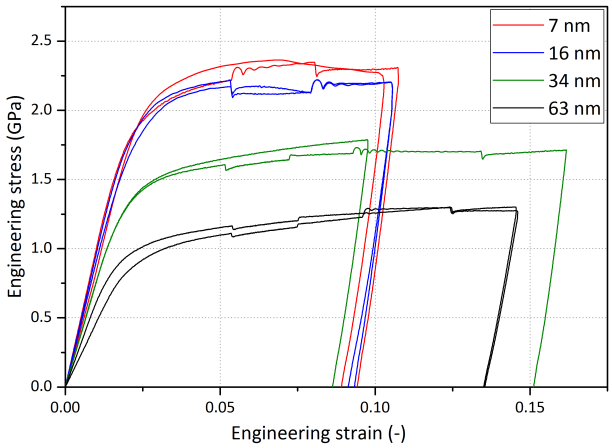


Figure 4.2: Representative (taper-free) compression curves of ARB Cu/Nb micropillars with average layer thickness of 7, 16, 34 and 63 nm.

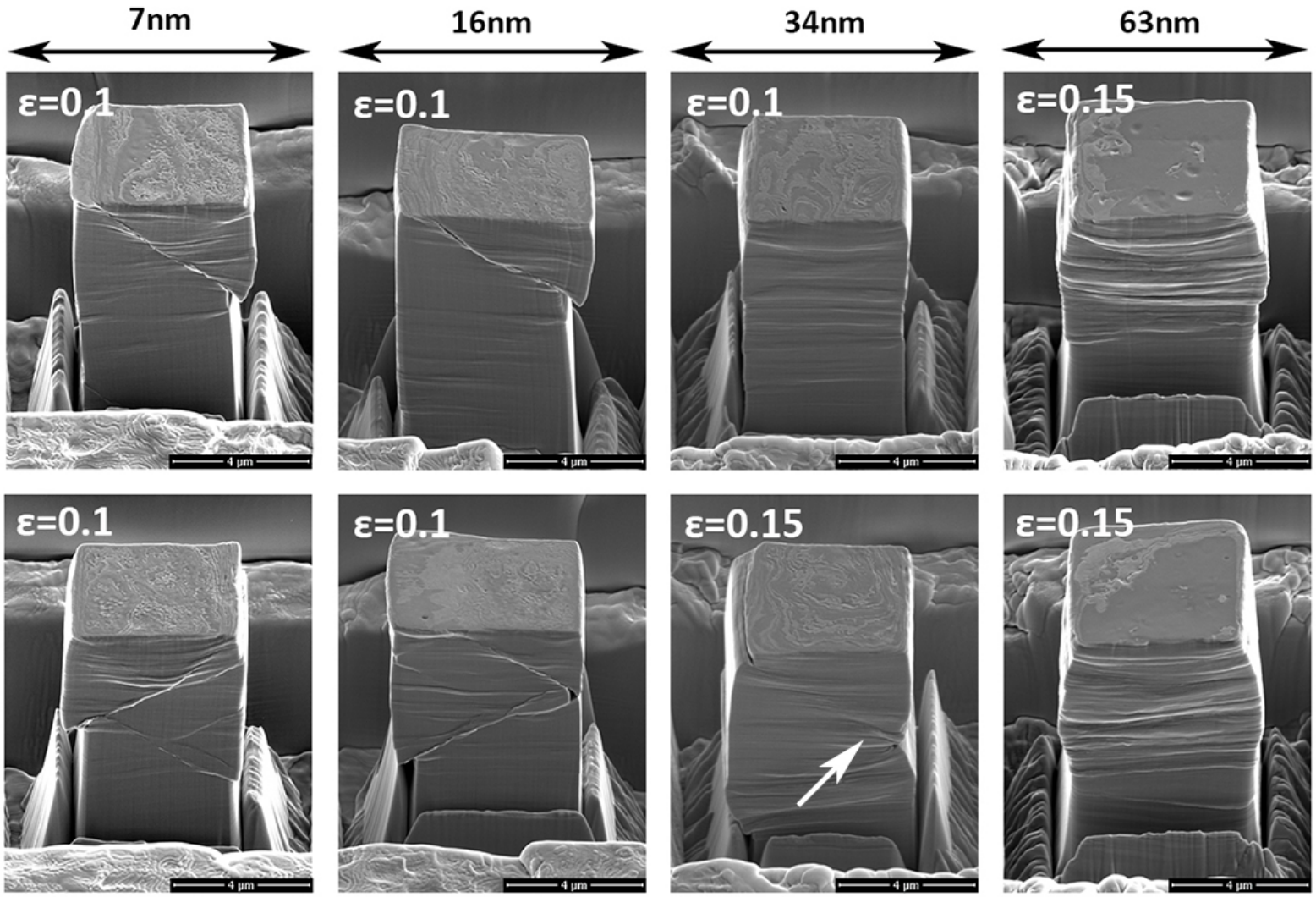


Figure 4.3: SEM images of deformed micropillars with individual layer thickness of 7, 16, 34 and 63 nm. The arrow indicates the presence of what appears to be a shear band.

## 4.3 Discussion

### 4.3.1 Indentation hardness vs. layer thickness

The obtained hardness as a function of the layer thickness is presented in Figure 4.4, the values are summarized in Table 4.2. Similar hardness values of $\pm 4.25\,GPa$ were obtained for the 7 and 16 nm samples. As the layer thickness increased to 34 nm a small drop in hardness was observed. A more significant drop was observed as the layer thickness further increased to 63 nm. The obtained yield strength values corresponded well with hardness values reported by Monclús et al. [26]. Furthermore Monclús et al. reported a nanoindentation hardness peak of 5 GPa for ARB Cu/Nb at layer thickness of 10 nm. The layer thickness at which peak strength was observed corresponds well with the current results. The current peak hardness is approximately 0.7 GPa lower.

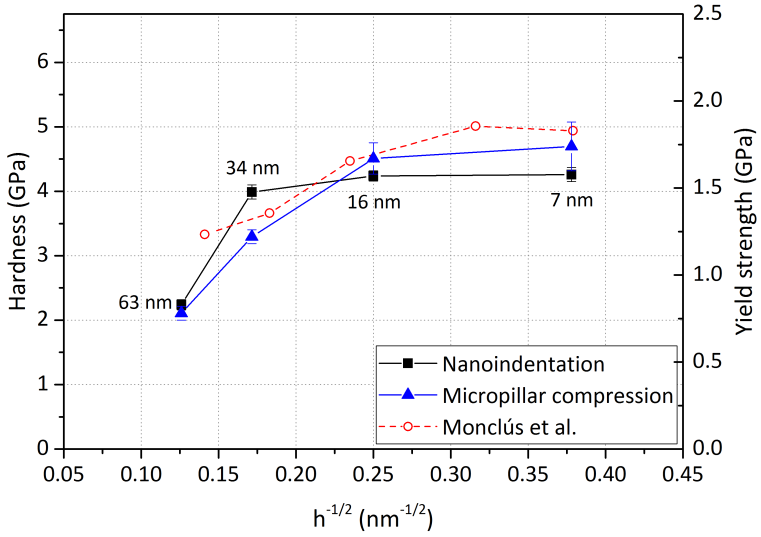


Figure 4.4: Multilayer hardness as a function of layer thickness obtained from nanoindentation. Micropillar compression results presented in Section 4.3.3 are plotted as a reference. Hardness and yield strength are related by a constraint factor of 2.7.

Table 4.2: Overview of nanoindentation hardness values for ARB Cu/Nb obtained at different layer thicknesses.

| Layer thickness | Hardness (GPa) |
|---|---|
| 7 nm | 4.26 ± 0.11 |
| 16 nm | 4.24 ± 0.08 |
| 34 nm | 3.99 ± 0.11 |
| 63 nm | 2.24 ± 0.08 |

Comparing nanoindentation results to the micropillar compression results presented in Section 4.3.3, one can see that nanoindentation hardness corresponds reasonably well to micropillar yield strength for a constraint factor of 2.7. However the constraint factor is known to relate hardness to stresses at 7-8%

plastic strain. Considering that yield is obtained at 0.2% plastic strain, H/2.7 is more representative of plastic flow stresses. The fact that the current nanoindentation flow stresses are lower than the compression yield strength indicate a Tabor factor $< 2.7$. The differences in strengh obtained from nanoindentation and micropillar compression are attributed to the different nature of testing of these techniques. This is further addressed in Section 4.3.4.

### 4.3.2 Deformation behaviour

A clear difference in deformation behaviour was observed at the largest thickness and the finest thicknesses. At the largest thicknesses pillars deformed relatively homogeneous and at the finest thicknesses the pillars failed by shear. Shear failure is a plastic instability and is a known problem for materials with low strain-hardening capability [13, 71]. Strain-hardening in metallic multilayers is generally believed to decrease at finer thicknesses[2], as shown by Zhang et al. in Cu/Zr multilayers [29, 32]. Multilayered materials therefore tend to be more prone to plastic instabilities at finer thicknesses, which is in-line with the current observations.

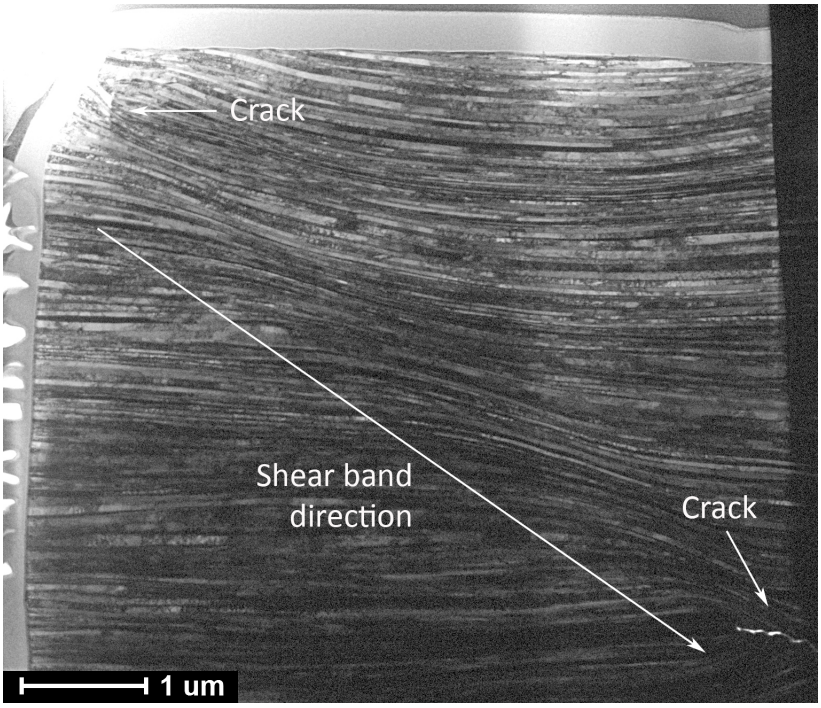


Figure 4.5: Dark-field TEM image of 34 nm ARB Cu/Nb showing a shear band across the sample. Layers were continuous across the shear band and two cracks were observed at each end of the shear band, one of which is clearly visible (bottom-right).

When comparing the deformation behaviour of the pillars at different layer thicknesses, one can see that a transition appears to occur at a layer thickness of 34 nm. The 34 nm pillar compressed to 10% strain appeared to show homogeneous deformation. At 15% strain signs of shear banding were present on the pillar surface. TEM analysis confirmed the presence of a shear band as shown in Figure 4.5, with the shear angle corresponding to the range of angles observed in the 7 and 16 nm pillars. The layered structure was maintained across the shear band. However, crack formation was observed at both ends of the shear band. This behaviour is very similar to the deformation observed in the 7 and 16 nm pillars.

[2]Similar to reduced strain-hardening in conventional metals as the grain size is reduced to the nanocrystallne range.

More interestingly, based on the corresponding compression curve the onset of failure was estimated to occur at a stress of $\pm 1.7\,GPa$. As shown in Figure 4.4, this stress is the same as the yield strength of the 7 and 16 nm pillars. It therefore appears that in the 7 and 16 nm samples strain-localization followed by shear failure occurs very quickly after yielding. In the 34 nm sample flow stresses of 1.7 GPa are only attained at higher strains and explain the delay of shear failure. At higher layer thicknesses where flow stresses do not reach a stress level of 1.7 GPa shear failure is not expected to occur.

Furthermore it was mentioned that there appeared to be a relation between the shearing direction of the pillars and the rolling direction during ARB manufacturing. Although the exact shearing direction was not further investigated, the textures in ARB manufactured Cu/Nb are known to differ along the rolling direction and transverse direction. The fact that pillars sheared in the rolling direction could indicate the existence of a preferred shearing direction possibly related to the directional texture of the interface.

### 4.3.3 Yield stress vs. layer thickness

The yield strengths as a function of layer thickness obtained from the compression experiments are plotted in Figure 4.6. The values are summarized in Table 4.3. Several data on pure Cu and Nb have been added to the figure. Meyers et al. collected empirical data on the yield stress of Cu as a function of grain size [13], as indicated by the red data points and red solid line. They reported a deviation from the Hall-Petch behaviour as grain size reached the nanocrystalline range, with strength approaching a plateau at the finest grain sizes. Furthermore Cu/Nb multilayers are known to form deformation twins in the Cu layers for h<50-60 nm [9, 48]. The strength in nanotwinned materials is known to be governed by the twin spacing as opposed to the grain size. Choi et al. reported nanoindentation hardness of 2.44 GPa for Cu with grain size of $0.5 - 3\mu m$ and twin spacing between 40 and 80 nm. Lu et al. studied the tensile yield strength as a function of twin spacing for Cu with grain size of 400-600 nm. They reported a maximum tensile yield strength of 0.9 GPa for a twin spacing of 15 nm. Few data were available on the strength of Nb. Pan et al. performed quasi-static compression experiments ($\dot{\epsilon} = 10^{-3}\,s^{-1}$) on ufg-Nb with grain size of 510 nm and obtained flow stresses of 540 MPa [15]. Based on the reported compression curves the yield strength is estimated at 450 MPa. No data was available on nanocrystalline Nb.

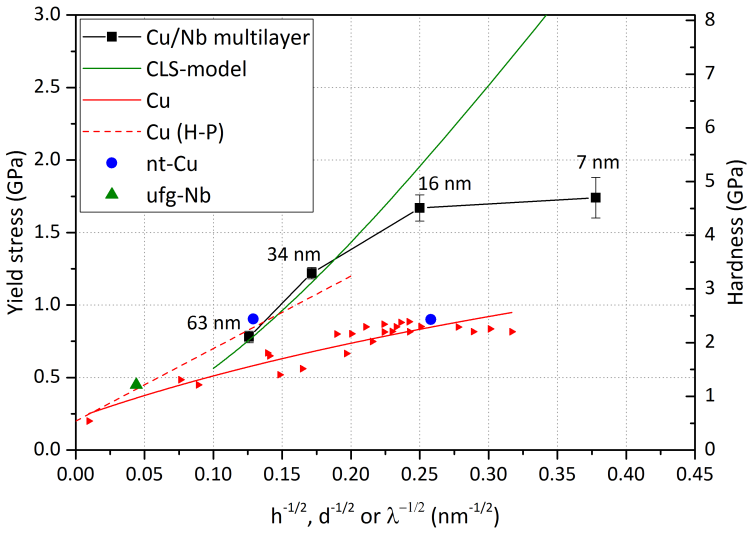


Figure 4.6: Plot of yield strength versus layer thickness for ARB Cu/Nb. Plot includes strength predicted by the confined layer slip model (CLS-model), classical Hall-Petch relation and empirical strength for Cu [13], nanotwinned (nt) Cu [14] and ultra-fine grained (ufg) Nb [15]. Yield strength and hardness are related by a constraint factor of 2.7. Horizontal axis represents either layer thickness ($h$), grain size ($d$) or twin size ($\lambda$) in case of nanotwinned Cu.

Table 4.3: Yield strength and maximum flow stresses for ARB Cu/Nb with different layer thicknesses.

| Layer thickness | Yield strength (GPa) | Eng. flow stress (GPa) | True flow stress (GPa) |
|---|---|---|---|
| 7 nm | 1.74±0.14 | 2.28±0.19 | 2.13±0.13 |
| 16 nm | 1.67±0.09 | 2.28±0.07 | 2.12±0.07 |
| 34 nm | 1.22±0.04 | - | 1.60±0.03 |
| 63 nm | 0.78±0.04 | - | 1.16±0.04 |

The yield strength was found to increase with layer thickness. At a layer thickness of 63 nm a yield strength of 0.78 GPa was obtained. At 16 nm thickness the yield strength increased to 1.67 GPa. At finer thicknesses the strength started to level off. A peak strength of 1.74 GPa was obtained at a layer thickness of 7 nm. Comparing multilayer strength with that of pure Cu, one can see that for a layer thickness of 63 nm the strength approaches that of nanotwinned Cu when the twin size equals the layer thickness. Twinning within Cu layers has been observed in ARB Cu/Nb multilayers for h$<$60 nm, and could explain the higher strength of the 63 nm multilayer compared to conventional nanocrystalline Cu. At finer thicknesses multilayer strength is significantly higher. At peak strength the multilayer approaches strengths twice the strength of conventional nanocrystalline Cu. It is known that the twinning fraction can approach 30% at the finest thicknesses [48]. However how twinning influences multilayer strength at the finest thicknesses is unknown since the twin spacing is not mentioned.

How multilayer strength compares to the strength of nanocrystalline Nb is unknown. If the strengthening behaviour is similar to that of bcc-Fe as reported by Meyers et al. [13], Nb is still expected to be stronger than Cu within the nanocrystalline regime. Regarding the strength of the multilayer in relation to its constituents, multilayer strength appears to be governed by several factors. If Nb still exhibits a higher strength than Cu at grain sizes of a few nanometer and multilayer strength is between that of Cu and Nb, then the strength seems to approach that of the rules-of-mixture. On the other hand if multilayer strength is higher than that of both Cu and Nb, it would indicate that incoherent interfaces in multilayers provide more strengthening than grain boundaries in conventional metals. Furthermore nanotwinning is also likely to play a role. Although no quantitative conclusions can be drawn on what exactly governs the strength in ARB Cu/Nb, the results suggest that it is a combination of the rules-of-mixture, interfaces and nanotwinning.

### Deformation models

In order to get an impression of the different deformation mechanisms operating within the current layer thickness regime, multilayer strengthening is compared with the known strength-relations of the different deformation regimes. Metallic multilayers are known to exhibit different deformation regimes as shown in Figure 4.7. Although unknown for ARB Cu/Nb, for PVD Cu/Nb it is known that for h$>$50-75 nm Hall-Petch type behaviour is observed [2, 43]. For these layer thicknesses the layers are thick enough for dislocation pile-ups to form. The Hall-Petch strengthening relation is given by [2]

$$\sigma_y = \sigma_0 + kh^{-1/2} \tag{4.1}$$

with $\sigma_y$ the yield stress, $h$ the layer thickness, $k$ the Hall-Petch slope and $\sigma_0$ a measure of the lattice friction stress to slip. Misra et al. showed typical Hall-Petch slopes of $k = 5.1 - 6.7\,GPa\sqrt{nm}$ for PVD Cu/Nb similar to that of pure Cu, and $\sigma_0 = 600 - 800\,MPa$ [43]. For ARB Cu/Nb these values have

not been reported. The strengthening capability of ARB Cu/Nb reflected by $k$ is expected to be of the same order as that of PVD Cu/Nb. However, $\sigma_0$ is expected to be lower for ARB Cu/Nb due to the lower strength generally observed in Cu/Nb multilayers with (weaker) ARB interfaces, i.e. $\sigma_0$ <600 MPa.

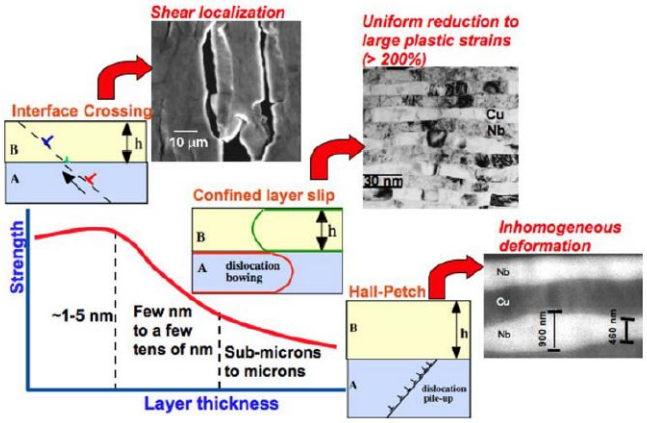


Figure 4.7: Overview of different deformation regimes observed in metallic multilayers as a function of layer thickness. [16]

At h<50-75 nm the layers are too thin for dislocation pile-ups to occur [2,43]. Instead deformation occurs by single dislocation loops bowing out between the interfaces bordering the layer. A schematic overview of confined layer slip is given in Figure 4.8. Important to note is that dislocation bowing is dependent on interface strength, with strong interfaces exhibiting higher repelling forces and therefore more bowing. Furthermore as dislocations travel from one interface to the other, dislocations are deposited at the interface which can interact with other dislocation loops. Based on these observations Misra et al. developed a model predicting multilayer strength within the confined layer slip regime [2].

$$\sigma_{cls} = M\frac{\mu b}{8\pi h'}\left(\frac{4-\nu}{1-\nu}\right)\left[ln\frac{\alpha h'}{b}\right] - \frac{f}{h} + \frac{C}{\lambda} \tag{4.2}$$

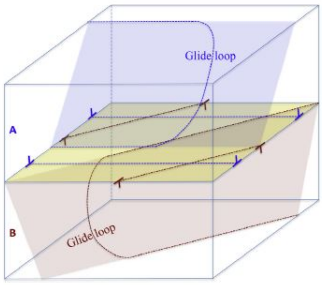


Figure 4.8: Schematic of the confined layer slip mechanism in multilayered materials. The interfaces bow-out dislocations resulting in dislocation glide loops confined to the layers. During the process dislocations are deposited at the interfaces which interact with subsequent glide loops. [3]

The first term on the right-hand side represents the normal in-plane stress $\sigma_{cls}$ needed to propagate a dislocation along the glide plane. $M$ is the Taylor factor, $\mu$ the shear modulus, $b$ the Burgers vector, $\nu$ the Poisson's ratio, $\alpha$ the core cut-off parameter, a measure of the interface strength to dislocation transmission, and $h' = h/sin\phi$ is the thickness of the layer parallel to the glide plane. The second term represents the interface stress contribution with $f$ the characteristic interface stress and $h$ the layer thickness. At large layer thicknesses this term is small. However at small layer thicknesses the interface

stress contribution may be significant. The third term represents the resistive force from the deposited interface dislocations. $C$ is the stress field of a single array of edge dislocations of spacing $\lambda$ given by $C = \mu b/(1-\nu)$ and $\lambda$ is related to the applied strain $\epsilon$ by $\lambda = b/\epsilon$.

At the finest thicknesses the stresses to bow-out dislocations are so high that interface crossing becomes favourable. In this regime decoupling between strength and layer thickness occurs and a strength plateau is observed $\sigma \neq h$. For PVD Cu/Nb this occurs at layer thicknesses of a few nanometers [2, 45]. For ARB Cu/Nb this transition occurs at larger thickness of $\approx 10\,nm$ [26].

In Figure 4.6 the strength predicted by the CLS model is plotted using the following parameter values: Taylor factor $M = 3.1$, shear modulus $\mu = 48\,GPa$ (Cu), Burgers vector $b = 0.25\,nm$ (Cu), Poisson's ratio $\nu = 0.3$, characteristic interface stress $f = 2\,J/m^2$ and $h' = h/sin\phi$ with $\phi = 70.8^o$ [2]. The misfit dislocation spacing $\lambda$ was determined at $\epsilon = 0.2\%$, the plastic strain at which the yield strength is determined. The core cutt-off parameter $\alpha$ which is in the range of $0-1$ was used as a fitting-parameter. The Hall-Petch behaviour of Cu is assumed to be representative of Hall-Petch type strengthening of the multilayer based on [43].

Comparing the strengthening in the multilayer with the strength-relations explained before, the Hall-Petch slope of Cu ($k \pm 5\,GPa\sqrt{nm}$) underestimates multilayer strengthening. Although not plotted in the graph, the upper bound estimate ($k = 6.7GPa\sqrt{nm}$) also underestimates strengthening. The CLS-model on the other hand corresponds well with layer thicknesses between 34 and 63 nm and for $\alpha = 1$. The relatively high value of $\alpha$ implies a compact dislocation core, which is generally associated with interfaces that permit dislocation transmission more easily, e.g. ARB interfaces [2]. Compared to PVD interfaces with wide dislocation core and $\alpha = 0.2$, the higher $\alpha$ value for ARB interfaces can be physically justified. As the layer thickness decreases from 34 nm to 16 nm the CLS-model breaks down and overestimates the yield stress. The strength plateau at the finest layer thicknesses is indicative of the onset of a different deformation mechanism where strength is no longer dependent on layer thickness ($\sigma \neq h$).

The trends in multilayer strength indicate Hall-Petch behaviour to occur at $h > 63\,nm$. For layer thicknesses of 63 nm to 34 nm the results suggest deformation to be controlled by confined layer slip. At finer thicknesses a transition is expected to a different deformation mechanism. These results are compatible with the deformation behaviour observed in the micropillars. The relatively homogeneous deformation observed in the 63 nm pillars fits the confined layer slip mechanism well. The deviation predicted by the CLS model at a layer thickness of 34 nm was also observed in the 34 nm pillars, where a transition from homogeneous deformation to shear-like deformation was observed at flow stresses of 1.7 GPa. Furthermore the strength plateau suggests similar deformation at layer thicknesses of 7 and 16 nm, which was also observed in the SEM images. Whether deformation at the finest thicknesses was characterized by transmission of dislocations across interfaces was not confirmed.

### 4.3.4 Strain-rate sensitivity and activation volume vs. layer thickness

Strain-rate sensitivities and activation volumes obtained by micropillar compression are plotted in Figure 4.9. The values are summarized in Table 4.4. For the data obtained by micropillar compression distinction is made between the $10^{-4} - 10^{-3}\,s^{-1}$ and $10^{-3} - 10^{-2}\,s^{-1}$ strain-rate regimes. Furthermore due to shear occurring rapidly after yielding in the 7 and 16 nm pillars, few "good" jumps were obtained limiting the statistical data for these samples. Strain-rate sensitivities and activation volumes reported for pure Cu and Nb were also plotted. Wei et al. reported a curve of SRS vs. grain size for Cu based on tensile rate-jump tests and other empirical SRS values reported in literature [17]. Pan et al. reported strain-rate sensitivities of 0.012 for ufg-Nb with grain sizes of 275-510 nm [15]. No data was found on nanocrystalline Nb.

Comparing the SRS of the multilayer to that of pure Cu, one can see that the SRS is significantly lower than Cu when the grain size is on the order of the layer thickness. This is explained by the fact that

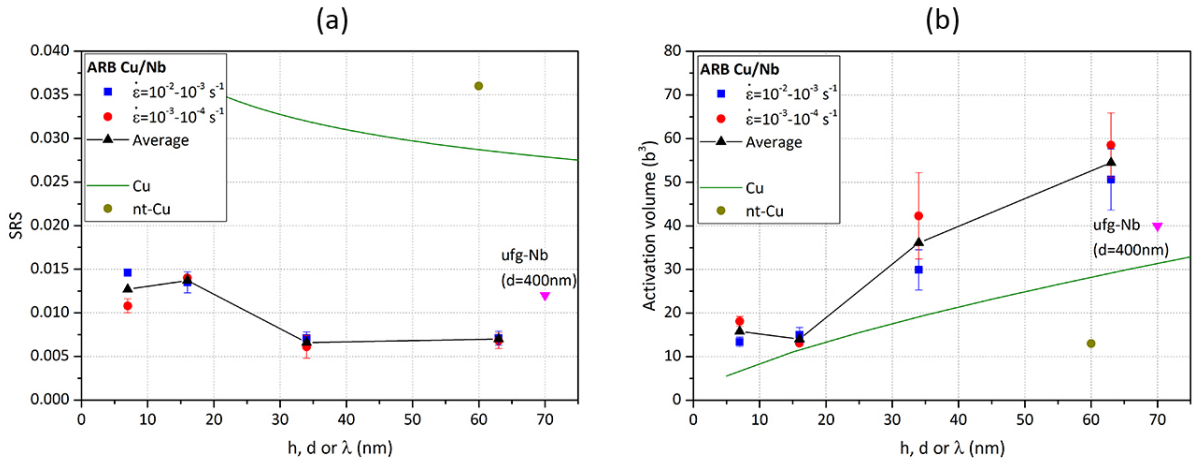


Figure 4.9: Plot showing strain-rate sensitivities (a) and activation volumes (b) obtained from micropillar compression as a function of layer thickness. SRS of Cu based on [13, 17] and activation volume based on [18], nt-Cu data from [14] and ufg-Nb from [15].

Table 4.4: Strain-rate sensitivites and activation volumes obtained from compression for ARB Cu/Nb within strain-rate regime of $10^{-2} - 10^{-4}\, s^{-1}$.

| **Layer thickness** | **SRS** $\dot{\epsilon} = 10^{-2} - 10^{-3}\, s^{-1}$ | **SRS** $\dot{\epsilon} = 10^{-3} - 10^{-4}\, s^{-1}$ | **AV** ($b^3$) $\dot{\epsilon} = 10^{-2} - 10^{-3}\, s^{-1}$ | **AV** ($b^3$) $\dot{\epsilon} = 10^{-3} - 10^{-4}\, s^{-1}$ |
|---|---|---|---|---|
| 7nm | 0.015±0.000 | 0.011±0.001 | 13.4±1.1 | 18.1±1.1 |
| 16nm | 0.014±0.001 | 0.014±— | 15.0±1.7 | 13.1±— |
| 34nm | 0.007±0.001 | 0.006±0.001 | 29.9±4.6 | 42.3±9.9 |
| 63nm | 0.007±0.001 | 0.007±0.001 | 50.6±7.0 | 58.5±7.4 |

for FCC metals with nanocrystalline grains, grain boundary sliding ($m = 0.5$) is a likely scenario as $d < 20\, nm$ [68]. In ARB Cu/Nb grain boundary and/or interface sliding is extremely difficult. Regarding the orientation of the layers with respect to the applied force and the high strength of the interfaces, sliding can only occur parallel to the interfaces. Furthermore the faceted nature of ARB interfaces require relatively large stresses for interfacial sliding to occur. Interface and/or grain boundary sliding is therefore not a likely scenario for the multilayered system.

Knowing that BCC metals generally show a decreasing strain-rate sensitivity with decreasing grain size, the SRS of Nb is expected to be below 0.012 for the nanocrystalline regime. The opposite trend of the SRS in BCC metals compared to FCC metals is related to the lattice friction. As grain size decreases and flow stresses increase, thermally activated cross-slip of edge and screw dislocations become easier lowering the activation energy and strain-rate sensitivity. The increase in strain-rate sensitivity with decreasing layer thickness observed in the multilayer follows more the trend of Cu.

Apart from the SRS of the multilayer in relation to pure Cu and Nb, the increase in strain-rate sensitivity as the layer thickness is reduced from 34 nm to 16 nm suggests the presence of two deformation regimes within the current layer thickness regime. Comparing this with the obtained activation volumes, a similar trend is observed. For the 34 and 63 nm samples activation volumes of $36\, b^3$ and $55\, b^3$ were obtained.

These activation volumes are compatible with confined layer slip ($V = 10 - 100\,b^3$) [13, 23]. At layer thicknesses of 7 and 16 nm activation volumes of $\pm 15\,b^3$ were obtained. This value approaches the regime compatible with dislocation nucleation and emission at interfaces ($V = 1 - 10\,b^3$) [13, 23].

Considering that the twin fraction approaches 30% at the finest thicknesses [9] and that twinning occurs by the emission of partial dislocations from interfaces [47], dislocation nucleation/emission from interfaces seems compatible with the mechanisms of twin-formation in the 7 and 16 nm samples. For the 34 and 63 nm samples a different deformation mechanism is predicted based on $m$ and $V$. Confined layer slip predicted by $V$ for the 63 nm sample is in-line with predictions from multilayer strength and SEM observations in pillar deformation. For the 34 nm sample confined layer slip is also predicted based on $V$, however the SEM images revealed shear-like deformation at larger strains. Since most of the deformation occurred below the threshold stress of 1.7 GPa, the obtained $m$ and $V$ are believed to be more representative of homogeneous deformation. This explains why the values are similar to that of the 63 nm sample. Altogether, the trends in strain-rate sensitivity and activation volumes correspond well to trends in multilayer strength and observations in deformation behaviour.

**Micropillar compression vs. nanoindentation**

In Figure 4.10 the SRS and activation volumes obtained from nanoindentation and micropillar compression are compared. For all layer thicknesses an average nanoindentation strain-rate sensitivity of 0.012 was obtained and activation volumes of $28 - 40\,b^3$. As opposed to micropillar compression, the constant SRS and $10\,b^3 << V << 100\,b^3$ obtained for nanoindentation indicate similar deformation behaviour over the full thickness range. Wheeler et al. reported similar behaviour for ufg-Al with temperature [72]. The strain-rate sensitivities and activation volumes obtained from nanoindentation were found to be less sensitive to temperature than values obtained by compression. They attributed this to the high plastic strain imposed by the indenter, which activates all thermodynamically-available deformation mechanisms.

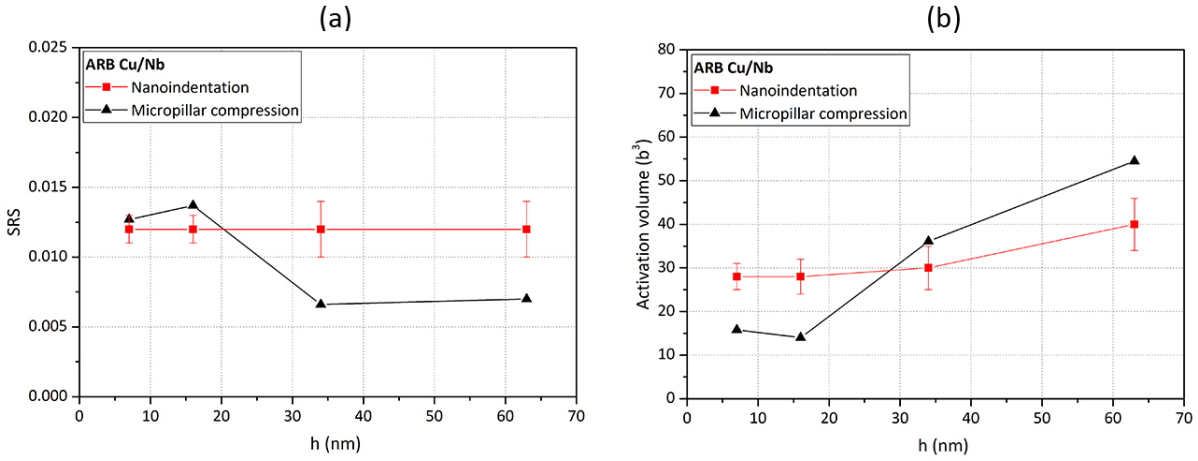


Figure 4.10: Comparison of strain-rate sensitivities (a) and activation volumes (b) obtained from micropillar compression and nanoindentation.

As indicated in Figure 4.11, in nanoindentation the compressed material is represented by a sphere. As opposed to the reasonably uni-axial stress-state in micropillar compression, in nanoindentation the material is compressed in multiple directions which results in non-homogeneous stress-strain states inside the material. Furthermore in the micropillar compression results the pillars were compressed perpendicular to the layers. One can see that in nanoindentation the material is compressed both perpendicular and parallel to layers, thereby giving an average over all layer directions.

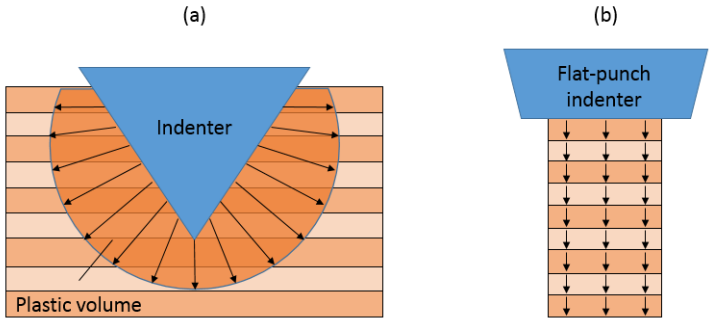


Figure 4.11: Schematic representation of deformation during nanoindentation (a) and micropillar compression (b). In nanoindentation plastic volume is represented by a sphere. Deformation occurs in multiple directions resulting in a complex stress-strain state. In micropillar compression, given that pillar taper is small, deformation is applied uni-axially perpendicular to the layers resulting in a homogeneous stress-strain state.

It is expected that in nanoindentation the high strains together with the different directions of compression activates multiple deformation mechanisms. These mechanisms are expected to be activated at all thicknesses studied. As a result it is extremely difficult to isolate single dislocation mechanisms. In micropillar compression the uni-axial stress state appears to activate fewer deformation mechanisms, leading to distinct strain-rate sensitivities at different layer thicknesses. These are expected to be representative of one or at most two deformation mechanisms. Although both techniques can be used to study the mechanical properties of a material, micropillar compression is more suitable to separate and study the fundamentals of individual deformation mechanisms.

## 4.4 Deformation mechanism map

Based on the results of the compression studies a deformation mechanism map is proposed for ARB Cu/Nb multilayers. The study has shown two distinct deformation regimes for layer thicknesses between 7 and 63 nm. The transition between these deformation regimes was observed to occur in the 34 nm sample and the flow stresses $\sigma_f$ for the transition were estimated at 1.7 GPa. For $\sigma_f < 1.7 GPa$ the results predicted confined layer slip to occur. At higher flow stresses a different mechanism was observed to control deformation leading to shear failure of the pillars. Based on the activation volumes predicting dislocation nucleation and/or transmission from/across interfaces, this regime is referred to as the ”interface-controlled deformation regime”. This threshold stress of 1.7 GPa is assumed to be independent of layer thickness based on SEM observations of the shear onset in the 7, 16 and 34 nm pillars. The transition between confined layer slip and Hall-Petch type behaviour was assumed to occur at 75 nm based on observations in PVD Cu/Nb.

Since the yield strength of the 7 and 16 nm pillars is 1.7 GPa, a direct transition from the elastic regime to the interface-controlled regime is predicted. For these thicknesses the maximum flow stresses are estimated at 2.3 GPa based on the compression curves. As the layer thickness increases and the yield strength reduces, the region characterized by $\sigma_y < \sigma_f < 1.7 GPa$ is controlled by confined layer slip. The yield strength for this regime is estimated by the CLS model as plotted in Figure 4.6 up to a layer thickness of 75 nm. The maximum flow stresses were determined assuming a 0.6 GPa offset based on the differences in yield strength and flow stresses observed in the 7 and 16 nm samples.

For h>75 nm deformation is assumed to be controlled by Hall-Petch behaviour. A yield strength of 0.68 GPa was estimated at 75 nm thickness based on extrapolation of the CLS curve. Using Equation 4.1 and taking $k = 0.16\, GPa\sqrt{nm}$ [43], this corresponds to $\sigma_0$ of $\pm$100 MPa. This seems reasonable considering a $\sigma_0$ of 600-800 MPa for PVD Cu/Nb and the strength of ARB Cu/Nb generally being a few tenths of

GPa lower. Hence the yield strength for ARB Cu/Nb and $75\,nm < h < 1000\,nm$ was determined by Equation 4.1 using $k = 0.16\,GPa\sqrt{nm}$ and $\approx= 100\,MPa$. The maximum flow stresses were determined in a similar fashion.

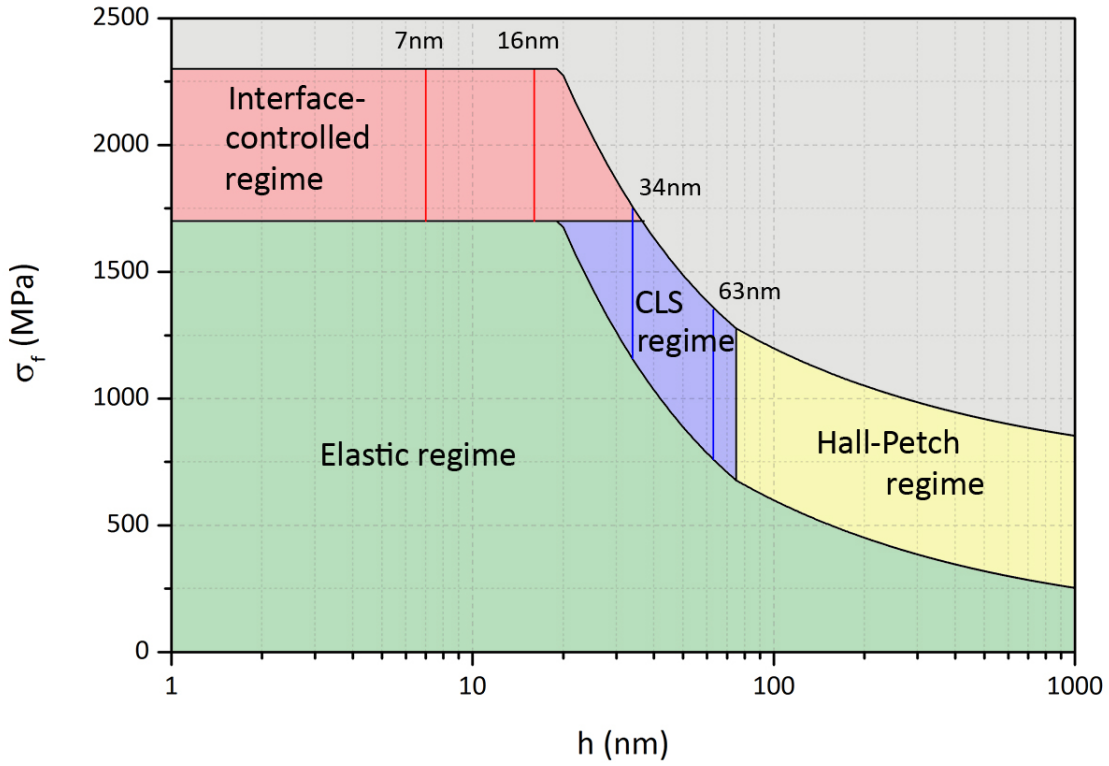


Figure 4.12: Room-temperature deformation mechanism map for ARB Cu/Nb NMMs with sub-micron layer thickness. Map is valid for a strain-rate regime of $10^{-2} - 10^{-4}\,s{-}1$.

The obtained deformation mechanism map is presented in Figure 4.12. The flow stress ranges obtained from the compression experiments at different layer thicknesses have also been plotted, and correspond well with the deformation mechanism map. Important to emphasize is that this map is valid for ARB Cu/Nb within a strain-rate regime of $10^{-2} - 10^{-4}\,s^{-1}$. Yield strength and flow stress borders will inevitably shift when the material is tested at different strain-rates. Furthermore a limitation of the current map is that strain-hardening is not taken into account. At the finest thicknesses strain-hardening is known to be very low. However, as layer thickness approaches $1\,\mu m$ maximum flow stresses are expected to be higher due to increased strain-hardening capability at these thicknesses. As a result the line between the grey region and the different plastic regimes, which represents the maximum flow stresses, is expected to shift upwards when the effect of strain-hardening is taken into account. This shift is expected to increase with increasing layer thickness due to the higher strain-hardening capability at larger layer thicknesses.

## 4.5 Conclusion

The compression experiments showed that two different deformation mechanisms are operative within the layer thickness regime studied. A transition in mechanism appears to occur as flow stresses surpass a threshold stress of 1.7 GPa. It is believed that at lower flow stresses deformation occurs by confined layer slip as indicated by the absence of strain localization and activation volumes of several tens of $b^3$.

As flow stresses surpass the threshold stress a different mechanism controls deformation which leads to strain localization followed by shear failure. With activation volumes approaching $10\,b^3$ compatible with dislocation nucleation and/or transmission from/across interfaces, it is expected that for this type of deformation flow the interfaces are rate-controlling.

Furthermore comparison of micropillar compression and nanoindentation results showed that both techniques can yield significantly different conclusions on deformation behaviour of the material. Based on strain-rate sensitivities and activation volumes, it is concluded that out of the two techniques micropillar compression is capable of separating deformation mechanisms, and is therefore more suitable for studying the fundamentals of individual deformation mechanisms.

Finally deformation of the 7 nm and 16 nm pillars showed that the shear direction is likely related to the rolling direction of the material. This indices a possible relation between preferred shearing direction and texture, which is interesting for future research.

# Chapter 5

# Micropillar compression at high-temperature

This chapter presents the results of the high-temperature compression experiments on ARB Cu/Nb multilayers. Compressions were performed at $20\,^oC$, $200\,^oC$ and $400\,^oC$. First an overview is given of the test set-up, experimental procedures and details on the compressions performed per layer thickness and temperature. SEM images of the deformed micropillars and the obtained compression curves are presented in Section 5.2. Yield strengths, strain-rate sensitivities and activation volumes will then be presented, which in combination with the SEM observations will be used to discuss the mechanical properties and deformation behaviour of the material as a function of temperature.

## 5.1 Experimental

The high-temperature compressions were performed with the Hysitron PI87 in-situ picoindenter. Figure 5.1 shows the test set-up for high-temperature testing. The sample was mounted on a special hot stage equipped with heater and thermocouple, and insulated from the rest of the system by a low thermally conductive ceramic disk and water cooling. An additional thermocouple was placed on the sample surface close to the micropillars to monitor the surface temperature close to the pillars. The transducer was equipped with a special high-temperature probe and a diamond flat-punch indenter with a diameter of $10\mu m$. The system was placed inside a Zeiss EVO MA15 SEM and the wiring and water-cooling entered the SEM by special feedthroughs on the side walls of the vaccuum chamber.

The indenter and the hot stage containing the sample were individually heated. The set-temperature of the hot stage was adjusted such that the additional thermocouple connected to the sample surface indicated the desired temperature. Thermal matching between indenter and sample was performed by making contact with a sacrificial micropillar and measuring the thermal drift. The temperature of the indenter was then adjusted accordingly. In all cases thermal drift was below 0.5 nm/s. Alignment of the indenter and sample surface was performed by moving the indenter along the surface and measuring the distance to make surface contact at different locations along the surface. This was done in both orthogonal directions parallel to the surface plane and the sample rotation & tilt was adjusted accordingly. Alignment of the indenter and pillar axis was done using the built-in measurement software. Figure 5.2 gives a schmatic overview of the set-up inside the vaccuum chamber of the SEM. By knowing the system tilt angle $\phi$ and the approximate diamaters of the flat-punch indenter $d_fp$ and the top of the pillar $d_p$, basic trigonometry can be used to calculate the distance $h'$ the (larger) indenter should be overlapping the pillar at that perspective. The measurement software can then be used to align the system based on the obtained value for $h'$.

Micropillar compression experiments were performed on Cu/Nb ARB samples with average individual

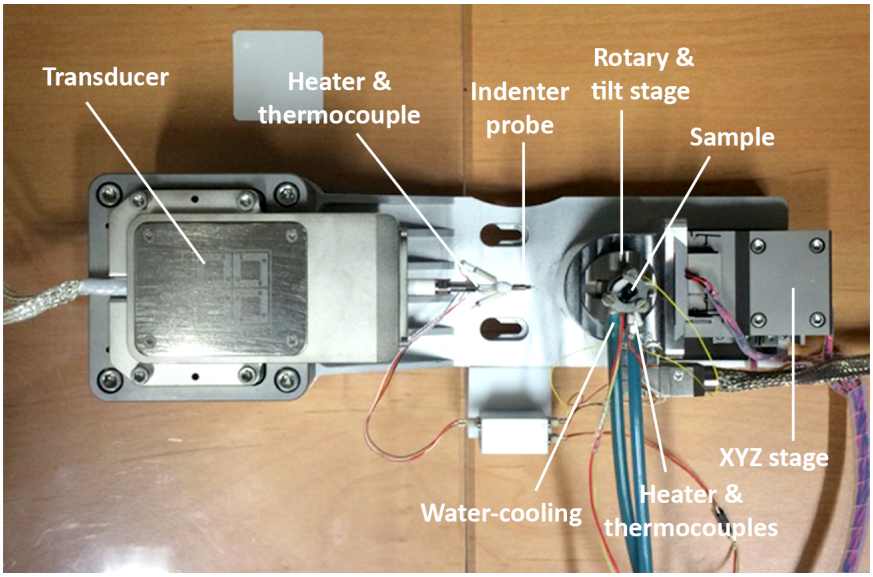


Figure 5.1: Image of the Hysitron PI87 SEM picoindenter showing the different components and set-up for high-temperature testing.

layer thickness of 7,16,34 and 63 nm at $20\,^oC$, $200\,^oC$ and $400\,^oC$. All compressions were strain-rate jump tests performed within the $10^{-2} - 10^{-4}\,s^{-1}$ strain-rate regime. Both taper-free and tapered micropillars were compressed. Yield strength was only determined from taper-free pillars, strain-rate sensitivity from both taper-free and tapered pillars. Table 5.1 gives an overview of the number of taper-free and tapered compressions per layer thickness and temperature, and the average dimensions of the taper-free pillars.

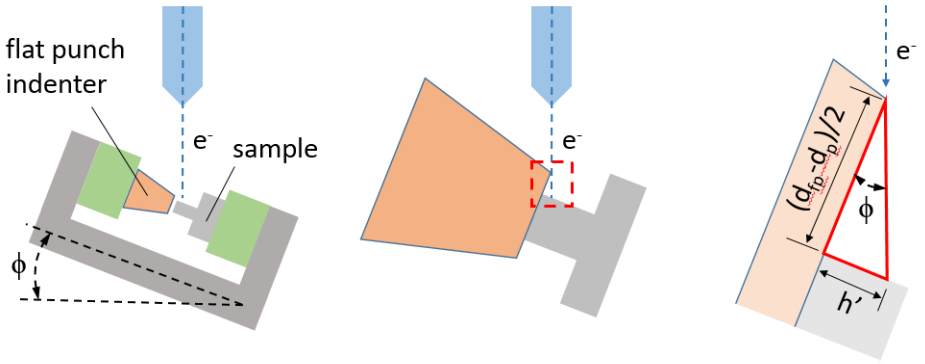


Figure 5.2: Schematic overview of test set-up for in-situ SEM testing and method for alignments of pillar and indenter. Alignments are performed with use of electron images and sytem is tilted by $\phi$ to provide a better perspective of the relative positions of pillar and indenter. The ideal alignment ($h'$) is calculated based on the diameter of the indenter ($d_{fp}$), the diameter of the top surface of the pillar ($d_p$) and the tilt of the system ($\phi$). The integrated measurement tool available in most SEMs can then be used to position the indenter according to the optimal $h'$ value.

For each layer thickness the compressions at various temperatures were performed on the same sample. For each sample all pillars have been exposed to the same thermal cycle[1]. For all samples a post-heating compression was performed to compare pillar behaviour before and after thermal exposure. Based on literature no significant alterations in the microstructure were expected for the current

[1]Total exposure times may vary a bit per test sample, but does not exceed 6 hours.

temperature range [49, 50, 53, 54, 73]. Comparison of room-temperature compressions before and after heating confirmed this. Furthermore the room-temperature results of the in-situ system were compared with the ex-situ results presented in Chapter 4. Yield strengths and strain-rate sensitivities were found to be reprodicible.

Table 5.1: Overview of the number of compressions performed on taper-free and tapered pillars per layer thickness sample and the average pillar dimensions of the taper-free pillars.

| **Layer thickness** | **Tapered compressions** $20\,^oC/200\,^oC/400\,^oC$ | **Taper-free compressions** $20\,^oC/200\,^oC/400\,^oC$ | **Diameter** ($\mu m$) | **Height** ($\mu m$) | **Taper** ($deg$) |
|---|---|---|---|---|---|
| 7 nm | 1/1/4 | 2/3/2 | 4.6$\pm$0.3 | 13.1$\pm$0.2 | 1.1$\pm$0.1 |
| 16 nm | 0/0/2 | 6/4/4 | 5.2$\pm$0.1 | 13.3$\pm$0.3 | 0.7$\pm$0.2 |
| 34 nm | 0/0/1 | 5/4/4 | 5.1$\pm$0.1 | 13.1$\pm$0.2 | 0.8$\pm$0.3 |
| 63 nm | 0/0/1 | 5/4/4 | 5.4$\pm$0.0 | 13.6$\pm$0.1 | 0.7$\pm$0.2 |

## 5.2 Results

SEM images of the deformed micropillars at different layer thicknesses and temperatures are presented in Figures 5.3 and 5.4. Deformation observed in the pillars at room-temperature was very similar to the deformation reported in Chapter 4. In the 63 nm pillars some bending was observed and signs of shear banding were present. Furthermore the compression curves showed flow stresses $\approx 0.2\,GPa$ lower than those reported in Chapter 4, possibly indicating small misalignments between pillar and indenter leading to some bending of the pillars. The compliance and stability issues of the hot stage for this particular sample could also have played a role.

At $200\,^oC$ deformation was very similar to deformation observed at room-temperature. The 7 nm and 16 nm samples showed strain-localization resulting in shear failure of the pillar. The shear lines appeared sharper at $200\,^oC$ than at room-temperature, such that failure at $200\,^oC$ seemed to be of more brittle nature. In the 34 nm pillars full shear failure was observed at $200\,^oC$ whereas under room-temperature conditions and similar strains only partial cracking was observed. Deformation behaviour of the 63 nm pillars at $200\,^oC$ appeared to be very similar to behaviour at room-temperature.

At $400\,^oC$ microcrystals were formed on the pillar walls and pillars were more unstable. The density of microcrystals appeared to increase with decreasing layer thickness, and appeared to form more readily in the higher stressed zones. Futhermore shear lines were present on the pillar surfaces at the finest thicknesses but no shear failure was observed.

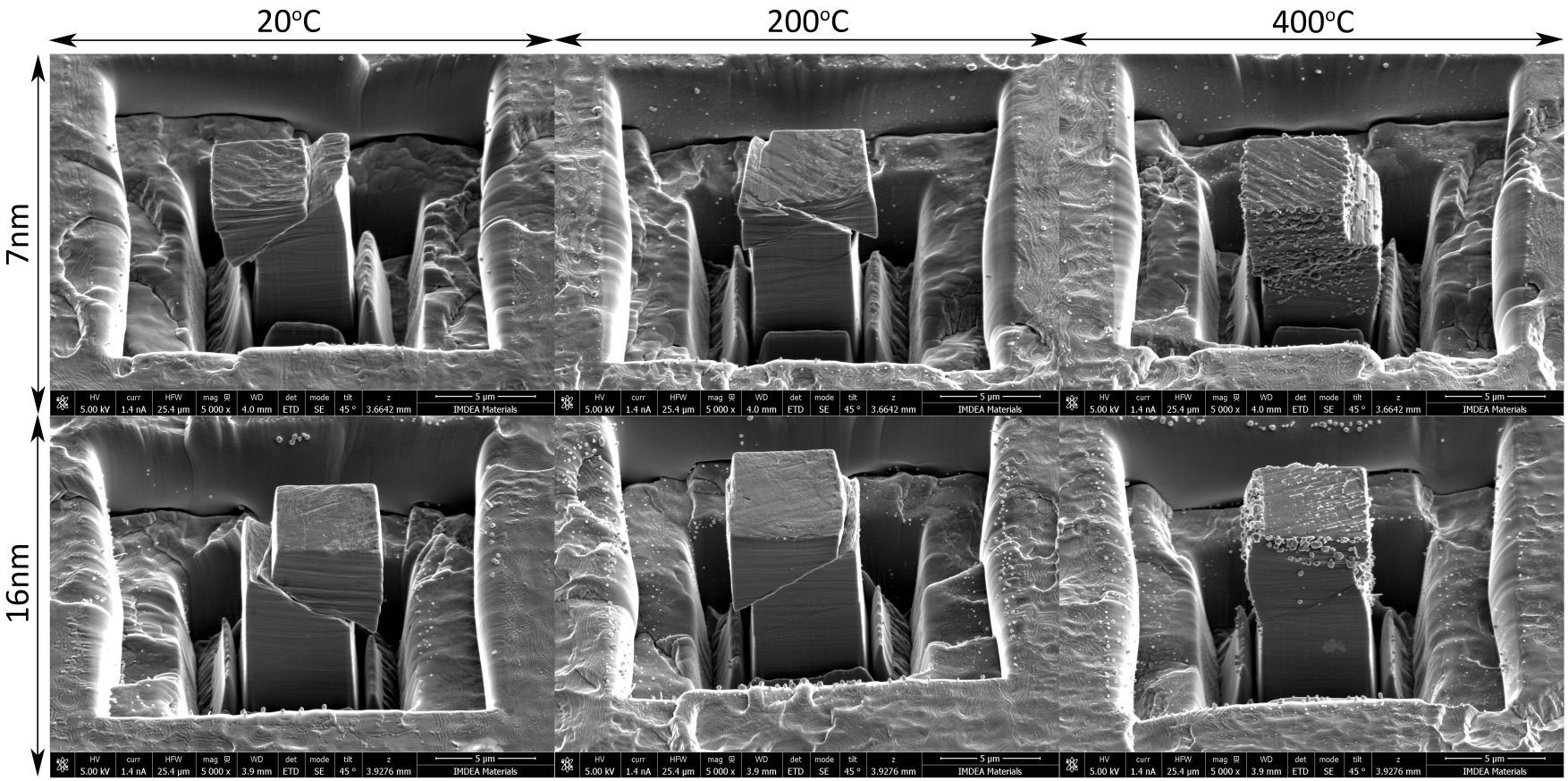


Figure 5.3: SEM images of deformed micropillars with individual layer thickness of 7 and 16 nm at $20^oC$, $200^oC$ and $400^oC$.

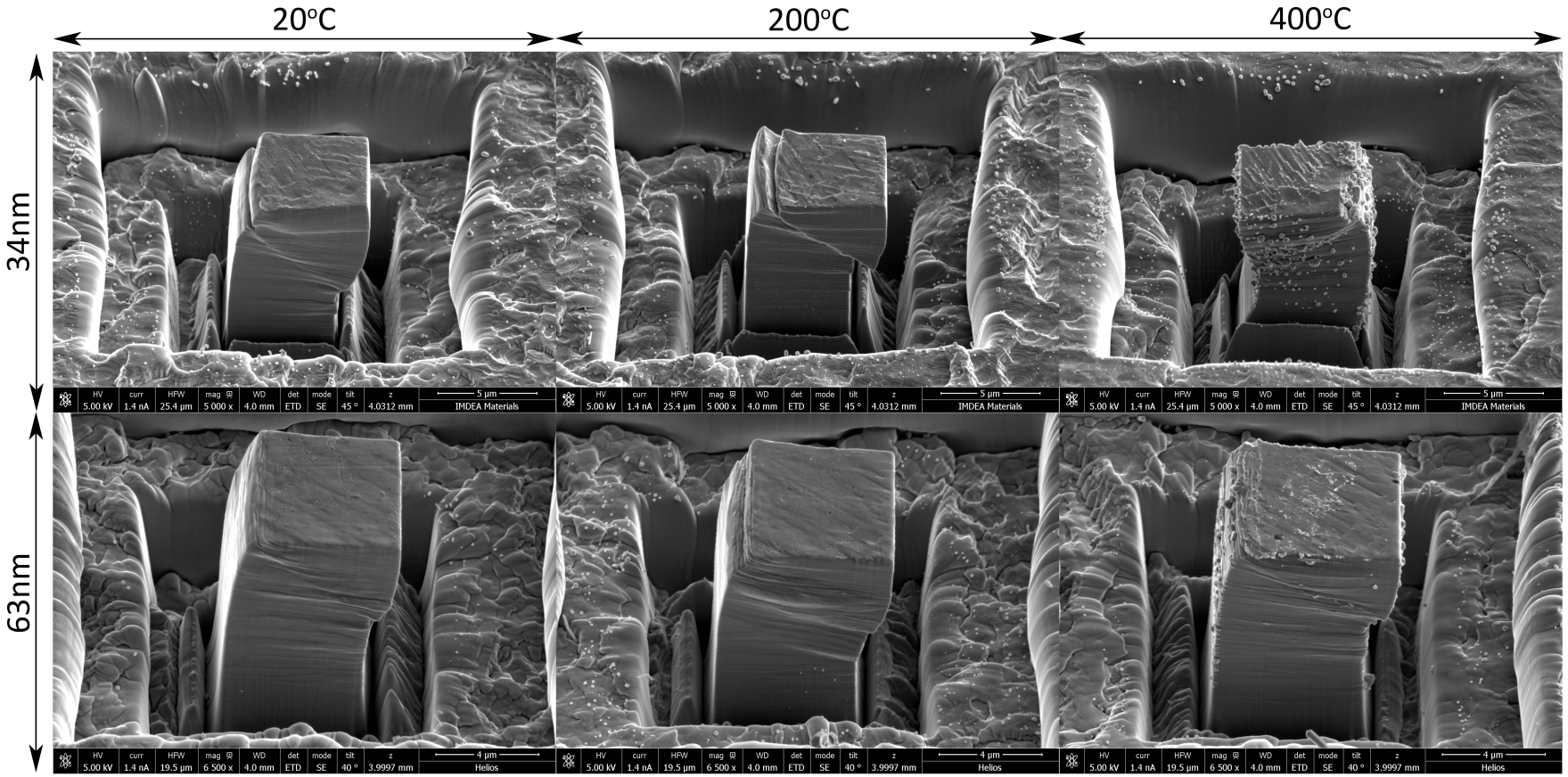


Figure 5.4: SEM images of deformed micropillars with individual layer thickness of 34 and 63 nm at $20^oC$, $200^oC$ and $400^oC$.

The obtained compression curves are presented in Figure 5.5. All compression curves have an initial loading strain-rate of $10^{-3}\,s^{-1}$. No room-temperature compression curves were obtained for the 7 nm sample due to the presence of angled layers in these particular pillars, thereby showing a significant reduction in strength. For the 63 nm sample the loading section of the curves were wobbly and a reduced modulus was observed. This is due to the use of a different hot stage in this particular experiment with which there were some difficulties with stability and compliance. As a result no yield strength could be determined, however it is not expected to affect the strain-rate sensitivity.

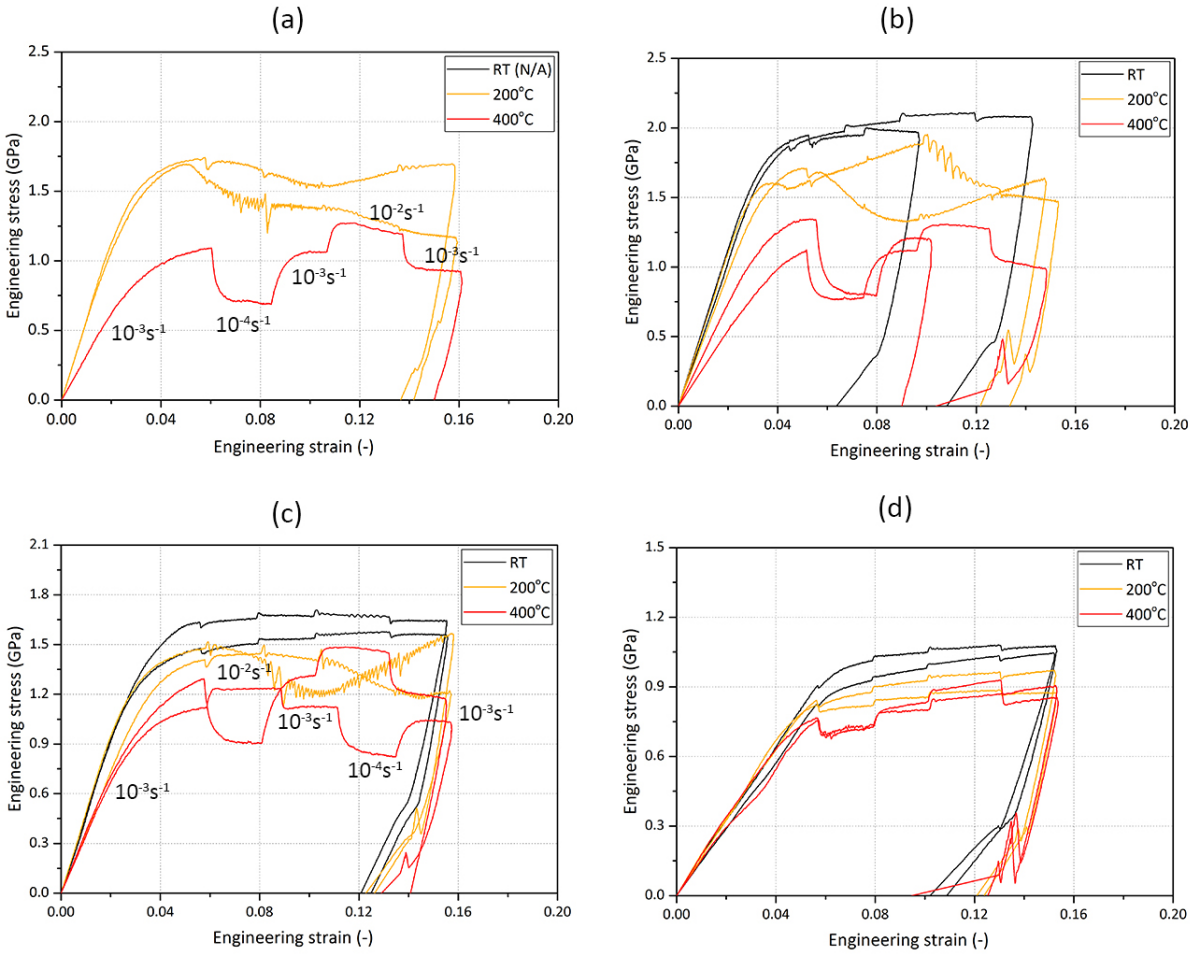


Figure 5.5: Representative (taper-free) compression curves of ARB Cu/Nb micropillars with average layer thickness of 7 nm (a), 16 nm (b), 34 nm (c) and 63 nm (d) nm at $20^oC$, $200^oC$ and $400^oC$. Strain-rates were predominantly applied in the following order unless stated otherwise: $10^{-3} - 10^{-4} - 10^{-3} - 10^{-2} - 10^{-3} s^{-1}$.

Comparing the flow stresses attained at different temperatures, the samples with finer layer thicknesses appeared to show a larger drop in strength at elevated temperatures than the samples with larger layer thicknesses. Furthermore the curves at the finest thicknesses and $200\,^oC$ showed flow serrations and appeared to show a reduced strain-rate sensitivity. At $400\,^oC$ a significant increase in strain-rate sensitivity was clearly visible for all layer thicknesses. The samples with the finest layer thicknesses appeared to show the highest strain-rate sensitivity. Furthermore a higher scatter was observed in the compression curves at $400\,^oC$, which is attributed to the height variations of the studied pillars. The height variations induced small variations in applied strain-rate between pillars which at high strain-rate sensitivity lead to more scatter.

## 5.3 Discussion

### 5.3.1 Deformation behaviour

At $200\,^oC$ the higher temperature appeared to promote shear failure in the pillars, as observed in the 34 nm pillars which did not shear at room-temperature under similar strains. Furthermore shear failure also appeared to be of more brittle nature. It therefore seems that plastic instabilities increased at $200\,^oC$. The strain-hardening capability of materials is generally known to decrease with temperature, and could explain the increased plastic instability and more brittle nature of failure at $200\,^oC$.

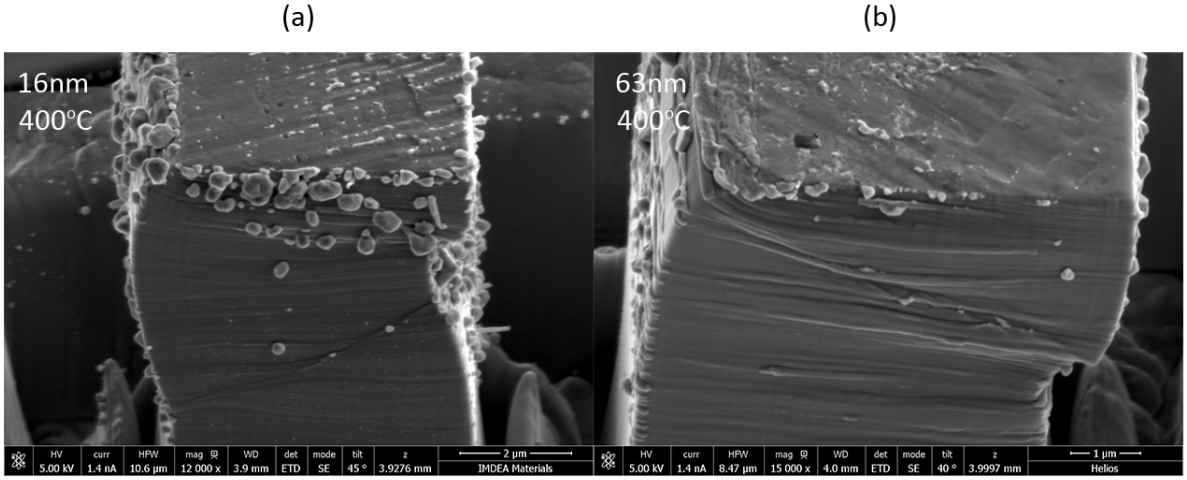


Figure 5.6: SEM images with a close-up of the 16 nm (a) and 63 nm (b) pillars compressed at $400\,^oC$. Microcrystal formation is more pronounced on the 16 nm sample. In the 63 nm pillar a shear band appeared to form.

At $400\,^oC$ microcrystals were formed on the pillar walls. Lotfian et al. and Raghaven et al. observed similar microcrystals in respectively Al/SiC and Cu/TiN metal-ceramic micropillars [24, 25]. Lotfian et al. reported massive extrusion of the Al layers at $100\,^oC$, from which they postulated that the extrusion might have been facilitated by interfacial diffusion. In the Cu/TiN micropillar studied by Raghaven et al., Cu microcrystals were formed on the pillar side walls at $200\,^oC$ and they attributed this to stress-assisted diffusion of Cu. EDX analysis on a cross-section of one of the compressed pillars confirmed the formation of Cu microcrystals on the pillar walls, as depicted in Figure 5.7b. An interesting difference is that in the Cu/TiN pillars microcrystals were already present at $200\,^oC$. In ARB Cu/Nb no microcrystals were formed at $200\,^oC$ and only at temperatures of $400\,^oC$ microcrystals were observed. This is likely explained by the relatively soft Nb layers in contrast to the hard TiN ceramic layers, with the Nb layers contributing more to deformation and thereby ”relieving” stresses in the Cu layers. It also shows that at these relatively low temperatures for diffusion, the stress level plays an important role.

Another interesting observation to mention for the 7 and 16 nm pillars is the presence of shear lines on the pillar surfaces but the absence of shear failure at $400\,^oC$, as shown in Figure 5.6a. The same study by Raghaven et al. showed that in Cu/TiN pillars Cu filled the cavities that formed along shear bands, indicating stress-assisted self-healing at elevated temperatures. The EDX image in Figure 5.7c confirms the presence of a similar healing mechanism in the current pillar in which Cu diffuses into shear band cavities, thereby (partially) recovering the crack and preventing shear failure of the pillar. Furthermore HRTEM also revealed the presence of deformation twins in the Cu layers at $400\,^oC$, which is also a known mechanism of deformation at room-temperature [4, 33, 47]. Twin size is $\approx$5-10 nm and consistent with sizes reported by Zheng et al. [47].

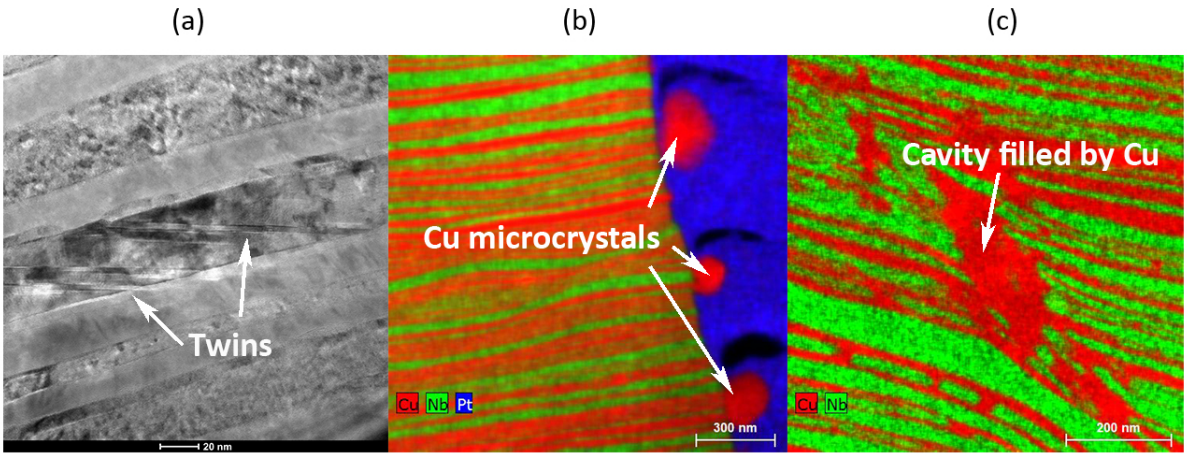


Figure 5.7: Images of TEM cross-section of 16 nm ARB Cu/Nb micropillar compressed at $400\,^oC$. (a) HRTEM image showing deformation twins in the Cu layers with twin size of $\pm$5-10 nm. (b) EDX image revealing Cu microcrystals on the free pillar walls and (c) EDX showing the filling of a cavity within the shear band by Cu.

### 5.3.2 Yield strength vs. temperature

The yield strength as a function of temperature for the different layer thicknesses is presented in Figure 5.8 and the values are summarized in Table 5.2. Important to emphasize is that the yield strength was determined at strain-rates of $10^{-3}\,s^{-1}$. In order to get a better understanding of multilayer strength dependencies at elevated temperatures, data on pure Cu and Nb have been added for comparison. Farrokh et al. studied the mechanical response of nc-Cu with a grain size of 32 nm at different temperatures by quasi-static and dynamic uniaxial compression tests [19]. The plotted strength values are yield strength values estimated from the compression curves, which were obtained at (higher) strain-rates of $10^{-2}\,s^{-1}$. Data on ufg-Cu is based on a study by Suo et al. [20] in which Cu with a grain size of 300 nm was compressed at strain-rates of $10^{-3}\,s^{-1}$. For Nb only data was available on material with a relatively large grain size of $32\,\mu m$. These compression experiments were performed at $10^{-3}\,s^{-1}$.

Table 5.2: Obtained yield strength values for ARB Cu/Nb at different temperatures.

| Layer thickness | $\sigma_y^{20\,^oC}$ (GPa) | $\sigma_y^{200\,^oC}$ (GPa) | $\sigma_y^{400\,^oC}$ (GPa) |
|---|---|---|---|
| 7 nm | 1.74 $\pm$ 0.14 | 1.28 $\pm$ 0.08 | 0.75 $\pm$ — |
| 16 nm | 1.64 $\pm$ 0.04 | 1.36 $\pm$ 0.08 | 0.90 $\pm$ 0.12 |
| 34 nm | 1.22 $\pm$ 0.03 | 1.13 $\pm$ 0.08 | 0.78 $\pm$ 0.08 |
| 63 nm | 0.78 $\pm$ 0.04 | 0.70 $\pm$ — | 0.60 $\pm$ — |

The yield strengths were found to correspond well with earlier nanoindentation hardness results at $300\,^oC$ and $400\,^oC$ reported by Monclús et al. [26]. For all layer thicknesses a decrease in strength was observed as the temperature increased. Similar to observations by Monclús et al., a relatively high drop in strength was observed in the sample with layer thickness of 7 nm, such that at $200\,^oC$ and $400^oC$ it is not the strongest sample anymore.

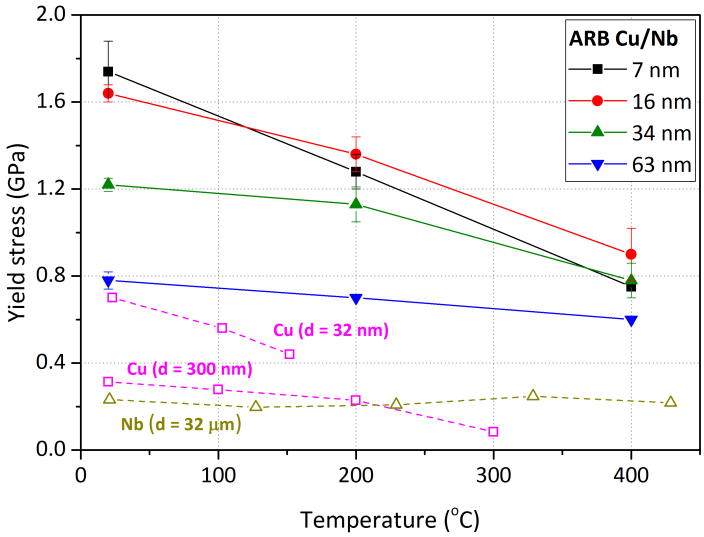


Figure 5.8: Plot of yield strength versus temperature for ARB Cu/Nb at different layer thicknesses. Data on nc-Cu and ufg-Cu are based on [19, 20]. Data on Nb is based on [21].

From Figure 5.8 two important observations can be made. First of all a general trend of increased thermo-mechanical stability with layer thickness was observed, i.e. temperature-induced softening decreases with increasing layer thickness. Despite the limited data, the plotted curves indicate a similar trend for Cu with the thermo-mechanical stability increasing with grain size. Furthermore softening at the finest thicknesses is consistent with softening observed in Cu with d = 32 nm. At larger thicknesses softening seems to approach that of Cu with grain size of 300 nm. Although trends for pure Nb at elevated temperatures are unknown for the ultra-fine grain and nanocrystalline regime, Nb is expected to be more temperature-stable even in the nanocrystalline regime due to the higher melting temperature ($T_m$ = 2741 K). The trends therefore suggest a profound role of Cu in the temperature behaviour of the multilayer, which would not be suprising considering the softer nature and significantly lower melting temperature of Cu ($T_m$ = 1356 K).

The second observation is related to the large softening observed at a layer thickness of 7 nm. Farrokh et al. and Suo et al. reported a decreasing strain-hardening capability for Cu at elevated temperatures [19, 20], to the extent that zero or even negative strain-hardening is observed for Cu with ultra-fine grains or smaller. It is not unlikely that at the finest multilayer thicknesses where strain-hardening capability is already extremely low, a temperature-related reduction in strain-hardening has a more detrimental impact on strength. Furthermore a decrease in strain-hardening capability also further promotes plastic instabilities, which seems compatible with the more brittle nature of shear failure and the increased plastic instability in the 7, 16 and 34 nm pillars at $200\,^oC$ as observed in the SEM images in Figures 5.3 and 5.4. It is therefore postulated that below a critical thickness, the additional strength gained by a layer thickness reduction at room-temperature might be exceeded by the reduction in strength due to the combined effects of reduced strain-hardening capability and increased plastic instability at elevated temperatures.

The planar stresses developing as a result of the thermal expansion mismatch between Cu and Nb can also affect the yield strength through the Von Mises construction. Taking coefficients of thermal expansion (CTE) of $\alpha_{Cu} = 16.6 \cdot 10^{-6}\,K^{-1}$ and $\alpha_{Nb} = 7.0 \cdot 10^{-6}\,K^{-1}$ and E-modulus of 130 GPa for the multilayer, the maximum mismatch planar stresses at $200\,^oC$ and $400\,^oC$ are estimated at respectively 225 MPa and 474 MPa. In Figure 5.8 one can see that at $200\,^oC$ these stress levels approach the yield

strength of nc-Cu, and could therefore contribute to the compressive yield strength through the Von Mises stresses. However, it is known that in-plane interfacial stresses are also present as a result of the lattice mismatch. The mismatch in lattice parameter between Cu and Nb results in tensile planar stresses in the Cu layers and compressive planar stresses in the Nb layers. The CTE mismatch is actually expected to partially relieve the stresses already present due to the lattice mismatch. Therefore if the planar stresses are high enough to contribute to the compressive yield strength through the Von Mises construction, the stresses developing as a result of thermal expansion are expected to lower the compressive yield strength of the multilayer.

### 5.3.3 Strain-rate sensitivity & activation volume vs. temperature

In Figure 5.9 the obtained strain-rate sensitivities and activation volumes are plotted. The values are summarized in Tables 5.3 and 5.4. Distinction was made between the $10^{-4} - 10^{-3}\,s^{-1}$ and $10^{-3} - 10^{-2}\,s^{-1}$ strain-rate regimes. Strain-rate sensitivities and activation volumes for ufg-Cu have been added based on the work by Suo et al. [20] mentioned in the previous section. The temperature-dependent SRS of nc-Cu was based on a study by Langlois et al. [74]. This study involved compressive strain-rate jump tests over a variety of strain-rates and temperatures on Cu with grain size of 90 nm. The strain-rates at which these strain-rate sensitivities have been determined were added for reference.

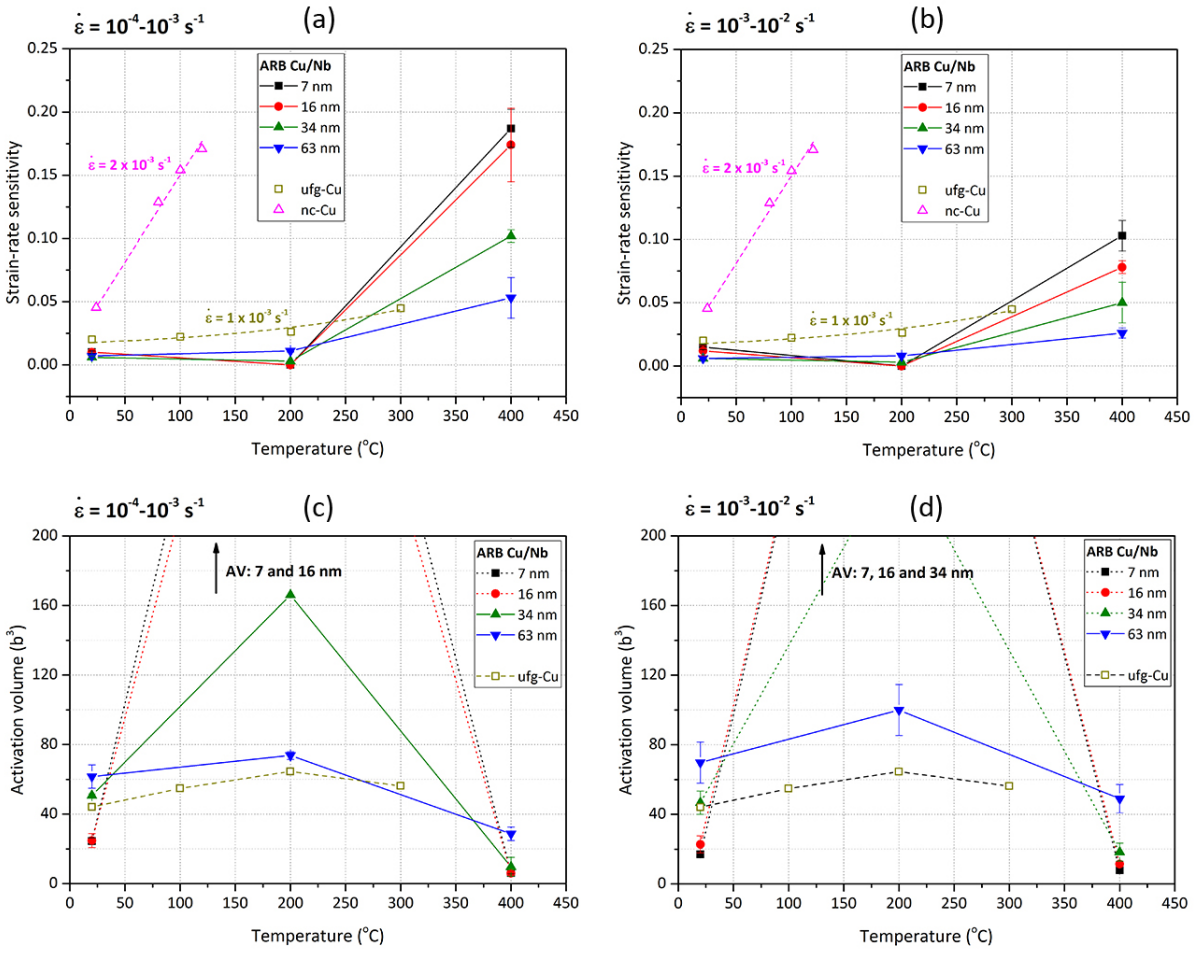


Figure 5.9: Plot showing strain-rate sensitivities (a+b) and activation volumes (c+d) for ARB Cu/Nb for the $10^{-4} - 10^{-3}\,s^{-1}$ and $10^{-3} - 10^{-2}\,s^{-1}$ strain-rate regimes and temperatures of $20\,^{o}C$, $200\,^{o}C$ and $400\,^{o}C$. The dotted curves act as a visual reference for the very high activation volumes obtained at $200\,^{o}C$ at the finer layer thicknesses.

Table 5.3: Strain-rate sensitivites and activation volumes obtained from compression for ARB Cu/Nb for strain-rate regime of $10^{-4} - 10^{-3}\,s^{-1}$.

| Layer thickness | SRS - $20\,^oC$ | SRS - $200\,^oC$ | SRS - $400\,^oC$ | V ($b^3$) $20\,^oC$ | V ($b^3$) $200\,^oC$ | V ($b^3$) $400\,^oC$ |
|---|---|---|---|---|---|---|
| 7 nm | 0.010±0.001 | ±0 | 0.19±0.01 | 24.5±2.0 | $\infty$ | 6.2±0.5 |
| 16 nm | 0.010±0.002 | ±0 | 0.17±0.03 | 24.8±4.0 | $\infty$ | 6.0±0.7 |
| 34 nm | 0.006±0.001 | 0.003±—— | 0.10±0.00 | 50.8±0.8 | 166.0±—— | 9.7±5.4 |
| 63 nm | 0.007±0.001 | 0.011±0.001 | 0.05±0.02 | 61.6±6.7 | 73.7±2.3 | 28.7±3.9 |

Table 5.4: Strain-rate sensitivites and activation volumes obtained from compression for ARB Cu/Nb for strain-rate regime of $10^{-3} - 10^{-2}\,s^{-1}$.

| Layer thickness | SRS - $20\,^oC$ | SRS - $200\,^oC$ | SRS - $400\,^oC$ | V ($b^3$) $20\,^oC$ | V ($b^3$) $200\,^oC$ | V ($b^3$) $400\,^oC$ |
|---|---|---|---|---|---|---|
| 7 nm | 0.015±0.002 | ±0 | 0.10±0.01 | 17.0±1.8 | $\infty$ | 7.9±0.7 |
| 16 nm | 0.012±0.004 | ±0 | 0.08±0.01 | 22.7±4.9 | $\infty$ | 11.4±1.5 |
| 34 nm | 0.006±0.001 | —— | 0.05±0.02 | 46.7±6.7 | —— | 18.3±5.2 |
| 63 nm | 0.006±0.001 | 0.008±0.001 | 0.03±0.00 | 69.8±11.8 | 100.0±14.6 | 49.0±8.1 |

From Figure 5.9 it can be seen that the strain-rate sensitivities of the multilayer follows the trend of ufg-Cu better than that for nc-Cu. Similar to the room-temperature conditions, the much lower SRS of the multilayer compared to nc-Cu is likely due to the inherent difficulty of interface and/or grain boundary sliding processes, which become prominent in polycrystalline materials at very fine grain sizes and are further enhanced by higher diffusion rates at elevated temperatures. For ufg-Cu deformation is expected to be controlled predominantly by glide, as supported by the lower strain-rate sensitivities and (higher) activation volumes[2]. As can be seen the values for $m$ and $V$ for ufg-Cu seem to correspond well to that of the multilayer with layer thickness of 63 nm.

**Deformation at $200\,^oC$**

For the 7, 16 and 34 nm samples a decrease in strain-rate sensitivity was observed at $200\,^oC$. For the 7 and 16 nm samples no reliable SRS could be obtained. From the compression curves in Figure 5.5 one can see that there is almost no change in flow stresses at the strain-rate steps, indicating an SRS close to zero. For the 34 nm sample a small SRS of $\pm 0.003$ was obtained. At layer thickness of 63 nm the SRS increased from $0.007$ at room-temperature to $0.010$ at $200\,^oC$. The near-zero strain-rate sensitivities for the 7 and 16 nm samples at $200^oC$ result in extremely high activation volumes. At larger layer thicknesses the activation volume decreases.

The decrease in SRS for the 7, 16 and 34 nm samples at $200\,^oC$ is remarkable. In Chapter 4 it was

[2]Although the activation volume of nc-Cu was not reported [74], based on the trends of higher flow stress and higher SRS a smaller activation volume is expected.

postulated that at these thicknesses and at room-temperature interfaces control deformation, likely by dislocation nucleation and/or emission at interfaces. It appears that at $200\,^oC$ some thermal activation or change in mechanism occurs such that the SRS is close to zero. A zero or negative SRS in combination with the flow serrations observed in the compression curves are typical for the Portevin-Le Chatelier (PLC) effect [75]. This effect is generally observed in materials containing solutes. Furthermore the fact that no decrease in SRS is observed in Cu at elevated temperatures suggests that it is likely related to the interfaces, the Nb layers or both.

Nemat-Nasser et al. studied the compressive behaviour of commercially pure Nb (99.9%). They observed dynamic strain ageing characterized by an insensitivity of flow stresses to temperature within the 400-600 K temperature range. Although this does not directly explain the strain-rate insensitivity of the multilayer, it does show that at $200\,^oC$ (473 K) even a small atomic fraction of impurities can already lead to dynamic strain ageing. Furthermore, Schneider et al. reported a critical temperature of $350\,K$ for Nb where edge and screw dislocations have equal mobility due to thermal activation of the screw dislocations [76]. Based on this observation a transition is expected between room-temperature and $200\,^oC$ where the mode of deformation of Nb changes from BCC-type deformation controlled by screw dislocations to FCC-type behaviour with negligible lattice friction.

Based on these observations by Nemat-Nasser et al. and Schneider et al., it is speculated that deformation at $200\,^oC$ might be affected in different ways. It is expected that at $200\,^oC$ the contribution of the Nb layers to deformation will increase due to the transition from BCC to a softer FCC-type behaviour. If deformation is controlled by the Nb layers at this temperature, dynamic strain ageing could occur. However since this mechanism of deformation would be purely related to the Nb layers and not to the interfaces, no dependendency on layer thickness would be expected and dynamic strain ageing would be observed at all thicknesses. The increase in SRS with layer thickness suggests differently and dynamic strain ageing therefore seems an unlikely scenario. Alternatively it is speculated that the negligible lattice friction in the Nb layers at $200\,^oC$ might "relax" the pinning of dislocations. The reduced interaction of lattice dislocations with misfit dislocation could thereby promote dislocation transmission across interfaces, and reduce the strain-rate sensitivity. This is supported by the faster and more brittle nature of shear failure in the $200\,^oC$ pillars.

If the transition from BCC to FCC-type behaviour of Nb has a negligible effect on multilayer behaviour, the reduced SRS is more likely related to thermal activation. At room-temperature (thermally activated) dislocation nucleation and/or emission from interfaces was predicted to be the controlling mechanisms of deformation. It is postulated that the room-temperature barrier for emission of partial dislocations from interfaces could disappear at $200\,^oC$, making it more of an athermal process with reduced strain-rate sensitivity. Unfortunately the extremely high activation volumes at these thicknesses do not provide further support for this prediction. Activation volumes of this order would normally be compatible with dislocation forest cutting ($V > 1000\,b^3$). However this seems unlikely at these fine layer thicknesses.

At 63 nm a slight increase in SRS is observed at $200^oC$. Activation volumes also increase but are still compatible with the confined layer slip regime ($V = 10 - 100\,b^3$). Furthermore considering the similar pillar deformation at room-temperature and $200\,^oC$, it is expected that deformation is also controlled by glide of single dislocations. The intermediate SRS at layer thicknesses of 34 nm suggests activity of both glide and the mechanism responsible for deformation at the finest thicknesses. Considering that the pillars fail by shear, it is expected that the rate-controlling mechanism of deformation is similar to that observed in the 7 and 16 nm samples. The increase in SRS compared to the finest thicknesses suggests an increasing contribution of dislocation glide to deformation.

**Deformation at** $400\,^oC$

At $400\,^oC$ all samples showed a significant increase in SRS. The SRS decreased with higher applied strain-rate, which is what one expects of a thermally activated mechanism. The 7 nm sample showed

the highest SRS, which was in the range of 0.10-0.20 depending on the strain-rate regime. Strain-rate sensitivity then gradually decreased with layer thickness, down to an SRS of $\pm$0.04 at layer thickness of 63 nm. For all samples activation volumes were smaller than values at room-temperature and $200\,^oC$. For the 7 and 16 nm samples average activation volumes were close to $10\,b^3$. The 34 nm sample showed slightly higher activation volumes of $\pm 14\,b^3$. Average activation volumes for the 63 nm sample were significantly higher ($\pm 39\,b^3$).

For the 7 and 16 nm samples compressed at lower strain-rates an SRS of $\pm\,0.18$ was obtained, which is compatible with dislocation climb. Activation volumes are of the order of $6\,b^3$ which in-turn are compatible with diffusional processes and/or dislocation nucleation/emission at interfaces. It is known that dislocation climb generally occurs at high stresses and $T > 0.5T_m$, and is assisted by diffusion. At $400\,^oC$ the temperature approaches the temperature domain for dislocation climb in Cu. Furthermore the Cu microcrystals formed on the pillar walls confirm diffusion of Cu atoms to free surfaces. Although the formation of crystals is a signature of diffusion, diffusion itself does not explain the formation of crystals. Apparently there is a driving force to nucleate a new phase on the free surface. Atomistic modeling studies by Wang et al. previously predicted dislocation climb to occur in PVD Cu/Nb at the interfaces, which was experimentally verified by in-situ indentation on Al-Nb multilayers in a TEM [34]. Based on this observation and the results on $m$ and $V$, diffusion-assisted dislocation climb seems a likely scenario at $400\,^oC$ and low strain-rates.

At higher strain-rates the strain-rate sensitivity decreases. It is expected that the shorter diffusion times at increased strain-rates limit diffusion-related deformation processes. In order to cope with the high rate of deformation, dislocation-based processes become more prominent and result in a reduction of strain-rate sensitivity. Furthermore in the case of Coble-type diffusion a dependency of the diffusion rate on grain size/layer thickness is expected. The decreasing SRS with increasing layer thickness is likely a reflection of decreasing diffusion activity. Furthermore the SEM images showed a decrease in Cu microcrystal formation with increasing layer thickness, which suggests Coble-type diffusion along interfaces to take place. In Chapter 4 it was postulated that shear failure was likely related to the nucleation and emission of dislocations from interfaces. Based on the shear lines observed at $400\,^oC$ in the SEM images, nucleation and emission of dislocations also plays a role at these temperatures. However full shear failure is not observed which is likely due to the high diffusivity of Cu acting as a stress-assisted healing agent at these temperatures.

At larger thicknesses the strain-rate sensitivity decreases. It is believed that at these thicknesses diffusion along interfaces becomes increasingly difficult and a transition from diffusion-related processes to deformation by glide occurs. At a layer thickness of 63 nm $m$ and $V$ are compatible with glide processes. Although some diffusion still takes place as observed in the SEM image, the results indicate confined layer slip to be the rate-controlling mechanism of deformation. This implies that at a layer thickness of 63 nm and based on $m$ and $V$, the same rate-controlling mechanism is operative within the $20-400\,^oC$ temperature range. Both the SEM images showing similar deformation over the studied temperature range and the relatively small softening observed at increasing temperatures support this statement. The increase in SRS with temperature is therefore believed to be mainly due to thermal activation of glide together with a small increase in diffusion-related process, but not due to a change in rate-controlling mechanism.

For the 34 nm sample, strain-rate sensitivities are in-between the values of $m$ for both processes and the activation volumes ($V \approx 10 - 18\,b^3$) are close to the transition from grain boundary diffusion to glide of single dislocations. Deformation at $400\,^oC$ is therefore believed to be a mix of diffusion-assisted dislocation climb and dislocation glide. Furthermore no shear lines were observed on the pillar surfaces, suggesting a decreased activity of dislocation nucleation/emission from interfaces.

## 5.4 Conclusion

The high-temperature compression experiments on ARB Cu/Nb showed an increase in thermo- mechanical stability with layer thickness. At thicknesses below ≈20 nm diffusion was found to play a dominant role in deformation at elevated temperatures. A link between layer thickness and diffusion-rate was found, suggesting Coble-type diffusion along interfaces. Strain-rate sensitivities and activation volumes suggested diffusion-assisted dislocation climb to be the rate-controlling mechanism of deformation at the highest temperatures.

At larger thicknesses of 63 nm diffusion was found to play a less prominent role. The results indicated a transition to deformation controlled by glide of single dislocations. This mechanism was found to be rate-controlling at all temperatures, and a relatively weak dependency of mechanical properties and deformation behaviour on temperature was found.

At the finest thicknesses no strain-rate sensitivity was observed at $200\,^oC$. Some postulations were made on possible temperature-induced mechanistic changes inside the material. However these are suggestions for future research. With respect to the application of the material in nuclear industry, observations indicate a competition between strength and diffusion-related deformation processes at the finest thicknesses, and do not look promising for the creep properties of the material at the finest thicknesses for neutron irradiation conditions.

# Chapter 6

# Conclusions and recommendations

The mechanical properties and deformation behaviour of ARB Cu/Nb metallic multilayers as a function of layer thickness and temperature was investigated by means of micropillar compression and nanoindentation. The thesis was divided into three core chapters. Chapter 3 focused on the experimental uncertainties related to pillar taper and microstructural variations when performing micropillar compression experiments. In Chapter 4 the room-temperature behaviour of the material was studied as a function of layer thickness. In Chapter 5 the high-temperature behaviour of the material was studied at temperatures of $200\,^oC$ and $400\,^oC$.

In order to shed some light on the experimental uncertainties of ARB Cu/Nb tested by micropillar compression, a small study was performed on the effects of taper and microstructural variations on the obtained yield strength and strain-rate sensitivity. The study revealed that both taper and microstructure strongly affect the yield strength. The yield strength needs to be geometrically corrected for taper, and the most accurate method proved to be the stress at average cross-sectional area. Microstructural variations were found to have a similar effect on pillar strength as taper. For ARB manufactured multilayers it is strongly advised to take images of each individual pillar before compression since microstructural artefacts can often explain deviating results from the compression experiments. The strain-rate sensitivity obtained by strain-rate jump tests was found to be independent of both taper and microstructure.

The room-temperature studies on ARB Cu/Nb multilayers with 7, 16, 34 and 63 nm layer thickness revealed an increase in strength with decreasing layer thickness and two competing deformation mechanisms. At the higher thicknesses it can be said with reasonable certainty that deformation is controlled by glide of single dislocations. As the layer thickness decreases a transition is observed to a different mechanism characterized by strain-localization and shear failure of the pillars. Activation volumes strongly suggest deformation to be related to the interfaces, possibly by the nucleation and emission of dislocations. This mechanism was found to be compatible with the twinning propensity of the material at the finest thicknesses. Hall-Petch behaviour was not observed in the current thickness range, indicating a transition from confined layer slip to Hall-Petch type deformation at thicknesses larger than 63 nm.

The high-temperature compression studies revealed an increasing thermomechanical stability with layer thickness. With increasing temperature diffusion was found to play a dominant role at the finest thicknesses. At $400\,^oC$ and strain-rates of $10^{-4} - 10^{-3}\,s^{-1}$ dislocation climb assisted by Coble-type diffusion was expected to be the rate-controlling mechanism of deformation. At increasing layer thickness and higher strain-rates diffusion-related processes were found to decrease and the results suggested a transition to dislocation glide as the rate-controlling mechanism. At $200\,^oC$ the material was found to be strain-rate insensitive at the finest thicknesses. Although no explanation could be given for the decrease in strain-rate sensitivity, it was postulated that this might be related to an increased contribution of the Nb layers above the critical temperature and/or thermal activation of the dislocation nucleation and emission mechanism.

In relation to the potential application of Cu/Nb multilayers in nuclear reactors, the results have shown that the high density of interfaces responsible for the outstanding irradiation resistance of the material also promote Coble-type diffusion. At typical operating temperatures of $600\,^oC$ for nuclear reactors, the material is expected to show significant creep when applied as a (static) coating. Creep can be suppressed by increasing the layer thicknes. However, this will also reduce the strength and irradiation properties of the material. It is up to future research to investigate whether at larger thicknesses the functional properties still fulfil the requirements for the application as a radiative coating.

Furthermore a few interesting observations were made over the course of this thesis, for which further research is proposed. Shear failure of pillars was observed to occur towards the rolling direction of the material. This strongly suggests a link between direction of shear and the texture of the material. Given the interface texture, atomistic modeling is proposed to further investigate these textural differences, with the emphasis being on the activation of slip systems at different orientations.

For the Cu/Nb multilayers showing a decreased strain-rate sensitivity at $200\,^oC$, TEM analysis is recommended. The amount of thinning of individual layers and/or dislocation activity inside the layers could potentially shed some light on whether the reduced strain-rate sensitivity is related to the Nb layers or the interfaces. If TEM analysis does not reveal any significant differences with deformation at room-temperature, answers are likely to be found by atomistic modeling. Regarding activation energies, the limited temperatures at which the material was tested made it impossible to determine activation energies. It is recommended to perform additional experiments at $100\,^oC$ and $300\,^oC$ in order to study the thermal activation of the different deformation mechanisms.

Furthermore from the experimental side involving compression experiments with the Hysitron PI87 SEM picoindenter, it is recommended to develop procedures to minimize compliance issues. The results have shown that compliance significantly alters the shape of the compression curves and it is difficult to correct the curves afterwards. Although these compliance issues do not affect the yield strength and strain-rate sensitivities, the E-modulus and other parameters such as strain-hardening exponents can only be determined from curves obtained under compliant conditions.

# Acknowledgements

This thesis would not have been possible without the help and support of many people.

First and foremost I would like to thank my principal supervisor Dr. Jon Molina for giving me the opportunity to work on the topic of nanoscale multilayers at the IMDEA Materials Institute. His extensive knowledge of and vast experience with multilayered materials and nanoscale testing, and the many fruitful discussions we had have been a continuous source of inspiration to me and the project. Equal gratitude goes out to my daily supervisor Dr. Miguel Monclús for teaching me many of the experimental techniques and supporting me in the day-to-day operations. Furthermore I would like to thank the director of IMDEA Prof.dr.ir. Javier Llorca for giving me the opportunity to do my MSc thesis at the institute, and for showing a continuous interest in the progress and results of the project. Lastly, I would like to thank the technicians and other people that have helped me and my fellow colleagues for making my time at IMDEA and in Spain an unforgettable experience.

I would also like to take the opportunity to thank my second supervisor Prof.dr.ir Sybrand van der Zwaag. His vast knowledge and experience in the field of material science has been of great value in shaping the research into a MSc thesis.

Lastly, I would like to thank family and friends for their continous support, faith and motivation.

# Appendix

In order to process the data consistently a Matlab script was developed. The majority of data corrections, data conversions and extraction of material parameters as outlined in Section 2.4 were performed by the script. Processing of compression data and indentation data differed. A schematic overview of the processing of compression data is given in Figure 1. For nanoindentation less processing steps were needed. Important to note is that the script only processes data. Data analysis is done afterwards in Excel.


Figure 1: Schematic diagram of processing of experimental data in Matlab.

## Micropillar compression

For micropillar compression the input consisted out of the compression curves (force and displacement) and a file containing the pillar dimensions[1] and pillar test conditions[2]. First a smoothing spline is applied to prepare the curves for further processing and to reduce the number of data points[3]. In the second step the initial plasticity correction and the Sneddon correction are applied. Initial plasticity is corrected by the aid of a moving average curve. The process is shown in Figure 2a. A moving average curve is plotted over the original curve to reveal the trend of the loading section and filter out noise and/or fluctuations. A point is then manually selected from which the original curve is extrapolated using the slope of the moving average curve. Finally the curve is shifted such that the zero load point coincides with the origin of the graph. The Sneddon correction is applied according to the method explained in Section 2.4.2. The influence of the corrections on the curves are illustrated in Figure 2b.

In the third step the corrected data is converted to engineering and true stress and strain as outlined in Section 2.4.2. Figure 2 shows the compression curves after conversion to engineering and true stress-strain. The lower stress levels and higher strains of the true stress-strain are due to the constant volume assumption and the logarithmic relation between strain and pillar length. In the fourth step material parameters are extracted from the compression curves. Distinction is made between CSR and SRJ tests. The yield strength and E-modulus are extracted from both types of tests. As depicted in Figure 4, the yield strength is determined by calculating the intersection of the curve with the loading modulus at 0.2% plastic strain. The E-modulus is determined by fitting a linear curve to the unloading section between $0.9\sigma_{\epsilon_{max}}$ and $0.4\sigma_{\epsilon_{max}}$[4]. The strain-rate sensitivity is only determined from the SRJ

[1] For each pillar the height, top diameter, bottom diameter and the cross-sectional shape is given.
[2] Describing the type of test (e.g. CSR or SRJ), the compression rate, or the compression sequence for SRJ tests
[3] This is done to limit the file size for further analysis in Excel.
[4] This range was chosen to: (1) avoid the hold segment at $\epsilon_{max}$ where the stress decreases due to relaxation and (2) avoid the last part of the unloading segment where deviations from linear unloading are regularly observed.

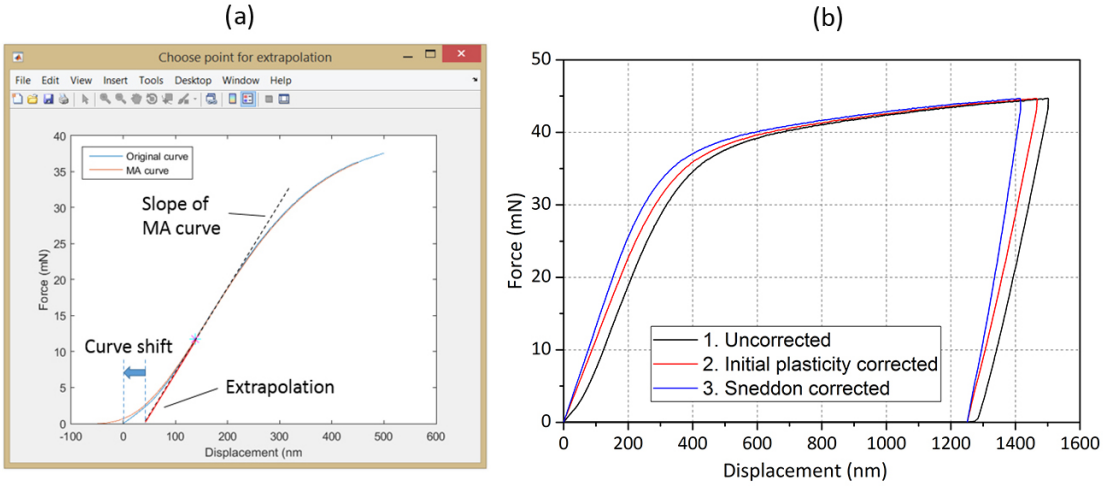


Figure 2: Method for correcting initial plasticity (a) and the effect of the initial plasticity correction and Sneddon correction on the compression curve (b).

tests. A transition point and two points on a linear part of the strain-rate segment are manually chosen as depicted in Figure 4a. A linear curve is fitted between the points and extrapolated to the strain at the jump point ($\epsilon_{jump}$). Strain-rate sensitivity is then calculated according to Equation 2.23 given in Section 2.4.5.

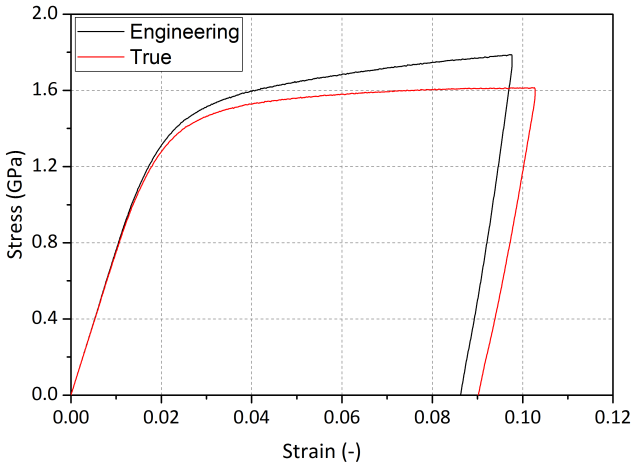


Figure 3: Engineering and true stress-strain curves after conversion from force-displacement.

In the last step the processed results are exported to an Excel file and figures are created. The Excel file contains the corrected force-displacement curves, engineering stress-strain curves and true stress-strain curves. Furthermore it contains the yield strength and E-modulus[5], and the different strain-rate sensitivities for each strain-rate jump test. Several other parameters such as maximum stress and maximum strain are also exported. For each compression experiment a figure with the data corrections and a figure containing the stress-strain curves with the unloading fits are exported, For strain-rate jump tests additional figures are exported containing the linear fits to each strain-rate segment, which in a later stage are used to analyze the jumps.

[5]Yield strength and E-modulus are determined for both the engineering and true stress-strain curves

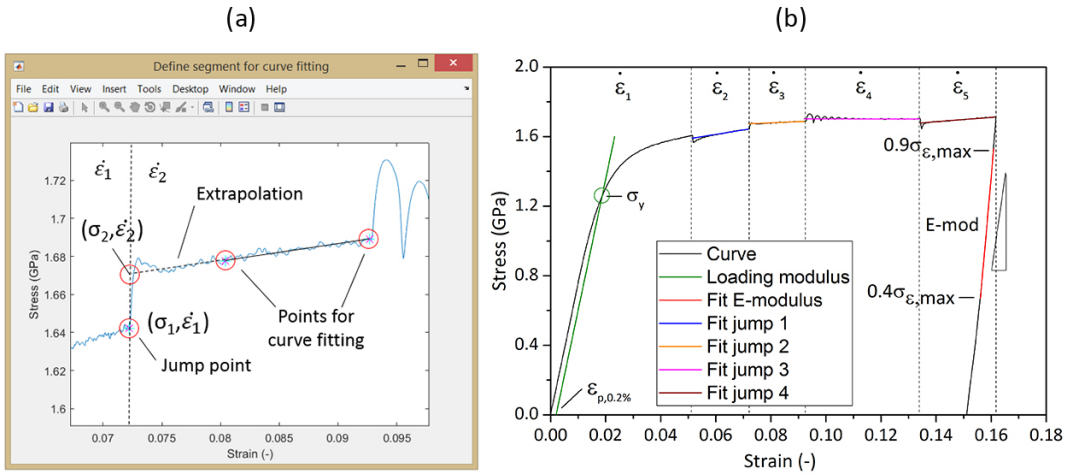


Figure 4: Method for determining transition points and flow stresses in Matlab to calculate strain-rate sensitivities (a) and methods for extracting material parameters from stress-strain curves (b).

# Nanoindentation

During processing of nanoindentation data no pre-processing or experimental corrections have to be applied. In the data conversion step the force is converted to instantaneous hardness according to Equation 2.14 given in Section 2.4.3. Figure 5a and b shows a force-displacement curve obtained from nanoindentation, and the curve after conversion to instantaneous hardness.

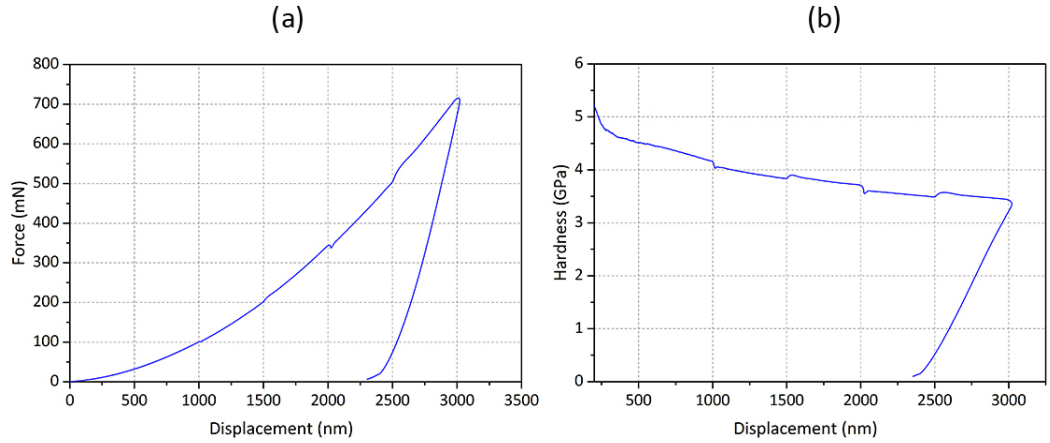


Figure 5: Example of nanoindentation force-displacement curve (a) and hardness-displacement curve after conversion (b).

Hardness and E-modulus are determined by by the integrated software of the Hysitron platform and not by the Matlab script. Strain-rate sensitivities are determined by the Matlab script. The SRS is determined from the hardness-displacement curves in a similar fashion as for micropillar compression. Finally the force-displacement curves, hardness-displacement curves and strain-rate sensitivities are exported to Excel. Figures with the linear fits to the strain-rate segments are also exported.

# Bibliography


[1] I. J. Beyerlein, N. A. Mara, J. Wang, J. S. Carpenter, S. J. Zheng, W. Z. Han, R. F. Zhang, K. Kang, T. Nizolek, and T. M. Pollock, "Structure-property-functionality of bimetal interfaces," *Jom*, vol. 64, no. 10, pp. 1192–1207, 2012.

[2] A. Misra, J. P. Hirth, and R. G. Hoagland, "Length-scale-dependent deformation mechanisms in incoherent metallic multilayered composites," *Acta Mater.*, vol. 53, no. 18, pp. 4817–4824, 2005.

[3] J. Wang and A. Misra, "Strain hardening in nanolayered thin films," *Curr. Opin. Solid State Mater. Sci.*, vol. 18, no. 1, pp. 19–28, 2014.

[4] S. Zheng, J. Wang, J. Carpenter, W. Mook, P. Dickerson, N. Mara, and I. Beyerlein, "Plastic instability mechanisms in bimetallic nanolayered composites," *Acta Mater.*, vol. 79, pp. 282–291, 2014.

[5] S. Lotfian, *High temperature mechanical behavior of Al/SiC nanoscale multilayers*. PhD thesis, Universidad Carlos III de Madrid, 2014.

[6] M. S. Tech, "Nanoindenters from micro star technologies," 2016.

[7] M. D. Uchic, D. M. Dimiduk, R. Wheeler, P. a. Shade, and H. L. Fraser, "Application of micro-sample testing to study fundamental aspects of plastic flow," *Scr. Mater.*, vol. 54, no. 5, pp. 759–764, 2006.

[8] J. M. Wheeler and J. Michler, "Elevated temperature, nano-mechanical testing in situ in the scanning electron microscope," *Rev. Sci. Instrum.*, vol. 84, no. 4, 2013.

[9] I. J. Beyerlein, N. A. Mara, J. S. Carpenter, T. Nizolek, W. M. Mook, T. A. Wynn, R. J. McCabe, J. R. Mayeur, K. Kang, S. Zheng, J. Wang, and T. M. Pollock, "Interface-driven microstructure development and ultra high strength of bulk nanostructured Cu-Nb multilayers fabricated by severe plastic deformation," *J. Mater. Res.*, vol. 28, no. 13, pp. 1799–1812, 2013.

[10] D. R. P. Singh, N. Chawla, G. Tang, and Y. L. Shen, "Micropillar compression of Al/SiC nanolaminates," *Acta Mater.*, vol. 58, no. 20, pp. 6628–6636, 2010.

[11] W. Oliver and G. Pharr, "Measurement of hardness and elastic modulus by instrumented indentation Advances in understanding and refinements to methodology," *Mater. Res. Soc.*, vol. 19, no. 1, pp. 3–20, 2004.

[12] G. Mohanty, J. M. Wheeler, R. Raghavan, J. Wehrs, M. Hasegawa, S. Mischler, L. Philippe, and J. Michler, "Elevated temperature, strain rate jump microcompression of nanocrystalline nickel," *Philos. Mag.*, no. October, pp. 1–18, 2014.

[13] M. a. Meyers, A. Mishra, D. J. Benson, Meyers M.A., Mishra A., and B. D.J., "Mechanical properties of nanocrystalline materials," *Prog. Mater. Sci.*, vol. 51, no. 4, pp. 427–556, 2006.

[14] I. C. Choi, Y. J. Kim, Y. M. Wang, U. Ramamurty, and J. I. Jang, "Nanoindentation behavior of nanotwinned Cu: Influence of indenter angle on hardness, strain rate sensitivity and activation volume," *Acta Mater.*, vol. 61, no. 19, pp. 7313–7323, 2013.

[15] Z. Pan, F. Xu, S. N. Mathaudhu, L. J. Kecskes, W. H. Yin, X. Y. Zhang, K. T. Hartwig, and Q. Wei, "Microstructural evolution and mechanical properties of niobium processed by equal channel angular extrusion up to 24 passes," *Acta Mater.*, vol. 60, no. 5, pp. 2310–2323, 2012.

[16] A. Misra and R. G. Hoagland, "Plastic flow stability of metallic nanolaminate composites," *J. Mater. Sci.*, vol. 42, no. 5, pp. 1765–1771, 2007.

[17] Q. Wei, S. Cheng, K. T. Ramesh, and E. Ma, "Effect of nanocrystalline and ultrafine grain sizes on the strain rate sensitivity and activation volume: Fcc versus bcc metals," *Mater. Sci. Eng. A*, vol. 381, no. 1-2, pp. 71–79, 2004.

[18] J. Chen, L. Lu, and K. Lu, "Hardness and strain rate sensitivity of nanocrystalline Cu," *Scr. Mater.*, vol. 54, pp. 1913–1918, 2006.

[19] B. Farrokh and A. S. Khan, "Grain size, strain rate, and temperature dependence of flow stress in ultra-fine grained and nanocrystalline Cu and Al: Synthesis, experiment, and constitutive modeling," *Int. J. Plast.*, vol. 25, no. 5, pp. 715–732, 2009.

[20] T. Suo, Y. Li, F. Zhao, X. Fan, and W. Guo, "Compressive behavior and rate-controlling mechanisms of ultrafine grained copper over wide temperature and strain rate ranges," *Mech. Mater.*, vol. 61, no. March, pp. 1–10, 2013.

[21] S. Nemat-Nasser and W.-G. Guo, "Flow stress of commercially pure niobium over a broad range of temperatures and strain rates," *Mater. Sci. Eng. A*, vol. 284, pp. 202–210, 2000.

[22] A. K. Mukherjee, "An examination of the constitutive equation for elevated temperature plasticity," *Mater. Sci. Eng. A*, vol. 322, no. 1-2, pp. 1–22, 2002.

[23] J. Wehrs, G. Mohanty, G. Guillonneau, A. a. Taylor, X. Maeder, D. Frey, L. Philippe, S. Mischler, J. M. Wheeler, and J. Michler, "Comparison of In Situ Micromechanical Strain-Rate Sensitivity Measurement Techniques," *Jom*, vol. 67, no. 8, pp. 1684–1693, 2015.

[24] S. Lotfian, M. Rodríguez, K. E. Yazzie, N. Chawla, J. Llorca, and J. M. Molina-Aldareguía, "High temperature micropillar compression of Al/SiC nanolaminates," *Acta Mater.*, vol. 61, no. 12, pp. 4439–4451, 2013.

[25] R. Raghavan, J. Wheeler, D. Esqué-de los Ojos, K. Thomas, E. Almandoz, G. Fuentes, and J. Michler, "Mechanical behavior of Cu/TiN multilayers at ambient and elevated temperatures: Stress-assisted diffusion of Cu," *Mater. Sci. Eng. A*, vol. 620, pp. 375–382, 2015.

[26] M. A. Monclús, S. J. Zheng, J. R. Mayeur, I. J. Beyerlein, N. A. Mara, T. Polcar, J. Llorca, and J. M. Molina-Aldareguía, "Optimum high temperature strength of two-dimensional nanocomposites," *APL Mater.*, vol. 1, no. 5, pp. 1–8, 2013.

[27] N. A. Mara, D. Bhattacharyya, P. Dickerson, R. G. Hoagland, and A. Misra, "Deformability of ultra-high strength 5 nm Cu/Nb nanolayered composites," *Appl. Phys. Lett.*, vol. 92, no. 23, pp. 10–13, 2008.

[28] J. Y. Zhang, S. Lei, J. Niu, Y. Liu, G. Liu, X. Zhang, and J. Sun, "Intrinsic and extrinsic size effects on deformation in nanolayered Cu/Zr micropillars: From bulk-like to small-volume materials behavior," *Acta Mater.*, vol. 60, no. 10, pp. 4054–4064, 2012.

[29] J. Y. Zhang, S. Lei, Y. Liu, J. J. Niu, Y. Chen, G. Liu, X. Zhang, and J. Sun, "Length scale-dependent deformation behavior of nanolayered Cu/Zr micropillars," *Acta Mater.*, vol. 60, no. 4, pp. 1610–1622, 2012.

[30] E. Frutos, M. Callisti, M. Karlik, and T. Polcar, "Length-scale-dependent mechanical behaviour of Zr/Nb multilayers as a function of individual layer thickness," *Mater. Sci. Eng. A*, vol. 632, pp. 137–146, 2015.

[31] R. Raghavan, T. Harzer, V. Chawla, S. Djaziri, B. Phillipi, J. Wehrs, J. Wheeler, J. Michler, and G. Dehm, "Comparing small scale plasticity of copper-chromium nanolayered and alloyed thin films at elevated temperatures," *Acta Mater.*, vol. 93, pp. 175–186, 2015.

[32] J. Y. Zhang, G. Liu, S. Y. Lei, J. J. Niu, and J. Sun, "Transition from homogeneous-like to shear-band deformation in nanolayered crystalline Cu/amorphous Cu-Zr micropillars: Intrinsic vs. extrinsic size effect," *Acta Mater.*, vol. 60, no. 20, pp. 7183–7196, 2012.

[33] M. Z. Wei, Z. H. Cao, J. Shi, G. J. Pan, L. J. Xu, and X. K. Meng, "Anomalous plastic deformation in nanoscale Cu/Ta multilayers," *Mater. Sci. Eng. A*, vol. 598, pp. 355–359, 2014.

[34] J. Wang and A. Misra, "An overview of interface-dominated deformation mechanisms in metallic multilayers," *Curr. Opin. Solid State Mater. Sci.*, vol. 15, no. 1, pp. 20–28, 2011.

[35] S. Shao and S. N. Medyanik, "Interaction of dislocations with incoherent interfaces in nanoscale FCCBCC metallic bi-layers," *Model. Simul. Mater. Sci. Eng.*, vol. 18, no. 5, p. 055010, 2010.

[36] S. P. Wen, R. L. Zong, F. Zeng, Y. Gao, and F. Pan, "Evaluating modulus and hardness enhancement in evaporated Cu/W multilayers," *Acta Mater.*, vol. 55, no. 1, pp. 345–351, 2007.

[37] a. Misra, M. J. Demkowicz, X. Zhang, and R. G. Hoagland, "The radiation damage tolerance of ultra-high strength nanolayered composites," *Jom*, vol. 59, no. 9, pp. 62–65, 2007.

[38] S. B. Lee, J. E. Ledonne, S. C. V. Lim, I. J. Beyerlein, and A. D. Rollett, "The heterophase interface character distribution of physical vapor-deposited and accumulative roll-bonded Cu-Nb multilayer composites," *Acta Mater.*, vol. 60, no. 4, pp. 1747–1761, 2012.

[39] X. Liu, N. T. Nuhfer, a. D. Rollett, S. Sinha, S. B. Lee, J. S. Carpenter, J. E. Ledonne, A. Darbal, and K. Barmak, "Interfacial orientation and misorientation relationships in nanolamellar Cu/Nb composites using transmission-electron-microscope-based orientation and phase mapping," *Acta Mater.*, vol. 64, pp. 333–344, 2014.

[40] J. S. Carpenter, X. Liu, A. Darbal, N. T. Nuhfer, R. J. McCabe, S. C. Vogel, J. E. Ledonne, a. D. Rollett, K. Barmak, I. J. Beyerlein, and N. a. Mara, "A comparison of texture results obtained using precession electron diffraction and neutron diffraction methods at diminishing length scales in ordered bimetallic nanolamellar composites," *Scr. Mater.*, vol. 67, no. 4, pp. 336–339, 2012.

[41] I. J. Beyerlein, J. R. Mayeur, S. Zheng, N. A. Mara, J. Wang, and A. Misra, "Emergence of stable interfaces under extreme plastic deformation.," *Proc. Natl. Acad. Sci. U. S. A.*, pp. 1–5, 2014.

[42] J. Wang, K. Kang, R. F. Zhang, S. J. Zheng, I. J. Beyerlein, and N. a. Mara, "Structure and property of interfaces in ARB Cu/Nb laminated composites," *Jom*, vol. 64, no. 10, pp. 1208–1217, 2012.

[43] A. Misra, M. Verdier, Y. C. Lu, H. Kung, T. E. Mitchell, M. Nastasi, and J. D. Embury, "STRUCTURE AND MECHANICAL PROPERTIES OF Cu-X ( X Nb , Cr , Ni ) NANOLAYERED COMPOSITES," *Scr. Mater.*, vol. 39, pp. 555–560, 1998.

[44] N. A. Mara, D. Bhattacharyya, J. P. Hirth, P. Dickerson, and A. Misra, "Mechanism for shear banding in nanolayered composites," *Appl. Phys. Lett.*, vol. 97, no. 2, pp. 2–4, 2010.

[45] X. Y. Zhu, J. T. Luo, F. Zeng, and F. Pan, "Microstructure and ultrahigh strength of nanoscale Cu/Nb multilayers," *Thin Solid Films*, vol. 520, no. 2, pp. 818–823, 2011.

[46] D. Bhattacharyya, N. Mara, P. Dickerson, R. Hoagland, and A. Misra, "Transmission electron microscopy study of the deformation behavior of Cu/Nb and Cu/Ni nanoscale multilayers during nanoindentation," *J. Mater. Res.*, vol. 24, no. 03, pp. 1291–1302, 2009.

[47] S. J. Zheng, I. J. Beyerlein, J. Wang, J. S. Carpenter, W. Z. Han, and N. a. Mara, "Deformation twinning mechanisms from bimetal interfaces as revealed by in situ straining in the TEM," *Acta Mater.*, vol. 60, no. 16, pp. 5858–5866, 2012.

[48] I. J. Beyerlein, J. R. Mayeur, R. J. McCabe, S. J. Zheng, J. S. Carpenter, and N. a. Mara, "Influence of slip and twinning on the crystallographic stability of bimetal interfaces in nanocomposites under deformation," *Acta Mater.*, vol. 72, pp. 137–147, 2014.

[49] N. A. Mara, A. Misra, R. G. Hoagland, A. V. Sergueeva, T. Tamayo, P. Dickerson, and A. K. Mukherjee, "High-temperature mechanical behavior/microstructure correlation of Cu/Nb nanoscale multilayers," *Mater. Sci. Eng. A*, vol. 493, no. 1-2, pp. 274–282, 2008.

[50] N. Mara, A. Sergueeva, A. Misra, and A. K. Mukherjee, "Structure and high-temperature mechanical behavior relationship in nano-scaled multilayered materials," *Scr. Mater.*, vol. 50, no. 6, pp. 803–806, 2004.

[51] N. A. Mara, T. Tamayo, a. V. Sergueeva, X. Zhang, A. Misra, and a. K. Mukherjee, "The effects of decreasing layer thickness on the high temperature mechanical behavior of Cu / Nb nanoscale multilayers," *Thin Solid Films*, vol. 515, no. 6, pp. 3241–3245, 2007.

[52] A. Misra, R. Hoagland, and H. Kung, "Thermal stability of self-supported nanolayered Cu/Nb films," *Philos. Mag.*, vol. 84, no. 10, pp. 1021–1028, 2004.

[53] J. Carpenter, S. Zheng, R. Zhang, S. Vogel, I. Beyerlein, and N. Mara, "Thermal stability of CuNb nanolamellar composites fabricated via accumulative roll bonding," *Philos. Mag.*, no. July 2014, pp. 1–18, 2012.

[54] A. Misra and R. Hoagland, "Effects of Elevated Temperature Annealing on the Structure and Hardness of Copper/niobium Nanolayered Films," *J. Mater. Res.*, vol. 20, no. 08, pp. 2046–2054, 2005.

[55] M. D. Uchic and D. M. Dimiduk, "A methodology to investigate size scale effects in crystalline plasticity using uniaxial compression testing," *Mater. Sci. Eng. A*, vol. 400-401, no. 1-2 SUPPL., pp. 268–278, 2005.

[56] M. D. Uchic, D. M. Dimiduk, J. N. Florando, and W. D. Nix, "Sample dimensions influence strength and crystal plasticity.," *Science*, vol. 305, no. 5686, pp. 986–989, 2004.

[57] J. Y. Kim and J. R. Greer, "Size-dependent mechanical properties of molybdenum nanopillars," *Applied Physics Letters*, vol. 93, 2008.

[58] J. R. Greer, W. C. Oliver, and W. D. Nix, "Size dependence of mechanical properties of gold at the micron scale in the absence of strain gradients," *Acta Mater.*, vol. 53, no. 6, pp. 1821–1830, 2005.

[59] R. Soler, J. M. Wheeler, H.-j. Chang, J. Segurado, J. Michler, J. Llorca, and J. M. Molina-aldareguia, "Understanding size effects on the strength of single crystals through high-temperature micropillar compression," *Acta Mater.*, vol. 81, pp. 50–57, 2014.

[60] J. Wheeler, D. Armstrong, W. Heinz, and R. Schwaiger, "High temperature nanoindentation: The state of the art and future challenges," *Curr. Opin. Solid State Mater. Sci.*, no. February, 2015.

[61] S. Korte, R. J. Stearn, J. M. Wheeler, and W. J. Clegg, "High temperature microcompression and nanoindentation in vacuum," *J. Mater. Res.*, vol. 27, no. 01, pp. 167–176, 2012.

[62] J. M. Wheeler and J. Michler, "Review of indenter materials for high temperature nanoindentation.".

[63] J. Hütsch and E. T. Lilleodden, "The influence of focused-ion beam preparation technique on microcompression investigations: Lathe vs. annular milling," *Scr. Mater.*, vol. 77, pp. 49–51, 2014.

[64] D. Kiener, C. Motz, and G. Dehm, "Micro-compression testing: A critical discussion of experimental constraints," *Mater. Sci. Eng. A*, vol. 505, no. 1-2, pp. 79–87, 2009.

[65] H. Zhang, B. E. Schuster, Q. Wei, and K. T. Ramesh, "The design of accurate micro-compression experiments," *Scr. Mater.*, vol. 54, no. 2, pp. 181–186, 2006.

[66] I. N. Sneddon, “The relation between load and penetration in the axisymmetric boussinesq problem for a punch of arbitrary profile,” *Int. J. Eng. Sci.*, vol. 3, no. 1, pp. 47–57, 1965.

[67] R. Soler, J. M. Molina-Aldareguia, J. Segurado, and J. Llorca, “Effect of misorientation on the compression of highly anisotropic single-crystal micropillars,” *Adv. Eng. Mater.*, vol. 14, no. 11, pp. 1004–1008, 2012.

[68] R. J. Asaro and S. Suresh, “Mechanistic models for the activation volume and rate sensitivity in metals with nanocrystalline grains and nano-scale twins,” *Acta Mater.*, vol. 53, no. 12, pp. 3369–3382, 2005.

[69] H. Fei, A. Abraham, N. Chawla, and H. Jiang, “Evaluation of Micro-Pillar Compression Tests for Accurate Determination of Elastic-Plastic Constitutive Relations,” *J. Appl. Mech.*, vol. 79, no. November, p. 061011, 2012.

[70] J. Zhao, F. Wang, P. Huang, T. Lu, and K. Xu, “Depth dependent strain rate sensitivity and inverse indentation size effect of hardness in body-centered cubic nanocrystalline metals,” *Mater. Sci. Eng. A*, vol. 615, pp. 87–91, 2014.

[71] Y. M. Wang and E. Ma, “Strain hardening, strain rate sensitivity, and ductility of nanostructured metals,” *Mater. Sci. Eng. A*, vol. 375-377, no. 1-2 SPEC. ISS., pp. 46–52, 2004.

[72] J. M. Wheeler, V. Maier, K. Durst, M. Göken, and J. Michler, “Activation parameters for deformation of ultrafine-grained aluminium as determined by indentation strain rate jumps at elevated temperature,” *Mater. Sci. Eng. A*, vol. 585, pp. 108–113, 2013.

[73] A. Misra, J. P. Hirth, R. G. Hoagland, J. D. Embury, and H. Kung, “Dislocation mechanisms and symmetric slip in rolled nano-scale metallic multilayers,” *Acta Mater.*, vol. 52, no. 8, pp. 2387–2394, 2004.

[74] C. Langlois, S. Guerin, M. Sennour, M. J. Hytch, C. Duhamel, and Y. Champion, “Thermomechanical behaviour of nanostructured copper,” *J. Alloys Compd.*, vol. 434-435, no. SPEC. ISS., pp. 279–282, 2007.

[75] A. Yilmaz, “The PortevinLe Chatelier effect: a review of experimental findings,” *Sci. Technol. Adv. Mater.*, vol. 12, no. 6, p. 063001, 2011.

[76] A. S. Schneider, D. Kaufmann, B. G. Clark, C. P. Frick, P. a. Gruber, R. Mönig, O. Kraft, and E. Arzt, “Correlation between critical temperature and strength of small-scale bcc pillars,” *Phys. Rev. Lett.*, vol. 103, no. 10, pp. 1–4, 2009.